

AD-A171 252

IGNITION AND COMBUSTION OF ALUMINUM AND ALUMINUM/CARBON  
SLURRY AGGLOMERAT (U) PENNSYLVANIA STATE UNIV  
UNIVERSITY PARK DEPT OF MECHANICAL EN

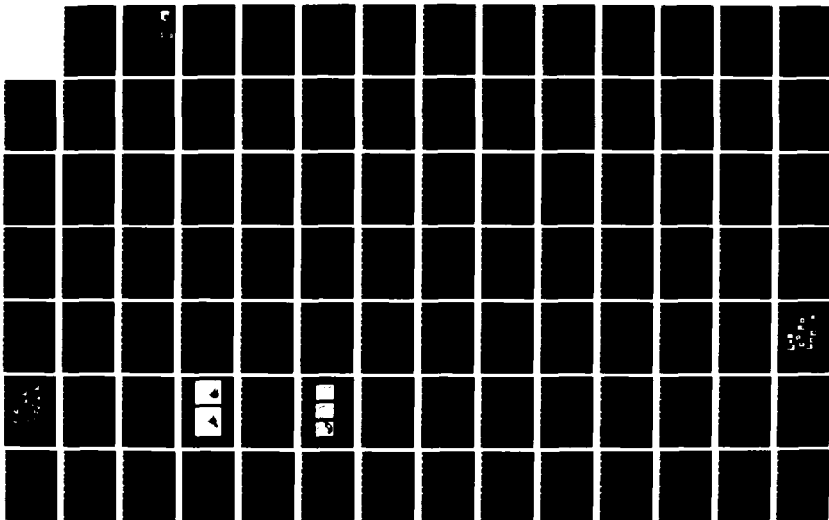
1/2

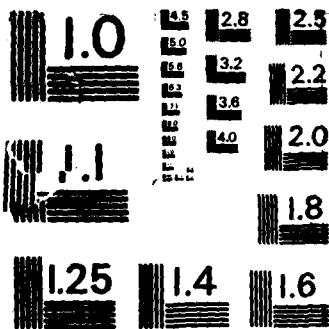
UNCLASSIFIED

S C MONG ET AL. MAY 86 PSU-ME-85-R-0063

F/G 21/2

NL





MICROCOPY RESOLUTION TEST CHART  
 NATIONAL BUREAU OF STANDARDS-1963-A

2



AFWAL-TR-86-2005

IGNITION AND COMBUSTION OF ALUMINUM AND ALUMINUM/CARBON SLURRY AGGLOMERATES

S.-C. Wong and S.R. Turns

Department of Mechanical Engineering  
The Pennsylvania State University  
University Park, PA 16802

May 1986

Final Report for Period September 1984-December 1985

Approved for Public Release; Distribution is unlimited

DTIC  
SELECTED  
AUG 26 1986  
S D D

AD-A171 252

DTIC FILE COPY

AERO PROPULSION LABORATORY  
AIR FORCE WRIGHT AERONAUTICAL LABORATORIES  
AIR FORCE SYSTEMS COMMAND  
WRIGHT-PATTERSON AIR FORCE BASE, OHIO 45433-6563

## NOTICE

When Government drawings, specifications, or other data are used for any purpose other than in connection with a definitely related Government procurement operation, the United States Government thereby incurs no responsibility nor any obligation whatsoever; and the fact that the government may have formulated, furnished, or in any way supplied the said drawings, specifications, or other data, is not to be regarded by implication or otherwise as in any manner licensing the holder or any other person or corporation, or conveying any rights or permission to manufacture, use, or sell any patented invention that may in any way be related thereto.

This report has been reviewed by the Office of Public Affairs (ASD/PA) and is releasable to the National Technical Information Service (NTIS). At NTIS, it will be available to the general public, including foreign nations.

This technical report has been reviewed and is approved for publication.



CHARLES R. MARTEL, Tech Area Mgr  
Fuels Branch  
Fuels and Lubrication Division  
Aero Propulsion Laboratory



ARTHUR V. CHURCHILL, Chief  
Fuels Branch  
Fuels and Lubrication Division  
Aero Propulsion Laboratory

FOR THE COMMANDER



BENITO P. BOTTERI, Asst Chief  
Fuels and Lubrication Division  
Aero Propulsion Laboratory

"If your address has changed, if you wish to be removed from our mailing list, or if the addressee is not longer employed by your organization, please notify AFWAL/POSF, Wright-Patterson AFB, Ohio 45433-6563 to help us maintain a current mailing list."

Copies of this report should not be returned unless return is required by security considerations, contractual obligations, or notice on a specific document.

UNCLASSIFIED

SECURITY CLASSIFICATION OF THIS PAGE

AD-A171252

## REPORT DOCUMENTATION PAGE

1a REPORT SECURITY CLASSIFICATION Unclassified		1b RESTRICTIVE MARKINGS NA	
2a SECURITY CLASSIFICATION AUTHORITY NA		3. DISTRIBUTION/AVAILABILITY OF REPORT Approved for Public Release; Distribution is unlimited	
2b DECLASSIFICATION/DOWNGRADING SCHEDULE NA			
4 PERFORMING ORGANIZATION REPORT NUMBER(S) PSU-ME-85-R-0063		5. MONITORING ORGANIZATION REPORT NUMBER(S) AFWAL-TR-86-2005	
6a NAME OF PERFORMING ORGANIZATION Department of Mechanical Eng. The Pennsylvania State Univ.	6b OFFICE SYMBOL (if applicable)	7a. NAME OF MONITORING ORGANIZATION Battelle Columbus Division	
6c. ADDRESS (City, State, and ZIP Code) University Park, PA 16802		7b. ADDRESS (City, State, and ZIP Code) 505 King Avenue Columbus, Ohio 43216	
8a NAME OF FUNDING/SPONSORING ORGANIZATION Aero Propulsion Laboratory	8b OFFICE SYMBOL (if applicable) AFWL/POSF	9. PROCUREMENT INSTRUMENT IDENTIFICATION NUMBER F33615-84-C-2410	
8c. ADDRESS (City, State, and ZIP Code) Wright Patterson AFB, Ohio 45433-6563		10. SOURCE OF FUNDING NUMBERS	
		PROGRAM ELEMENT NO. 62203F	PROJECT NO. 3048
		TASK NO. 05	WORK UNIT ACCESSION NO. 34
11 TITLE (Include Security Classification) Ignition and Combustion of Aluminum and Aluminum/Carbon Slurry Agglomerates (Unclassified)			
12 PERSONAL AUTHOR(S) S.-C. Wong and S. R. Turns			
13a TYPE OF REPORT Final	13b TIME COVERED FROM 9/84 TO 12/85	14. DATE OF REPORT (Year, Month, Day) May 1986	15 PAGE COUNT 161
16 SUPPLEMENTARY NOTATION			
17 COSATI CODES		18. SUBJECT TERMS (Continue on reverse if necessary and identify by block number)	
FIELD	GROUP	SUB-GROUP	
21	02		
21	04		
19 ABSTRACT (Continue on reverse if necessary and identify by block number)			
<p>An experimental and theoretical study of the ignition and combustion of aluminum and aluminum/carbon slurry fuel droplets in both dry and wet environments was performed. Individual slurry droplets having initial diameters ranging from 500-1100<math>\mu</math>m, supported on 125<math>\mu</math>m diameter silicon carbide filaments and rapidly exposed to the post-flame region of a flat-flame burner, were studied. Burner post-flame environments were characterized by determination of species mole fractions using gas chromatography, ambient gas temperature using Pt/Pt-10% Ph fine wire thermocouples, and ambient gas velocities using conservation of mass. Burner operating conditions were varied to provide oxygen mole fractions ranging from 0.10 to 0.25, and gas temperatures from 1250-1869 K at atmospheric pressure. Particle life histories were characterized by measurement of particle diameter as a function of residence time in the burner gases using backlit and/or natural-light motion picture photography. Ignition and burning times were measured, and low-temperature ignition limits were determined. Composition and morphology of the residual combustion products were (over)</p>			
20 DISTRIBUTION/AVAILABILITY OF ABSTRACT <input checked="" type="checkbox"/> UNCLASSIFIED/UNLIMITED <input type="checkbox"/> SAME AS RPT <input type="checkbox"/> DTIC USERS		21 ABSTRACT SECURITY CLASSIFICATION UNCLASSIFIED	
22a NAME OF RESPONSIBLE INDIVIDUAL Eva M. Conley		22b TELEPHONE (Include Area Code) (513)255-7211	22c OFFICE SYMBOL AFWAL: POSF

DD FORM 1473, 84 MAR

83 APR edition may be used until exhausted  
All other editions are obsolete

SECURITY CLASSIFICATION OF THIS PAGE

U.S. Government Printing Office: 1985-507-047

UNCLASSIFIED

ABSTRACT (Continued)

SEM. →

determined using X-ray diffraction techniques and scanning electron microscopy, respectively.

Both the ignition and burning process were modeled analytically. In the aluminum slurry ignition model, the processes of slurry droplet heat-up, liquid fuel combustion, and agglomerate heat-up were treated. To account for the enhanced convective heat transfer compared to a solid sphere that occurs for the porous aluminum agglomerates, a convective transport enhancement factor was used. A value for the transport enhancement factor was determined experimentally. To model the combustion process of the coalesced molten aluminum droplets, the vapor-phase combustion analysis of Law was adapted and extended to account for oxide build-up and convective effects. The theoretical predictions of both the ignition and combustion model were compared with the experimental results. It was found that both theoretical models provided reasonable interpretations of the experimental data.

ACKNOWLEDGEMENTS

The authors would like to acknowledge the following persons for their assistance in this project: Dr. L.W. Hall, Jr. of Sun Refining and Marketing Company for providing the slurry samples, D.L. Gamberoni for help in data reduction, Dr. R.E. Tressler for providing the SiC filament, and S. Anderson for typing of the manuscript. The authors also are particularly grateful to Dr. E. Ryba for performing the X-ray diffraction analysis.



Accession For	
NTIS CRA&I	<input checked="" type="checkbox"/>
DTIC TAB	<input type="checkbox"/>
Unannounced	<input type="checkbox"/>
Justification	
By	
Distribution /	
Availability Codes	
Dist	Avail and/or Special
A-1	

## TABLE OF CONTENTS

<u>Section</u>	<u>Page</u>
I. INTRODUCTION.....	1
1.1 GENERAL PROBLEM STATEMENT.....	1
1.2 PREVIOUS RELATED STUDIES.....	2
1.2.1 Ignition of Single Aluminum Particles.....	2
1.2.2 Combustion of Single Aluminum Particles.....	5
1.2.2.1 Experimental Studies.....	6
1.2.2.2 Theoretical Models.....	7
1.2.3 Aluminum Slurry Ignition.....	8
1.3 OBJECTIVES.....	9
II. EXPERIMENTAL APPROACH.....	11
2.1 TEST APPARATUS.....	11
2.2 TEST CONDITIONS.....	16
2.3 SLURRY SAMPLES.....	21
2.4 TEST PROCEDURE.....	21
III. THEORETICAL APPROACH.....	23
3.1 AGGLOMERATE IGNITION MODEL.....	23
3.1.1 Overview.....	23
3.1.2 JP-10 Gasification.....	25
3.1.2.1 Assumptions.....	25
3.1.2.2 Gas-Phase Conservation Relations.....	26
3.1.2.3 Liquid-Phase Conservation Relations.....	29
3.1.3 Dry Agglomerate Heat-Up.....	31
3.1.3.1 Assumptions.....	31
3.1.3.2 Energy Conservation.....	33
3.2 ALUMINUM COMBUSTION MODEL.....	37
3.2.1 Overview.....	37
3.2.2 Assumptions.....	37
3.2.3 Gas-Phase Mass Conservation.....	39
3.2.4 Species Conservation.....	42
3.2.5 Energy Conservation.....	43
3.2.6 Particle Mass Conservation.....	47
3.2.7 Solution Approach.....	48
IV. RESULTS AND DISCUSSION.....	50
4.1 GENERAL OBSERVATIONS.....	50
4.1.1 Slurry Droplet Life History.....	50
4.1.1.1 CO/O <sub>2</sub> /N <sub>2</sub> Flames.....	50
4.1.1.2 CH <sub>4</sub> /O <sub>2</sub> /N <sub>2</sub> Flames.....	54
4.1.2 Agglomerate Structure.....	56
4.1.3 Ignition and Combustion Characteristics.....	56
4.1.4 Heat-Up Characteristics.....	61
4.2 IGNITION.....	63
4.2.1 Aluminum Slurries.....	63
4.2.1.1 Ignition Limits.....	63
4.2.1.2 Diameter Effects.....	66
4.2.1.3 Temperature Effects.....	68
4.2.1.4 Slurry Composition Effects.....	68
4.2.1.5 Oxygen Mole Fraction Effects.....	71
4.2.2 Aluminum/Carbon Slurries.....	71

TABLE OF CONTENTS (CONTINUED)

4.2.3	Transport Enhancement Determination.....	73
4.3	COMBUSTION.....	75
4.3.1	Aluminum Slurries.....	75
4.3.1.1	Typical Theoretical Results.....	75
4.3.1.2	Initial Diameter Effects.....	77
4.3.1.3	Oxygen Mole Fraction Effects.....	80
4.3.1.4	Ambient Temperature Effects.....	83
4.3.1.5	Water Vapor Effects.....	83
4.3.1.6	Slurry Composition Effects.....	85
4.3.1.7	Comparison of Aluminum and JP-10 Burning Times.....	85
4.3.2	Aluminum/Carbon Slurries.....	88
4.4	COMBUSTION PRODUCT ANALYSIS.....	89
4.4.1	Accumulated Products.....	89
4.4.1.1	Aluminum Slurries.....	89
4.4.1.2	Aluminum/Carbon Slurries.....	95
4.4.2	Dispersed Products.....	99
V.	SUMMARY AND CONCLUSIONS.....	101
5.1	SUMMARY.....	101
5.2	CONCLUSIONS.....	104
	REFERENCES.....	107
	APPENDIX A - JP-10 Evaporation Calibration.....	111
	APPENDIX B - Slurry Ignition and Burning Time Data.....	119
	APPENDIX C - Slurry Droplet Diameter Histories.....	128
	APPENDIX D - JP-10 Burning Time Data.....	141

## LIST OF ILLUSTRATIONS

		<u>Page</u>
FIGURE 1.	Schematic diagram of test rig and instrumentation.	12
FIGURE 2.	Schematic diagram of laminar premixed flat-flame burner.	14
FIGURE 3.	Schematic diagram of the thermocouple probe.	17
FIGURE 4.	Schematic diagram of the water-cooled gas sampling probe.	19
FIGURE 5.	Aluminum slurry ignition model.	24
FIGURE 6.	Schematic diagram illustrating method to determine transport enhancement factors.	36
FIGURE 7.	Aluminum combustion model incorporating oxide accumulation.	38
FIGURE 8.	Mass fluxes of fuel, oxidizer, and combustion products used in the combustion model.	40
FIGURE 9.	Radiant fluxes at the burning droplet surface and at the flame zone.	46
FIGURE 10.	Typical aluminum slurry droplet life history--natural light.	51
FIGURE 11.	Typical aluminum slurry droplet history--backlit.	52
FIGURE 12.	Photographs showing characteristics of jetting (lower) and partial fragmentation (upper).	55
FIGURE 13.	SEM micrographs of agglomerates formed from three different aluminum-based slurries.	57
FIGURE 14.	Typical diameter-versus-time plots for various aluminum-based slurry types.	58
FIGURE 15.	Typical temperature-versus-time plots for stabilized Al/JP-10 slurry droplets.	62
FIGURE 16.	Minimum ambient gas temperatures required for ignition versus initial diameter for stabilized Al/JP-10 slurry.	64
FIGURE 17.	Ignition times versus initial droplet diameter for stabilized Al/JP-10 slurry.	67
FIGURE 18.	Ignition times versus gas temperature for stabilized Al/JP-10 slurries.	69

LIST OF ILLUSTRATIONS (Continued)

	<u>Page</u>
FIGURE 19. Ignition times versus gas temperature for stabilized and unstabilized Al/JP-10 slurries.	70
FIGURE 20. Ignition time versus ambient oxygen mole fraction for stabilized Al/JP-10 slurry.	72
FIGURE 21. Transport enhancement factor versus initial slurry droplet diameter for stabilized Al/JP-10 slurry.	74
FIGURE 22. Predicted life history of aluminum agglomerate after ignition.	76
FIGURE 23. Predicted influence of flame emissivity on dimensionless burning rate, flame radius, product vapor mass fraction at the flame, and the fraction of oxide dissociated.	78
FIGURE 24. Burning times versus diameter of molten droplet following coalescence.	79
FIGURE 25. Comparison between the burning times of stabilized aluminum slurry droplets and single aluminum particles.	81
FIGURE 26. Aluminum droplet burning times versus oxygen mole fraction.	82
FIGURE 27. Aluminum droplet burning times versus ambient gas temperature.	84
FIGURE 28. Aluminum droplet burning times versus ambient gas temperature for stabilized and unstabilized Al/JP-10 slurries.	86
FIGURE 29. Comparison between the burning times of aluminum droplets and JP-10 droplets.	87
FIGURE 30. SEM micrographs of residual combustion products for stabilized Al/JP-10 slurry in wet flames.	90
FIGURE 31. SEM micrographs of residual combustion products for stabilized Al/JP-10 slurry in dry flames.	92
FIGURE 32. SEM micrographs of residual combustion products for unstabilized Al/JP-10 slurry in dry flames.	94
FIGURE 33. SEM micrographs of residual combustion products for stabilized Al/C/JP-10 slurry in dry flames.	97

LIST OF ILLUSTRATIONS (Continued)

		<u>Page</u>
FIGURE 34.	SEM micrographs of residual combustion products for stabilized Al/C/JP-10 slurry in wet flames.	98
FIGURE 35.	Smoke particle size distribution for stabilized Al/JP-10 slurry at $T_{\infty}=1809$ K, $O_2=10.4\%$ .	100
FIGURE A.1	Calibration for $\alpha$ at $T_{\infty}=1510$ K, $O_2=10.0\%$ dry flame condition.	112
FIGURE A.2	Calibration for $\alpha$ at $T_{\infty}=1548$ K, $O_2=10.3\%$ dry flame condition.	113
FIGURE A.3	Calibration for $\alpha$ at $T_{\infty}=1659$ K, $O_2=10.4\%$ dry flame condition.	114
FIGURE A.4	Calibration for $\alpha$ at $T_{\infty}=1809$ K, $O_2=10.4\%$ dry flame condition.	115
FIGURE A.5	Calibration for $\alpha$ at $T_{\infty}=1827$ K, $O_2=25.2\%$ dry flame condition.	116
FIGURE A.6	Calibration for $\alpha$ at $T_{\infty}=1519$ K, $O_2=10.9\%$ wet flame condition.	117
FIGURE A.7	Calibration for $\alpha$ at $T_{\infty}=1677$ K, $O_2=10.9\%$ wet flame condition.	118

LIST OF TABLES

		<u>Page</u>
TABLE 1.	Summary of CO/O <sub>2</sub> /N <sub>2</sub> Flame Conditions	20
TABLE 2.	Summary of CH <sub>4</sub> /O <sub>2</sub> /N <sub>2</sub> Flame Conditions	21
TABLE 3.	Slurry Samples	21
TABLE 4.	Test for Agglomerate Lumpiness	33
TABLE 5.	Comparison of Slurry Characteristics in CO/O <sub>2</sub> /N <sub>2</sub> Flame Environments	60
TABLE 6.	Residual Combustion Product Analysis--CH <sub>4</sub> /O <sub>2</sub> /N <sub>2</sub> Flame Environments	91
TABLE 7.	Residual Combustion Product Analysis--CO/O <sub>2</sub> /N <sub>2</sub> Flame Environments	93
TABLE 8.	Conversion of Al <sub>4</sub> C <sub>3</sub> to Al <sub>2</sub> O <sub>3</sub> at T <sub>∞</sub> = 1785 K, O <sub>2</sub> = 10.3%	96
TABLE B.1	Ignition and Burning Times for Stabilized Al Slurry, T <sub>∞</sub> = 1510 K, φ = 0.54, O <sub>2</sub> = 10.0%, Dry	119
TABLE B.2	Ignition and Burning Times for Stabilized Al Slurry, T <sub>∞</sub> = 1548 K, φ = 0.59, O <sub>2</sub> = 10.3%, Dry	120
TABLE B.3	Ignition and Burning Times for Stabilized Al Slurry, T <sub>∞</sub> = 1659 K, φ = 0.66, O <sub>2</sub> = 10.4%, Dry	120
TABLE B.4	Ignition and Burning Times for Stabilized Al Slurry, T <sub>∞</sub> = 1809 K, φ = 0.58, O <sub>2</sub> = 10.4%, Dry	121
TABLE B.5	Ignition and Burning Times for Stabilized Al Slurry, T <sub>∞</sub> = 1868 K, φ = 0.58, O <sub>2</sub> = 11.4%, Dry	122
TABLE B.6	Ignition and Burning Times for Stabilized Al Slurry, T <sub>∞</sub> = 1888 K, φ = 0.58, O <sub>2</sub> = 12.9%, Dry	122
TABLE B.7	Ignition and Burning Times for Stabilized Al Slurry, T <sub>∞</sub> = 1869 K, φ = 0.58, O <sub>2</sub> = 13.8%, Dry	122
TABLE B.8	Ignition and Burning Times for Stabilized Al Slurry, T <sub>∞</sub> = 1827 K, φ = 0.37, O <sub>2</sub> = 25.2%, Dry	123
TABLE B.9	Ignition and Burning Times for Stabilized Al Slurry, T <sub>∞</sub> = 1907 K, φ = 0.58, O <sub>2</sub> = 10.4%, Dry with Argon Diluent	123
TABLE B.10	Ignition and Burning Times for Stabilized Al Slurry, T <sub>∞</sub> = 1417 K, φ = 0.50, O <sub>2</sub> = 10.9%, Wet	123

## LIST OF TABLES (Continued)

	<u>Page</u>
TABLE B.11 Ignition and Burning Times for Stabilized Al Slurry, $T_{\infty} = 1519 \text{ K}$ , $\phi = 0.50$ , $O_2 = 10.9\%$ , Wet	124
TABLE B.12 Ignition and Burning Times for Stabilized Al Slurry, $T_{\infty} = 1677 \text{ K}$ , $\phi = 0.58$ , $O_2 = 10.9\%$ , Wet	124
TABLE B.13 Ignition and Burning Times for Stabilized Al Slurry, $T_{\infty} = 1785 \text{ K}$ , $\phi = 0.62$ , $O_2 = 10.3\%$ , Wet	125
TABLE B.14 Ignition and Burning Times for Unstabilized Al Slurry, $T_{\infty} = 1510 \text{ K}$ , $\phi = 0.54$ , $O_2 = 10.0\%$ , Dry	125
TABLE B.15 Ignition and Burning Times for Unstabilized Al Slurry, $T_{\infty} = 1548 \text{ K}$ , $\phi = 0.59$ , $O_2 = 10.3\%$ , Dry	126
TABLE B.16 Ignition and Burning Times for Unstabilized Al Slurry, $T_{\infty} = 1659 \text{ K}$ , $\phi = 0.66$ , $O_2 = 10.4\%$ , Dry	126
TABLE B.17 Ignition and Burning Times for Unstabilized Al Slurry, $T_{\infty} = 1809 \text{ K}$ , $\phi = 0.58$ , $O_2 = 10.4\%$ , Dry	127
TABLE C.1 Diameter Versus Time, $T_{\infty} = 1510 \text{ K}$ , $\phi = 0.54$ , $O_2 = 10.0\%$ , Dry	128
TABLE C.2 Diameter Versus Time, $T_{\infty} = 1659 \text{ K}$ , $\phi = 0.66$ , $O_2 = 10.4\%$ , Dry	129
TABLE C.3 Diameter Versus Time, $T_{\infty} = 1809 \text{ K}$ , $\phi = 0.58$ , $O_2 = 10.4\%$ , Dry	131
TABLE C.4 Diameter Versus Time, $T_{\infty} = 1827 \text{ K}$ , $\phi = 0.37$ , $O_2 = 25.2\%$ , Dry	133
TABLE C.5 Diameter Versus Time for Stabilized Al/JP-10 Slurry, $T_{\infty} = 1907 \text{ K}$ , $\phi = 0.58$ , $O_2 = 10.4\%$ , CO/O <sub>2</sub> /Ar	134
TABLE C.6 Diameter Versus Time, $T_{\infty} = 1417 \text{ K}$ , $\phi = 0.50$ , $O_2 = 10.9\%$ , Wet	135
TABLE C.7 Diameter Versus Time, $T_{\infty} = 1519 \text{ K}$ , $\phi = 0.50$ , $O_2 = 10.9\%$ , Wet	137
TABLE C.8 Diameter Versus Time, $T_{\infty} = 1547 \text{ K}$ , $\phi = 0.53$ , $O_2 = 10.9\%$ , Wet	138
TABLE C.9 Diameter Versus Time, $T_{\infty} = 1677 \text{ K}$ , $\phi = 0.58$ , $O_2 = 10.9\%$ , Wet	139
TABLE C.10 Diameter Versus Time, $T_{\infty} = 1785 \text{ K}$ , $\phi = 0.62$ , $O_2 = 10.3\%$ , Wet	140

LIST OF TABLES (Continued)

		<u>Page</u>
TABLE D.1	JP-10 Burning Times, $T_{\infty} = 1510$ K, $\phi = 0.54$ , $O_2 = 10.0\%$ , Dry	141
TABLE D.2	JP-10 Burning Times, $T_{\infty} = 1548$ K, $\phi = 0.59$ , $O_2 = 10.3\%$ , Dry	142
TABLE D.3	JP-10 Burning Times, $T_{\infty} = 1659$ K, $\phi = 0.66$ , $O_2 = 10.4\%$ , Dry	142
TABLE D.4	JP-10 Burning Times, $T_{\infty} = 1809$ K, $\phi = 0.58$ , $O_2 = 10.4\%$ , Dry	143
TABLE D.5	JP-10 Burning Times, $T_{\infty} = 1827$ K, $\phi = 0.37$ , $O_2 = 25.2\%$ , Dry	143
TABLE D.6	JP-10 Burning Times, $T_{\infty} = 1417$ K, $\phi = 0.50$ , $O_2 = 10.9\%$ , Wet	144
TABLE D.7	JP-10 Burning Times, $T_{\infty} = 1519$ K, $\phi = 0.50$ , $O_2 = 10.9\%$ , Wet	144
TABLE D.8	JP-10 Burning Times, $T_{\infty} = 1547$ K, $\phi = 0.53$ , $O_2 = 10.9\%$ , Wet	145
TABLE D.9	JP-10 Burning Times, $T_{\infty} = 1677$ K, $\phi = 0.58$ , $O_2 = 10.9\%$ , Wet	145
TABLE D.10	JP-10 Burning Times, $T_{\infty} = 1785$ K, $\phi = 0.62$ , $O_2 = 10.3\%$ , Wet	145

## NOMENCLATURE

a	- difference between flame and surface temperatures
b	- difference between flame and ambient temperatures
Bi	- Biot number
$B_y$	- transfer number defined in Eqn. (14)
$B_0$	- defined in Eqn. (17)
$C_p$	- specific heat
d	- diameter
D	- effective mass diffusivity
f	- mass fraction
$F_1, F_2$	- parameters defined in Eqns. (37) and (39), respectively
G	- incident radiant flux
h	- enthalpy or oxide cap height
$\bar{h}$	- average heat-transfer coefficient
$\hat{h}$	- dimensionless enthalpy, $h/L$
$H_1, H_2$	- total energy flux in inner and outer regions, respectively
k	- thermal conductivity
L	- latent heat of vaporization
m	- mass
$\dot{m}$	- mass flow, kg/s
$\dot{m}''$	- mass flux, $\text{kg/s}\cdot\text{m}^2$
M	- dimensionless mass flow, $m/(4\pi\rho D r_s)$
MW	- molecular weight
n	- exponent defined in Eqn. (28)
Nu	- Nusselt number

$P$	- pressure
$Pr$	- Prandtl number
$Q_c, Q_r$	- convective and radiant heat flows, W
$q''$	- heat flux, W/m <sup>2</sup>
$Q_1, Q_2$	- heat of reaction/condensation at $T_s$ for oxide vapor per unit mass of aluminum
$Q$	- $Q_1 + Q_2$
$\hat{Q}$	- $Q/L (1+v)$
$Q_f$	- heat of reaction
$r$	- radial coordinate
$\hat{r}$	- dimensionless radial coordinate, $r/r_s$
$r_{\infty,T}, r_{\infty,m}$	- film radii for heat and mass transfer, respectively
$Re$	- Reynolds number
$Sc$	- Schmidt number
$Sh$	- Sherwood number
$t$	- time
$T$	- temperature
$\hat{T}$	- dimensionless temperature, $C_p T/L$
$v$	- velocity
$V$	- volume
$Y$	- species mass fraction
$\alpha$	- property weighting factor
$\epsilon$	- emissivity
$\zeta_{1,2}$	- parameters defining aluminum combustion mode
$\eta$	- fraction of $\theta$ diffusing inward
$\theta$	- porosity or fraction of oxide vaporized at the flame
$\hat{\theta}$	- $\theta (1+v)$

$\nu$	- stoichiometric mass ratio of oxidizer to fuel
$\xi$	- transport enhancement factor defined by Eqn. (32)
$\rho$	- density
$\sigma$	- Stefan-Boltzmann constant
$\phi$	- equivalence ratio, temperature, or mass fraction
$\psi_{1,2}$	- parameters defined in Eqns. (63) and (64), respectively

### Subscripts

1,2	- inner and outer zones, respectively
$\infty$	- ambient
a	- air
Al	- aluminum
boil	- boiling point
e	- effective
f	- fuel or flame
g	- gas phase
i	- ith species or initial
ign, i	- ignition point
JP	- JP-10 (exo-tetrahydrodi) (cyclopentadiene)
l	- liquid
m	- mass transfer or molten
max	- maximum
min	- minimum
o	- oxidant or initial
ox	- oxide
p	- particle

r            - radial  
s            - surface  
surr         - laboratory surroundings  
T            - heat transfer  
v            - vapor

## I. INTRODUCTION

### 1.1 GENERAL PROBLEM STATEMENT

Slurry fuels have drawn substantial attention in recent years because of their versatility and potentially high energy content. Industrially, coal/water and coal/oil slurries are attractive because they are pumpable, can readily be used in conventional combustors with minimal equipment modifications and, more importantly, have the potential of substituting coal for oil as an energy source in the future. Militarily, slurry fuels for air-breathing propulsion systems are important because of their potential for greater energy release per unit volume compared to pure hydrocarbon fuels. A number of solid constituents, such as carbon, boron, aluminum, etc. have been considered for slurry fuels, each having unique potential benefits as well as unique problems. In the past several years, we have conducted research on carbon [1-4] and boron [5-6] slurries in our laboratories. The present work focuses attention on aluminum and aluminum-carbon slurries.

One attraction of formulating a slurry with aluminum arises from the fact that aluminum can burn in the vapor phase [7] similar to a hydrocarbon fuel. With flame temperatures approximately equal to the boiling point of the oxide  $Al_2O_3$ , aluminum vaporizes rapidly, thereby producing rapid combustion rates. However, a large number of studies of individual aluminum particles [8-19] or wires [20-24] have shown that aluminum ignition and combustion is in many ways more complex than hydrocarbon combustion. For example, the ignition of aluminum particles is related to the mechanical breakdown of an oxide coating, with ignition occurring only at relatively high temperatures that sometime approach the oxide melting point (ca 2300 K) [8,9,19]. Another complication which arises is that, although purely vapor-phase

burning with a detached envelope flame does occur in  $O_2/Ar$  atmospheres [7, 12-14], oxide condenses or is formed on the surface of aluminum droplets burning in air [12, 13]. This surface oxide relates to the frequently observed behavior of jetting, spinning, and fragmentation of burning aluminum droplets. A review of aluminum ignition and combustion problems is provided by Price [25].

Combustion studies of aluminum slurries, however, are much less numerous than for single aluminum particles, with attention primarily focused on ignition properties [26-28]. In the present study, ignition and combustion of aluminum-based slurry fuels were explored both experimentally and analytically. Specifically, the effects of droplet diameter, ambient gas temperature, ambient oxygen mole fraction, and slurry composition on ignition and combustion times were studied, together with the influence of these parameters on the mode of combustion and nature of the residual condensed products.

## 1.2 PREVIOUS RELATED STUDIES

### 1.2.1 Ignition of Single Aluminum Particles

The ignition of aluminum has been studied widely [8-10, 15-17, 19-24]. Some experiments have shown that a relatively high ambient gas temperature is required for ignition because of a protective oxide coating on the particle surface. However, other studies indicate that ignition can be achieved at temperatures well below the oxide melting point. Apparently, the detailed mechanism of ignition is strongly linked to specific test conditions, i.e., pressure, ambient composition, particle size, etc.

Friedman and Macek [8,9] studied the ignition behavior of aluminum

particles in 1962. Particles of diameter 10-74  $\mu\text{m}$  were injected into either  $\text{C}_3\text{H}_8/\text{O}_2/\text{N}_2$  flames (water vapor content of 14-18%) or  $\text{CO}/\text{O}_2/\text{N}_2$  flames (water vapor content about 0.5%) generated by a flat-flame burner operating at atmospheric pressure. It was found that ignition occurred only when the ambient gas temperatures were above 2210-2360 K and was quite insensitive to oxygen content and particle size. From these experimental observations, Friedman and Macek [8,9] concluded that the pre-ignition reaction was always controlled by diffusion through the oxide coating, and ignition occurred only when the oxide coating melted, not affected by the water vapor content of the ambient gas and only slightly by its oxygen content. Observations of Brzustowski and Glassman [20] supported this ignition mechanism, and further found that ignition temperature was independent of pressure (ranging from 50 mm Hg to 20 atm).

However, Kuehl in 1965 [22,23] reported different effects of pressure, oxygen concentration and water vapor content on ignition temperature. Kuehl [22,23] measured the minimum temperature for ignition of 508  $\mu\text{m}$  diameter aluminum wires over a pressure range of 20 mm Hg to 68 atm using optical pyrometry. A critical ignition pressure (about 100 to 250 mm Hg for the conditions studied) was defined above which ignition occurred as the oxide coating melted. Below the critical pressure the minimum wire temperatures required for ignition were substantially lower than the melting point of alumina. This implies that melting of the oxide coating is not the sole mechanism of ignition when the total pressure is below the critical value. For example, increased permeability and/or the rupturing of the oxide coating due to higher internal metal vapor pressure can reduce the ignition temperature. As far as ambient oxygen effects were concerned, below the critical ignition pressure, ignition temperatures increased

slightly at higher oxygen levels. Oxygen levels ranged from 30 to 100%. Kuehl [22, 23] also observed that a change in oxidizer from oxygen to water vapor produced a drastic decrease in the minimum wire temperature for ignition to values less than 1700 K, even at pressure far above the critical ignition pressure. This was postulated to result from a change from the normally protective oxide coating to a more permeable, less protective coating of a different chemical composition. Kuehl's observations [23] showed that below the critical ignition pressure the metal vapor pressure was more important than the oxide melting point in determining the ignition temperatures, and that the presence of water vapor in the ambient gas could change the properties of the oxide coating, and hence, reduce ignition temperatures. The effects of surface treatment on ignition of aluminum wires were studied by Mellor and Glassman [21, 24]

Gurevich et al. [15] found that ignition could occur over a wide range of temperatures (ca. 1000-2300) for 5-50  $\mu\text{m}$  diameter aluminum particles exposed to a hot stream of air or  $\text{O}_2/\text{Ar}/\text{N}_2$ . In addition, the minimum ambient temperature for ignition depended strongly on particle size and oxygen level. These results differ sharply from the observations of Friedman and Macek [8,9] both with respect to the absolute values of the ignition temperatures and with respect to the qualitative dependence on particle size. One probable reason for these differences, suggested by Khaikin et al. [29], was the different purities of the aluminum used in the various studies.

Derevyaga et al. [16] studied the ignition of 3-4 mm diameter aluminum particles in air at atmospheric pressure. Particle temperatures were measured with tungsten-rhenium thermocouples, while the appearance of a

flash was recorded with a photocell. It was found that some condensed reaction products were entrained into the air stream during the heat-up of the particles. The occurrence of ignition was characterized by a temperature jump, an increase in brightness, and also a visually observed sharp increase in the quantity of condensed products in the surrounding atmosphere. The particle temperatures at ignition in all cases were in the range  $2053 \pm 20$  K, somewhat lower than the melting point of alumina. The particle temperature at ignition did not rise even for the pre-oxidized particles on which the thickness of the oxide coating was accumulated up to 20  $\mu\text{m}$ . It was therefore suggested that the oxide coating becomes permeable at temperatures lower than the oxide melting temperature.

More recently, Ermakov et al. [19] measured the temperature of 400-1200  $\mu\text{m}$  diameter aluminum particles at the time of ignition using tungsten-rhenium thermocouples. Experimental results showed that the particle temperatures at ignition did not depend on the particle size in the range of these parameters studied. The particle ignition temperatures obtained were about 300 K below the oxide melting point, consistent with those of Derevyaga [16]. It was shown [19] that ignition was not related to the melting of the oxide coating, but was a result of the destruction of its integrity due to thermomechanical stresses arising during the heat-up process.

### 1.2.2 Combustion of Single Aluminum Particles

The combustion of aluminum also has been widely studied [7-14, 16-20, 22, 23]. Experiments have been conducted to acquire better knowledge of the combustion features and to determine the effects of important factors, such as particle size, oxygen level, composition of the ambient gas, etc.

Theoretical models also have been proposed to describe the experimental

observations and to predict the burning rate and/or burning time [9, 11, 30-35].

1.2.2.1 Experimental Studies - It is generally accepted that under the proper conditions aluminum can burn in the vapor phase, similar to a hydrocarbon fuel [7,20,22,23]. However, although purely vapor-phase combustion with a detached envelope flame does occur in dry O<sub>2</sub>/Ar atmospheres [7, 12-14], oxide condenses or is formed on the surface of aluminum droplets burning in air or in environments containing water vapor, nitrogen, carbon dioxide, carbon monoxide, etc. [9, 12-14]. The accumulation of the surface oxide complicates the combustion process and is related to the frequently observed behavior of jetting, spinning, and fragmentation of the burning aluminum droplets. Fragmentation of burning particles, which is observed in the presence of water vapor [14], is presumably related to oxide encapsulation of the molten aluminum. Nitrogen and carbon monoxide also have been suggested to be related to the fragmentation, while carbon dioxide does not seem to be involved [13].

Contradictory effects of the presence of water vapor on burning have been reported. Friedman and Macek [9] reported that the presence of moisture in the ambient gases increases burning times, while Prentice [14] reported the reverse effects.

The temperature of aluminum particles during combustion was measured in a few studies [16-19] with different results. Derevyaga et al. [16] measured temperatures of particles with diameters of 3-4 mm burning in air at atmospheric pressure using tungsten-rhenium thermocouples. The temperature during combustion was characterized by two stages: a high-temperature

stage and a low-temperature stage. The high-temperature stage occurred shortly after ignition with a constant temperature of 2430-2540 K; the low-temperature stage followed with a temperature equal to the melting point of  $\text{Al}_2\text{O}_3$ . Similarly, two-stage combustion of aluminum burning in air also was observed by Smelkov et al. [18]. The high temperature stage was in the range of the boiling point of Al (2767 K) and the low temperature stage ranged from 2320 to 2370 K, which is close to the melting point of  $\text{Al}_2\text{O}_3$ . The temperatures were measured using optical pyrometry for particles of diameters ranging from 1-3 mm.

Bouriannes [17] measured particle temperatures (3 mm diameter) in a 80%  $\text{CO}_2$ /20%  $\text{O}_2$  environment at 2 bars using both tungsten-rhenium thermocouples and an infrared optical pyrometer. According to the thermocouple measurements the temperature of a burning particle was also between the melting point of  $\text{Al}_2\text{O}_3$  and boiling point of Al (ca. 2900 K at 2 bars), with a maximum of 2600 K. However, Ermakov et al. [19] found that the temperatures of the burning particles maintained a constant value which was lower than the melting point of  $\text{Al}_2\text{O}_3$ . The W-Rh thermocouple measurements [19] were for aluminum particles having diameters from 400-1200  $\mu\text{m}$  burning in air at atmospheric pressure. No explanation was provided for these seemingly low temperatures.

1.2.2.2 Theoretical Models - Several theoretical models have been proposed to describe the combustion of single metal particles. They can be classified into three categories: vapor-phase combustion models [23, 30-34], surface combustion models [11], and a model considering the simultaneous existence of surface and vapor-phase combustion [35]. Experimental observations seemed to be more consistent with the vapor-phase

combustion models [7,13,20,22,23], although the surface combustion model can offer a natural explanation of fragmentation and the formation of oxide bubble products observed at some test conditions. Since oxide does form on part of or the whole surface of burning aluminum particles in most environments, impeding the vapor-phase combustion, a vapor-phase model considering the accumulation of oxide on the particle surface should be more reasonable.

Based on the vapor-phase theory for hydrocarbon droplet combustion, Brzustowski and Glassman [30] proposed a simplified model for metal particle combustion in which the flame temperature was assumed to be the boiling point of the metal oxide. This model was then modified by Kuehl [23] and Kuehl and Zwillenberg [31] to account for the condensation of vaporized products on the particle surface. Models also have been presented by Wilson [32] and Klyachko [33] to describe metal particle combustion. Law [34] presented a model which allowed oxide accumulation as a result of diffusion of dissociated oxide products to the surface of the burning aluminum droplet.

### 1.2.3 Aluminum Slurry Ignition

While considerable efforts have been made to understand the ignition and combustion of single aluminum particles, few fundamental combustion studies have been conducted for aluminum slurries, with attention primarily focused on ignition properties [26-28].

The minimum ambient gas temperatures for ignition of aluminum agglomerates formed after burn-out of a hydrocarbon carrier was studied as a function of aluminum loading (wt% of constituent particles in the slurry), constituent

particle size, and the concentration of thickening agent added to the slurry by Polishchuk et al. [26] and Velikanova et al. [27]. Pure kerosene and kerosene thickened with polyisobutylene in concentrations from 0 to 20% were used as the carrier. Aluminum loadings of the slurries were 20-100%, with constituent particle diameters ranging from 1 to 16  $\mu\text{m}$ . The most striking finding was the low minimum gas temperature required for aluminum agglomerate ignition compared to single aluminum particles. The minimum ambient temperatures as low as 930-1200 K, much lower than the melting point of  $\text{Al}_2\text{O}_3$  and somewhat higher than the melting point of Al, were obtained [26,27]. Gas temperatures depended strongly on both the aluminum loading and the concentration of thickening agent. A loading of 45% Al was found to exhibit a minimum value of ambient temperature; the presence of the thickening agent always reduced the minimum ambient temperature required for ignition.

Polishchuk et al. [28] presented a theoretical model dictating the critical condition for the ignition of aluminum agglomerates along with experimental data. This model accounted for the heat transfer from the hot ambient gas and the heat release from the surface oxidation on the constituent-particle surface, but neglected the heat loss through radiation. The theory predicted qualitatively the experimental observation that ignition temperature is lowered by increasing agglomerate diameter and decreasing constituent particle diameter.

### 1.3 OBJECTIVES

Since very few fundamental studies of the combustion characteristics of aluminum slurries have been performed, the present study was conducted. The specific objectives were the following:

- 1) Using both experiment and analysis, determine the effects of the following parameters on the ignition and burning times of slurry fuel droplets:
  - a) droplet diameter
  - b) ambient gas temperature
  - c) ambient oxygen mole fraction
  - d) slurry composition.
- 2) Determine the influence of the above parameters on the structure and composition of the accumulated products remaining after combustion.

## II. EXPERIMENTAL APPROACH

### 2.1 TEST APPARATUS

A flat-flame burner rig was used in the investigation to provide a wide range of hot-gas environments in which slurry droplet ignition and combustion could be studied. As shown in Fig. 1, the overall arrangement consisted of a flat-flame burner, a droplet support system, a flame shield, and a motion picture camera. In most cases a backlighting floodlight also was used. By rapidly withdrawing the flame shield, a slurry droplet could be exposed to the hot product gases. The subsequent events then were recorded with the motion picture camera.

Silicon carbide/carbon filaments manufactured by AVCO-Specialty Materials Division (Lowell, MA) were used to support slurry droplets because they were found to give satisfactory performance. In a CO/O<sub>2</sub>/N<sub>2</sub> test condition, combustion occurred with an envelope flame completely surrounding the agglomerate for essentially the entire combustion period, leaving white alumina residual on the SiC/C filaments. These 125 μm diameter SiC/C filaments were originally manufactured in 1973; testing of filaments of recent manufacture (SCS-2 and SCS-6) having a much higher proportion of SiC were found to be unsuitable because the molten aluminum did not wet the probe and fell off. Several other types of support probes were tried. Quartz fibers of diameter 100-200 μm were found to be unsuitable because of melting and balling after the aluminum ignited. When tungsten wires of 125 μm diameter were used as supporting probes, unstable envelope flames existed, which under certain conditions oscillated between complete and partial envelope flames. The residual material left on the probes appeared black and was frequently in the shape of a "bird's nest," suggesting that

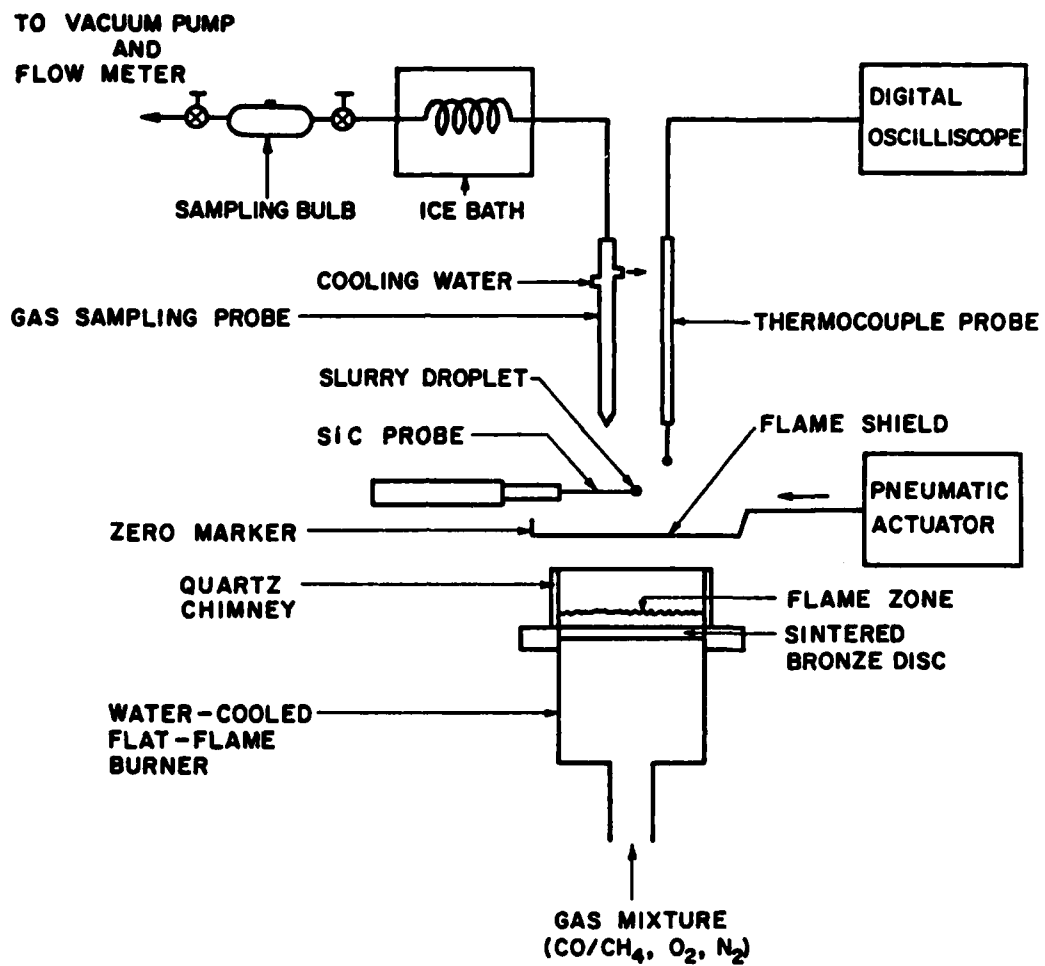


FIGURE 1. Schematic diagram of test rig and instrumentation.

the partial envelope flames were the result of the aluminum burning in the cup of the oxide "nests."

Mixtures of CO, CH<sub>4</sub>, O<sub>2</sub>, and N<sub>2</sub> were used to produce dry and wet environments. Oxygen and nitrogen flow rates were metered with Matheson models 604 and 605 rotameters, respectively. Carbon monoxide and methane flow rates were metered with Matheson model 603 rotameters. All rotameters were calibrated with a Precision Scientific Company wet-test meter. Gas pressure was monitored with a Heise absolute pressure gauge having a pressure range of 0.0-0.4 MPa. After leaving the rotameters, the gases were mixed while flowing through a 1.5 m length of 10 mm I.D. flexible tubing which carried the gas mixture to the base of the flat-flame burner. The burner, as sketched in Fig. 2, was constructed of brass and had an inside diameter of 50 mm. The mixed gases flowed from the bottom of the burner through two layers of steel wool separated by a perforated brass plate. A second perforated brass plate was located just below the porous sintered bronze disc at the top of the burner, where the flat flame was stabilized. Cooling water was run through a coil brazed to the block supporting the sintered disk around its circumference. A quartz chimney, 2.6 cm in length and 5.3 cm I.D., was used to prevent mixing of the burner gases with ambient air.

A 16 mm motion picture camera (Redlake Locam, model 51), capable of resolution up to 2 milliseconds, was used to record the processes of ignition and combustion. The camera was equipped with an LED timing marker powered by an external timing pulse generator. Kodak Plus-X reversal film was used for the tests. The film was developed as a negative by developing with Kodak D-19 developer solution for 6 minutes at 20°C with continuous

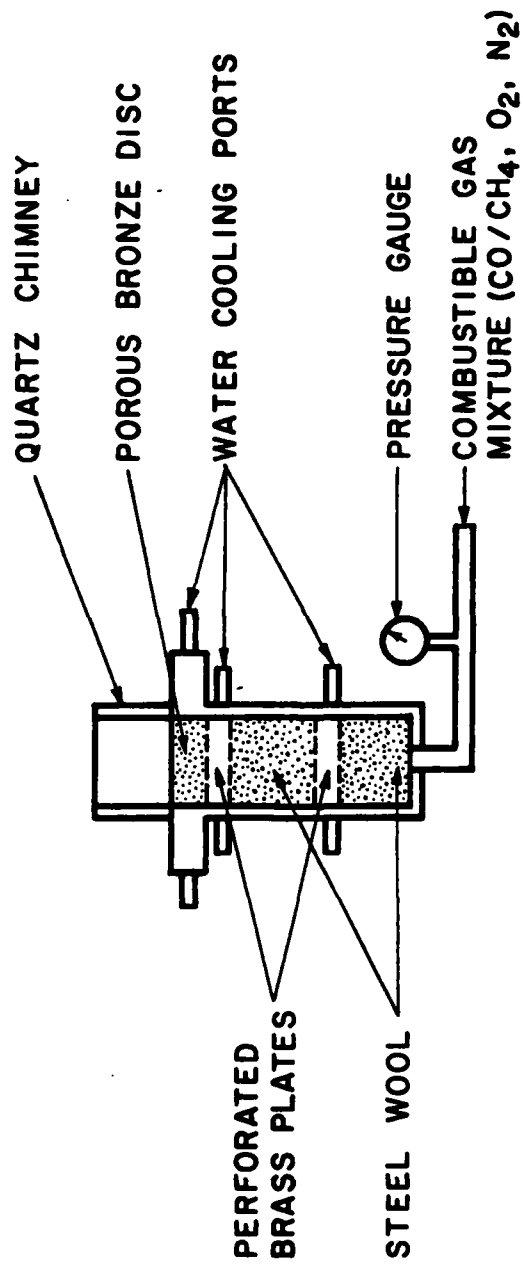


FIGURE 2. Schematic diagram of laminar premixed flat-flame burner.

winding and rewinding in the developing tank. Photographs were taken in either of two ways: with or without backlighting. For clear measurement of particle diameter, a 600 watt floodlight (Bogen Photo Corp.) was used as a backlight. In other cases, natural light photography was used for observation of the flame and/or the fragmentation of the burning particles. Photographs of an Edmund Scientific graticule provided the size calibrations for the particle diameter measurements. Calibration also was verified routinely using the cylindrical SiC/C slurry-droplet support probes. Particle sizes were obtained from the film records using a Vanguard/Bendix computer digitizing motion analyzer. The reported particle diameters were calculated as in past work by approximating the particles as ellipsoids [1]:

$$d = (d_{\min}^2 d_{\max})^{1/3}$$

where  $d$  is the reported diameter,  $d_{\max}$  and  $d_{\min}$  are the measured major and minor diameters of the particle, respectively. This approximation was found to be quite reasonable for aluminum and aluminum/carbon slurry droplets, with typical eccentricities ranging from 0.63-0.80.

The surface morphology of agglomerates and combustion residual products were investigated with a scanning electron microscope (International Scientific Instruments, model Super III-A). SEM micrographs were taken using Polaroid type 52 films.

The chemical composition of the combustion residual products found on the SiC probes was obtained by X-ray diffraction analysis. The small samples were mounted in Debye-Scherrer cameras, and diffraction patterns were taken

using CuK $\alpha$  radiation. Rough estimates of the relative portions of the phases present were made visually from the Debye-Scherrer photographs. Oxide smoke particles were collected on quartz slides and then photographed with an SEM. Particle size distributions were obtained by analyzing the SEM micrographs.

## 2.2 TEST CONDITIONS

Slurry droplets were tested both with and without water vapor present in the burner gases (wet and dry environments). All flame conditions used in this study were characterized by gas temperature, species concentrations and gas velocity at the particle test position. Normally, these parameters were controlled by adjusting the burner feed flow rates. However, gas temperatures lower than 1500 K could not be obtained solely by adjusting the flow rates because flames could not be stabilized at these conditions. Two methods were used to obtain gas temperatures lower than 1500 K. One method was to use a longer chimney tube which resulted in increased heat transfer over the standard chimney. This method, adopted for CH<sub>4</sub>/O<sub>2</sub>/N<sub>2</sub> flames yielded stable gas temperatures 100-150 K lower than the parent condition. The other technique to obtain lower temperatures was to place small steel screens on top of the standard quartz chimney. By using screens of different sizes and/or meshes, gas temperatures could be lowered to 1000-1430 K, principally as a result of radiation losses from the glowing screen. The latter method was applied for the lower-temperature dry conditions which were used to determine minimum ignition temperatures.

Gas temperatures at the test position were measured using 76  $\mu$ m diameter wire Pt/Pt-10% Rh thermocouples mounted on a support probe, as shown in Fig. 3. The thermocouples were manufactured by Omega Engineering, Inc. To

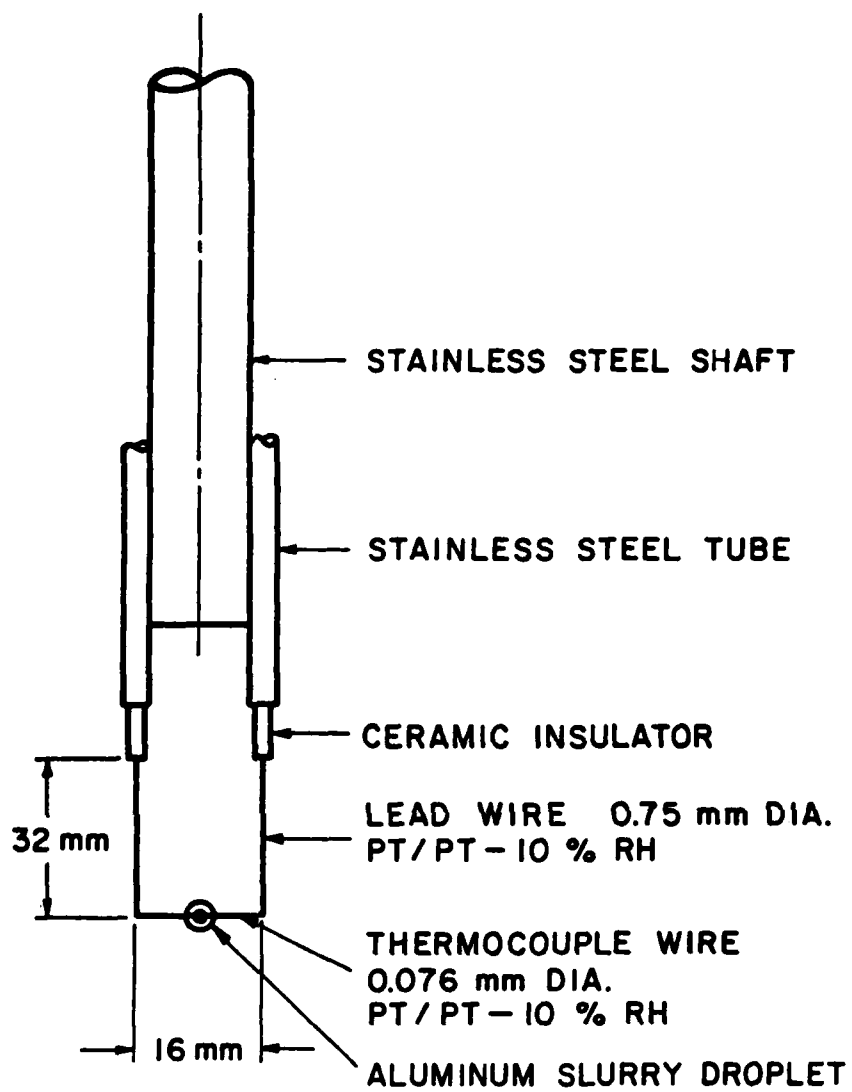


FIGURE 3. Schematic diagram of the thermocouple probe.

prevent catalytic effects, the thermocouples were protected with beryllium oxide-yttrium oxide coatings [37]. The bead diameters were approximately 210  $\mu\text{m}$  after coating. The signal from the thermocouples was recorded with a Nicolet Explorer III digital oscilloscope, transferred to a mainframe computer and converted to temperature records. Temperatures were then corrected for radiation losses assuming an emissivity of  $0.20 \pm 0.02$  [38-40] for the coated thermocouples.

Species concentrations were measured at the particle test position by analyzing samples withdrawn using the stainless steel water-cooled sampling probe shown in Figure 4. The probe was mounted on a Unislide traversing mechanism, which allowed sampling at any axial distance along the centerline of the burner. The water flow rate through the sampling probe was adjusted to maintain a probe temperature of about 340 K in order to avoid condensation of water vapor inside the probe. Water vapor in the sample was removed farther downstream by an ice-bath condenser, as shown in Fig. 1. The dry sample then flowed into a 125 ml sampling bulb (Supelco, model 2-2161), which was connected to a Welch Scientific duo-seal vacuum pump, model 1405. Sample flow rates were controlled with a Whitey regulating valve and metered with a bubble meter to ensure nearly isokinetic sampling at the probe inlet. The sample was drawn through the septum of the sampling bulb into a 1.0 ml series D Pressure-Lock gas syringe, and was analyzed using a Varian model 3700 gas chromatograph. The gas chromatograph was fitted with a Supelco Molecular Sieve 5A, 80/100 mesh, 0.91 m x 3.2 mm stainless steel column and a Chromosorb 102, 80/100 mesh, 1.82 m x 3.2 mm stainless steel column. The column temperature was maintained at 60°C. The GC was calibrated with Scott gas mixtures of known concentrations ( $\pm 2\%$ ) of nitrogen, oxygen, carbon monoxide and carbon

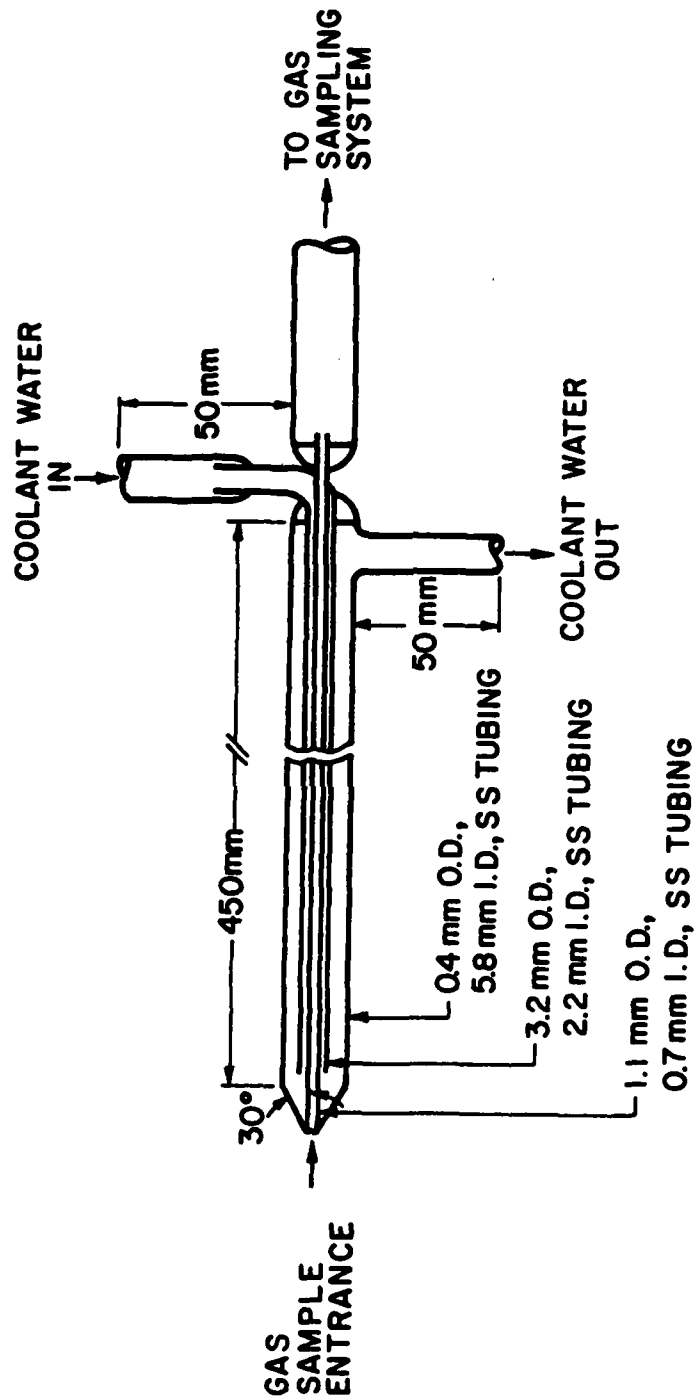


FIGURE 4. Schematic diagram of the water-cooled gas sampling probe.

dioxide. Helium was used as the carrier gas, having a flow rate of 0.6 ml/second.

For the test conditions using the 2.6 cm-long quartz chimney, gas velocities at the test section were calculated assuming one-dimensional flow of an ideal gas at the measured gas temperature. However, if a longer quartz chimney was used to lower the gas temperature, the gas velocity at the test position was calculated as a developing flow [41]. Summaries of the CO/O<sub>2</sub>/N<sub>2</sub> and CH<sub>4</sub>/O<sub>2</sub>/N<sub>2</sub> flame conditions used in this study are listed in Tables 1 and 2, respectively.

TABLE 1. Summary of CO/O<sub>2</sub>/N<sub>2</sub> Flame Conditions

$\phi$	$T_{\infty}$ (K)	$U_{\infty}$ (m/s)	Mole Fractions (%)				
			N <sub>2</sub>	O <sub>2</sub>	CO <sub>2</sub>	CO	H <sub>2</sub> O <sup>a</sup>
0.54	1510	0.32	69.5	10.0	22.3	0.05	0.25
0.59	1548	0.35	61.6	10.3	28.1	0.07	0.33
0.66	1659	0.44	53.8	10.4	35.5	0.14	0.39
0.58	1809	0.91	63.9	10.4	27.1	0.49	0.29
0.58	1868	0.86	54.0	11.4	31.2	0.57	0.34
0.58	1888	0.76	53.2	12.9	35.7	0.52	0.37
0.58	1869	0.69	47.4	13.8	38.4	0.41	0.38
0.37	1827	0.85	46.2	25.2	30.1	0.15	0.31
0.58	1907	0.97	63.9 <sup>b</sup>	10.4	27.1	0.49	0.29

<sup>a</sup> Water vapor concentrations were estimated using CEC 76 [42] and measured amounts of H<sub>2</sub> present in the fuel.

<sup>b</sup> Ar was used in place of N<sub>2</sub>.

TABLE 2. Summary of CH<sub>4</sub>/O<sub>2</sub>/N<sub>2</sub> Flame Conditions

$\phi$	$T_{\infty}$ (K)	$U_{\infty}$ (m/s)	Mole Fractions (%)				
			N <sub>2</sub>	O <sub>2</sub>	CO <sub>2</sub>	CO	H <sub>2</sub> O <sup>a</sup>
0.50	1417	1.09	68.7	10.9	6.2	0.0	12.4
0.50	1519	0.76	68.7	10.9	6.2	0.0	12.4
0.53	1547	1.41	70.3	10.9	6.2	0.0	12.5
0.58	1677	1.43	66.3	10.9	7.5	0.0	14.9
0.62	1785	2.15	65.4	10.3	8.1	0.0	16.2

<sup>a</sup> Water vapor concentrations were estimated using CEC 76 [42].

### 2.3 SLURRY SAMPLES

Three different aluminum-based slurries manufactured by Sun Refining and Marketing Company were investigated in this study. The basic compositions of these slurries are listed in Table 3.

TABLE 3. Slurry Samples

Slurry Designation	Additive	Mass Fraction (%)		
		Al	C	JP-10
Al/JP-10 (stabilized)	Surfactant/Gellant	42.6	—	57.4
Al/JP-10 (unstabilized)	—	42.0	—	58.0
Al/C/JP-10 (stabilized)	Surfactant/Gellant	35.5	9.3	55.2

### 2.4 TEST PROCEDURE

Slurry droplets of 400-1100  $\mu\text{m}$  diameter were tested in this study. Droplets supported by silicon carbide filaments were mounted horizontally above the flat-flame burner. Before the tests were started, the droplets were protected by the flame shield from the hot environment. By switching on the pneumatic actuator, the shield was quickly withdrawn leaving the

droplets exposed to the post-flame gases. The ignition and combustion of the droplets were photographed using the motion picture camera. Typical framing rates for these runs were around 50 frames per second. Both ignition times and combustion times were determined from these records. Particle diameters as a function of residence time in the post-flame gases were obtained from film records using the Vanguard/Bendix computer digitizing motion analyzer.

Slurry combustion products that remained on the probes were then investigated by SEM and X-ray diffraction analysis for each test condition. Information concerning surface morphology and chemical composition were obtained through these investigations.

Droplet temperatures during the heat-up stage were measured by burning the slurry droplets on Pt/Pt-10% Rh thermocouples. Again, the thermocouples were coated with BeO/Y<sub>2</sub>O<sub>3</sub>. The thermocouple voltage outputs as a function of time were recorded with a Nicolet oscilloscope until the thermocouples burned out at the high temperatures that occurred after ignition. The outputs were stored on floppy discs and thereafter converted to temperatures. Particle diameter versus time were simultaneously recorded by the motion picture camera. To synchronize the thermocouple outputs and the film records, the signal from the timing pulse generator was routed to the Nicolet oscilloscope as well as the LED time marker in the camera.

### III. THEORETICAL APPROACH

#### 3.1 AGGLOMERATE IGNITION MODEL

##### 3.1.1 Overview

Based on experimental observations, the history of an aluminum slurry droplet prior to ignition can be divided into four distinct stages as shown schematically in Fig. 5. In the first stage, the slurry droplet heats up as the liquid carrier (JP-10) burns. The droplet diameter either shrinks or remains essentially constant in this first stage, depending upon the slurry formulation. After the carrier is consumed, the porous aluminum agglomerate heats up to the melting point during stage two. The phase change occurs with the individual aluminum particles maintaining their integrity, ostensibly because of the ability of the thin oxide coating to reform and heal small cracks or ruptures [21,25]. The phase change is completed, during the third stage, and the still porous agglomerate continues to heat up. At some point, the oxide coating is insufficiently strong to contain the molten aluminium, and the particles begin to coalesce into a single drop. Coalescence occurs rapidly and is idealized as being instantaneous. With the completion of coalescence, vapor-phase combustion of the aluminum begins. Because of the relatively long time required for the agglomerate to heat to the point where coalescence begins (compared to the times required to complete coalescence and ignite the aluminium vapor), agglomerate ignition times are computed as the time from the introduction of the droplet into the hot gases to the beginning of agglomerate coalescence. A mathematical description of the processes up to ignition is given in the following sections.

# ALUMINUM SLURRY IGNITION MODEL

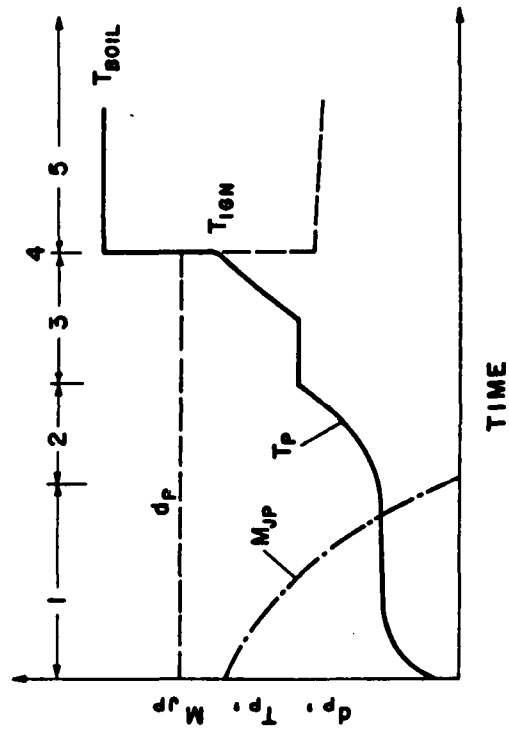
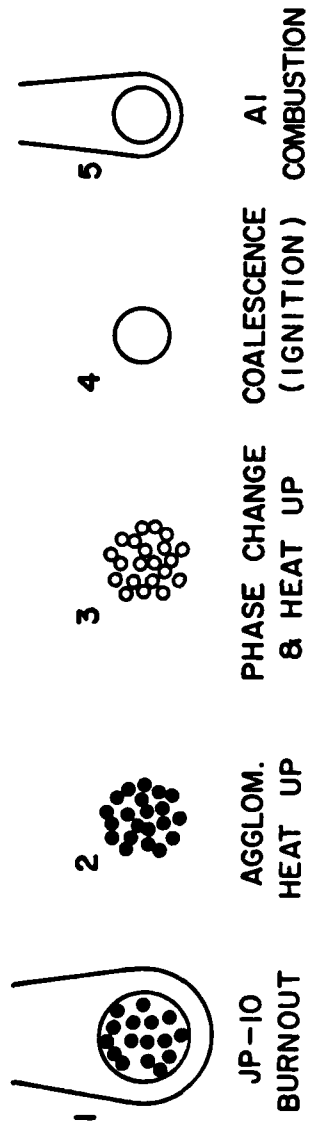


FIGURE 5. Aluminum slurry ignition model.

### 3.1.2 JP-10 Gasification

3.1.2.1 Assumptions - The basic approach taken to model the liquid evaporation and/or combustion follows the analysis of Faeth [43]. The major assumptions embodied in the model are as follows:

1. The gas phase is assumed to be quasi-steady, instantaneously adjusting to changing boundary conditions at the droplet surface.
2. Convective effects are treated using film theory for both heat and mass transport. Thus gas-phase transport is determined for a stagnant, spherically-symmetric boundary layer with an outer radius obtained from empirical convection correlations.
3. Solubilities of gas-phase species in the liquid phase are negligible.
4. The relationship between the gas-phase fuel concentration and the liquid temperature is given by the vapor-pressure correlation for the pure liquid. Surface tension effects are neglected.
5. Only diffusion by mass concentration gradients are considered, employing an effective binary diffusivity.
6. Constant average gas-phase properties are assumed at each instant and computed at a mean state defined as:

$$\phi_{avg} = \alpha \phi_s + (1 - \alpha) \phi_\infty \quad (1)$$

where  $\phi$  represents temperature and species mass fraction. Based on calibration tests with pure JP-10 (Appendix A), a value of 0.95 was used for  $\alpha$ .

7. Radiation is neglected until the gasification of the fuel is complete.
8. The Lewis number is assumed to be unity.

3.1.2.2 Gas-Phase Conservation Relations - Under the above assumptions, the basic conservation equations (eg., Williams [44]) become:

Mass:

$$\frac{d}{dr} (\rho r^2 v_r) = 0 \quad (2)$$

Species:

$$\frac{d}{dr} \left[ r^2 (\rho v_r Y_i - \rho D \frac{dY_i}{dr}) \right] = 0 \quad (3)$$

where: i=fuel, oxidizer and/or ambient gas

Energy:

$$\frac{d}{dr} \left[ r^2 (\rho v_r C_p (T - T_\infty) - k \frac{dT}{dr}) \right] = 0 \quad (4)$$

Integration of Eqn. (2) yields

$$r^2 \rho v_r = \dot{m}_f / 4\pi = \text{constant} \quad (5)$$

where  $\dot{m}_f$  is the mass gasification rate of the liquid fuel.

In the absence of an envelope flame (i.e., pure evaporation), the appropriate boundary conditions for species and energy conservation are

Droplet Surface:

$$T(r_s) = T_s \quad (6a)$$

$$Y_f(r_s) = Y_{fs} \quad (6b)$$

$$\left[ \rho v_r Y_a - \rho D \frac{dY_a}{dr} \right]_{r_s} = 0 \quad (6c)$$

Outer Edge of Film:

$$T(r_{\infty, T}) = T_{\infty} \quad (6d)$$

$$Y_f(r_{\infty, m}) = 0 \quad (6e)$$

$$Y_a(r_{\infty, m}) = 1 \quad (6f)$$

where the film radius for heat and mass transfer are defined as:

$$\frac{r_{\infty, T}}{r_s} = \frac{Nu}{Nu-2}, \quad \frac{r_{\infty, m}}{r_s} = \frac{Sh}{Sh-2}, \quad (7)$$

The Nusselt and Sherwood numbers were defined using the following correlation [43]:

$$Nu \text{ or } Sh = 2 + \frac{0.552 Re^{1/2} (Pr \text{ or } Sc)^{1/3}}{\left\{ 1 + 1.232 / [Re (Pr \text{ or } Sc)^{4/3}] \right\}^{1/2}} \quad (8)$$

The boundary condition represented by Eqn. (6c) results from the assumption of insolubility of the ambient gases in the liquid.

The fuel mass fraction at the droplet surface  $Y_{fs}$ , was computed using the JP-10 vapor-pressure correlation given in [1],

$$P_{JP} = 3.069 \cdot 10^9 \exp \left[ - \frac{4704.2}{T(K)} \right] \text{ [ = ] Pa} \quad (9)$$

and

$$Y_f = \frac{P_{JP}}{P} \frac{MW_f}{MW} \quad (10)$$

where the average molecular weight of the binary mixture of fuel and ambient gases is given by:

$$\frac{1}{MW} = \frac{Y_f}{MW_f} + \frac{1-Y_f}{MW_a} \quad (11)$$

Solution of Eqns. (2) and (3) subject to Eqns. (6a)-(6c) results in the following:

$$\dot{m}_f = 2\pi r_s \text{ Sh } \rho D \ln[1 + B_y] \quad (12)$$

$$q_c = 2\pi r_s (T_\infty - T_s) \text{ Nu } k \ln [(1 + B_y)/B_y] \quad (13)$$

where

$$B_y = Y_{fs}/(1-Y_{fs}) \quad (14)$$

If an envelope flame surrounds the droplet, two regions separated by an infinitesimally thin flame zone are defined. In the inner region, fuel diffuses from the droplet surface through the stagnant gases to the flame zone where it is totally consumed. In the outer region, oxygen diffuses inward and is consumed at the flame in stoichiometric proportions. To solve this problem, the basic conservation Eqns. (2)-(4) are solved for each region with appropriate boundary conditions at the flame sheet position. Following Faeth's [43] approach to this problem yields the following solutions:

$$\dot{m}_f = 2\pi r_s \rho D \text{ Sh } \ln [(1 + B_y) (1 + B_o)] \quad (15)$$

and

$$q_c = 2\pi r_s k Nu (T_f - T_s) \frac{1}{B_y} \ln [(1 + B_y) (1 + B_o)] \quad (16)$$

where

$$B_o = v_f Y_{O,\infty} \quad (17)$$

with the flame temperature defined by

$$\frac{T_f - T_s}{T_\infty - T_s} = \left( \frac{B_o Q_f}{C_p (T_\infty - T_s)} + 1 \right) / \left( 1 + \frac{B_o}{B_y} (B_y + B_o) \right) \quad (18)$$

The heat of combustion of the fuel,  $Q_f$ , was taken to be 41.9 kJ/kg for JP-10 [45].

3.1.2.3 Liquid-Phase Conservation Relations - To determine the mass of JP-10 at any instant, the following mass conservation expression was integrated

$$\frac{dm_f}{dt} = -\dot{m}_f \quad (19)$$

The initial JP-10 mass was computed from the experimentally-determined initial droplet diameter and knowledge of the mass fraction of the aluminum in the slurry, i.e.,

$$m_{f,i} = (1 - f_{Al}) \left[ \frac{f_{Al}}{\rho_{Al}} + \frac{1-f_{Al}}{\rho_f} \right]^{-1} \frac{4\pi}{3} r_{s,i}^3 \quad (20)$$

A density of 2702 kg/m<sup>3</sup> was used for the aluminum, while the following correlation [1] was used for the JP-10 density:

$$\rho_f = 1166.4 - 0.792 T_s [=] \text{ kg/m}^3 \quad (21)$$

where  $T_s$  has units of Kelvins.

For the case of the shrinking slurry droplet, the instantaneous droplet radius can be obtained as a function of the mass of liquid remaining as follows:

$$r_s = \left[ \frac{3}{4\pi} \left( \frac{m_{Al}}{\rho_{Al}} + \frac{m_f}{\rho_f} \right) \right]^{1/3} \quad (22)$$

where

$$m_{Al} = \frac{f_{Al}}{1-f_{Al}} m_{f,i} \quad (23)$$

Equation (22) is used until sufficient evaporation has occurred such that the individual spherical aluminum particles touch, after which no further shrinking occurs. The minimum diameter occurs at this point and is computed from the experimentally or theoretically determined agglomerate porosity,  $\theta$ , as follows:

$$d_{min} = \left( 6 m_{Al} / [\pi \rho_{Al} (1-\theta)] \right)^{1/3} \quad (24)$$

Experimentally, the porosity of slowly-dried agglomerates was found to be approximately 0.4.

To determine the slurry droplet temperature history, it was assumed that the liquid/solid system behaved as a single lump. With this assumption, conservation of energy for the system can be expressed:

$$(m_{Al} C_{p,Al} + m_f C_{p,f}) \frac{dT}{dt} = q_c - \dot{m}_f L \quad (25)$$

where the heat of vaporization of the fuel L was taken to be 286.7 kJ/kg [1].

The integration of Eqns. (19) and (25) to yield the mass and temperature history of the slurry droplet during the liquid gasification stage was performed numerically using the IMSL routine DVERK [46].

### 3.1.3 Dry Agglomerate Heat-Up

3.1.3.1 Assumptions - During the time which the liquid fuel evaporates and burns, the aluminum particles in the slurry droplet are assumed to be in equilibrium with the fuel liquid. Thus after the initial droplet heat-up period, the aluminum particles are at the fuel wet-bulb temperature, a temperature somewhat less than the 459 K boiling point of JP-10. After the disappearance of the fuel, the following major assumptions were applied to the agglomerate heat-up:

- 1) Temperature gradients within the agglomerate are negligible with the system treated as a single "lump."
- 2) Chemical reaction of the aluminum particles is negligible.
- 3) The convective heat transfer to the porous agglomerates is assumed to exceed that of an equivalent diameter solid sphere. This effect is taken into account by utilizing an empirical multiplicative correction to the Nusselt number, as has been done in past studies of carbon slurry agglomerates [2-5].

The validity of the first assumption can be tested by examining the Biot number of the agglomerate. The usual engineering criterion for "lumpedness" is a Biot number less than 0.1. For the porous agglomerate,

the Biot number is defined in terms of an effective thermal conductivity,  $k_e$ , as follows:

$$Bi = \frac{1}{6} \left( \frac{k_g}{k_e} \right) Nu \quad (26)$$

Using the Krupiczka correlation [47], the effective conductivity can be computed from the agglomerate porosity and the thermal conductivities of the solid and gaseous phases which make up the agglomerate:

$$k_e = k_g \left( k_{Al}/k_g \right)^n \quad (27)$$

where

$$n = 0.280 + 0.757 \log_{10} \theta + 0.057 \log_{10} (k_{Al}/k_g) \quad (28)$$

The validity of the lumped assumption for the range of agglomerate porosities encountered experimentally can be judged from the results shown in Table 4.

TABLE 4  
Test for Agglomerate Lumpedness <sup>a</sup>

Porosity, $\theta$	n	Bi/Nu	Nu <sub>max</sub> (Bi=0.1)
0.80	0.146	0.0490	2.04
0.40	0.374	0.0073	13.7

<sup>a</sup> Conductivities for aluminum and air were evaluated at a mean value of the JP-10 boiling point and aluminum melting point, i.e. 692K.

From the table it can be seen that the lumped approximation appears to be valid for the low-porosity ( $\theta=0.4$ ) agglomerates, since Nusselt numbers in the experiments were typically between 2 and 4. On the other hand, for the very porous agglomerates ( $\theta=0.8$ ), the maximum Nu for Bi=0.1 is at the lower end of the experimental range. Nevertheless, departures from the assumption of a uniform temperature do not appear to be particularly severe.

3.1.3.2 Energy Conservation - In the absence of chemical effects, the agglomerate temperature up to the aluminum phase change is controlled by the combined effects of convection and radiation as given below.

$$m_{Al} C_{p,Al} \frac{dT}{dt} = q_c - q_r \quad (29)$$

where

$$q_c = \pi d_p^2 \bar{h} (T_\infty - T), \quad (30)$$

$$q_r = \pi d_p^2 \epsilon \sigma (T^4 - T_{surr}^4) \quad (31)$$

with the convective heat transfer coefficient defined as:

$$\frac{\bar{h}d_p}{k} = \xi Nu \quad (32)$$

where  $\xi$  is the empirical transport enhancement factor. The correlation given by Eqn. (8) was used to evaluate the Nusselt number. The agglomerate emissivity was assumed to be unity because of the highly porous nature of the surface.

When the aluminum particles composing the agglomerate reach the melting point (933.1K), two possibilities exist: First, the individual particles may coalesce as they melt, forming a single droplet when the melting is complete. The second possibility is that as the individual particles melt, the thin oxide coating is sufficiently strong to withstand the volumetric expansion (ca 6%), or is self healing, such that the agglomerate retains its identity as an aggregate of small individual particles. In the experiments, this second possibility was observed. In either case, the time required to complete the melting of all particles can be obtained by evaluating the difference between the upper and lower limits of the following integral:

$$m_l L = \int_t^{t+m} (q_c + q_r) dt \quad (33)$$

where  $t$  is the time at which melting first begins, and  $m_l$  is the total mass of liquid equal to the initial mass of the agglomerate. In the absence of coalescence, evaluation of the integral is straightforward because the heat-transfer rates are fixed by the constant agglomerate

diameter and constant temperature. If coalescence occurs, the time-dependent diameter needed to calculate the heat-transfer rates can be estimated from the instantaneous value of the mass of molten metal

$$d_p = \left\{ \frac{6}{\pi} \left[ \frac{m_l}{\rho_{Al(l)}} + \frac{(m_{Al} - m_l)}{\rho_{Al(s)} (1-\theta)} \right] \right\}^{1/3} \quad (34)$$

Upon completion of the phase change, the temperature history of the molten particles (or particle) continues as expressed by Eqn. (29).

To evaluate the transport enhancement factor, the procedure schematically illustrated in Fig. 6 was used as follows: Equilibrium (steady-state) agglomerate temperatures  $T_e$  were computed as a function of  $\xi$  for the test conditions found at the ignition limit, i.e., minimum gas temperature where ignition occurred (Fig. 6A). Agglomerate temperature histories also were computed for a test condition where ignition was readily achieved using various values of  $\xi$  (Fig. 6B). Temperatures corresponding to the observed "ignition time",  $t_i$ , for the igniting particles, and equilibrium temperatures for the ignition-limit condition, match at a unique value of  $\xi$ , thereby determining both the transport enhancement factor and an apparent ignition temperature.

It should be pointed out that this concept of ignition and ignition temperature differs considerably from the usual definitions which result from a stability analysis of a reacting system [48]. With the present assumption of no chemical reaction, "ignition" is modeled as the point at which the oxide coating is too weak to contain the readily oxidized molten aluminum. Obviously, the real process of ignition is quite complicated and

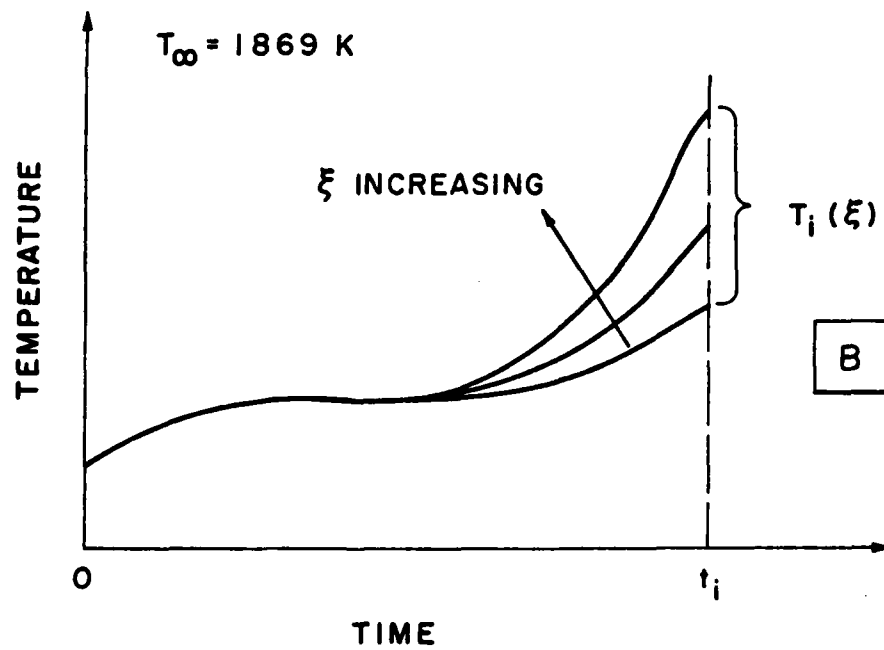
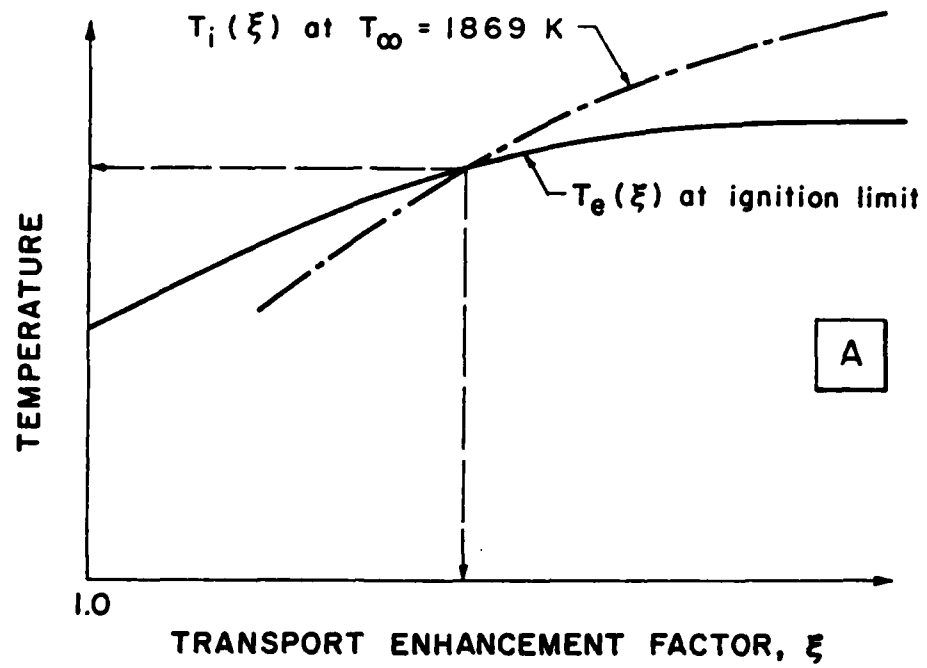


FIGURE 6. Schematic diagram illustrating method to determine transport enhancement factors.

a detailed knowledge of the chemical and mechanical properties of the oxide, together with the appropriate aluminum reaction kinetics, would be required for a comprehensive model. Therefore, the present analysis should be viewed as a first step in the modeling of agglomerate ignition.

## 3.2 ALUMINUM COMBUSTION MODEL

### 3.2.1 Overview

Experimental observations showed that after coalescence of the particles constituting the agglomerate, combustion generally proceeded with an axisymmetric, detached flame surrounding the aluminum droplet.

Furthermore, surface accumulation of oxide on the leeward side was observed.

To model this combustion process with a minimum of complexity, the theoretical vapor-phase combustion analysis of Law [34] was adapted and extended. This extended model is schematically illustrated in Fig. 7.

### 3.2.2 Assumptions

The basic assumptions embodied in the model are as follows:

1. Reactions between the aluminum vapor and oxidizer occur instantaneously at the flame sheet surrounding the particle. The flame temperature is at the oxide boiling point (3850 K).
2. The surface temperature is at the aluminum boiling point (2767 K).
3. Radial symmetry is assumed, and asymmetric forced convection effects are treated using film theory (Eqn. 7).

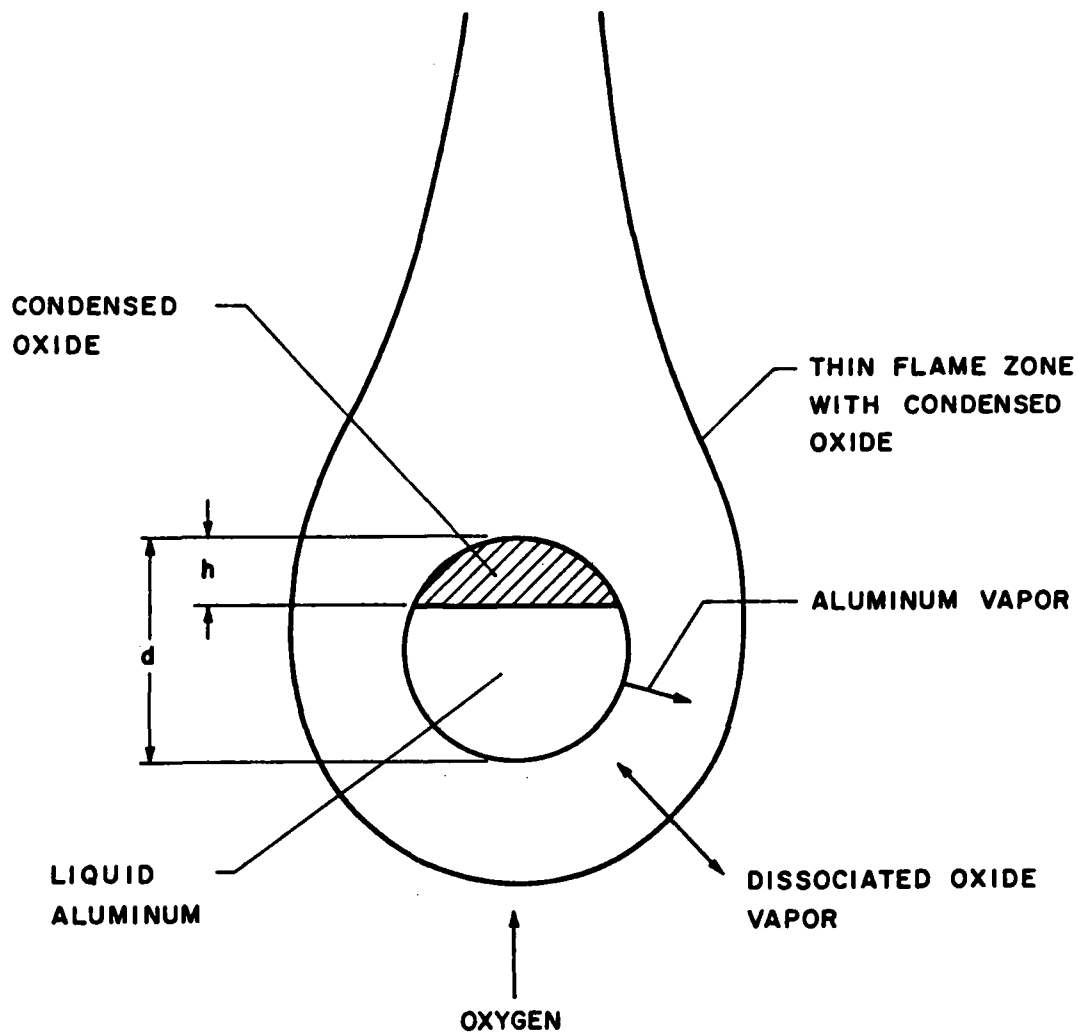


FIGURE 7. Aluminum combustion model incorporating oxide accumulation.

4. Oxide condensed in the flame zone is either convected away ( $\zeta_2=0$ ) or is trapped in the flame ( $\zeta_2=1$ ).
5. Gas phase properties are treated as described in the ignition model with properties of aluminum vapor taken from Svehla [49]. The Lewis number is taken to be unity.
6. The oxide vapor, defined as  $\text{Al}_2\text{O}_3(\text{g}) = 2 \text{AlO}(\text{g}) + 1/2 \text{O}_2$ , that is convected to the droplet surface condenses at the surface and accumulates, forming a spherical segment with height  $h$  on the leeward side of the droplet. (Fig. 7).
7. The presence of the oxide cap does not alter the spherical symmetry assumption of Law's combustion model [34]; thus the combustion rate of the aluminum is equal to the ratio of exposed area to total surface area multiplied by the burning rate computed for a sphere having the same diameter as the combined oxide-aluminum particle.

### 3.2.3 Gas Phase Mass Conservation

The relationship among the fuel vapor, oxidizer, and combustion products mass fluxes are illustrated in Fig. 8. Following Law's notation [34],  $M_{\text{Al}}$  is the dimensionless fuel aluminum vapor mass flow rate. At the flame, fuel and oxidizer meet in stoichiometric proportions,  $v$ . In the flame, a certain fraction,  $\theta$ , of the oxide is vaporized to maintain the flame temperature at the oxide boiling point. A fraction,  $\eta$ , of the vapor

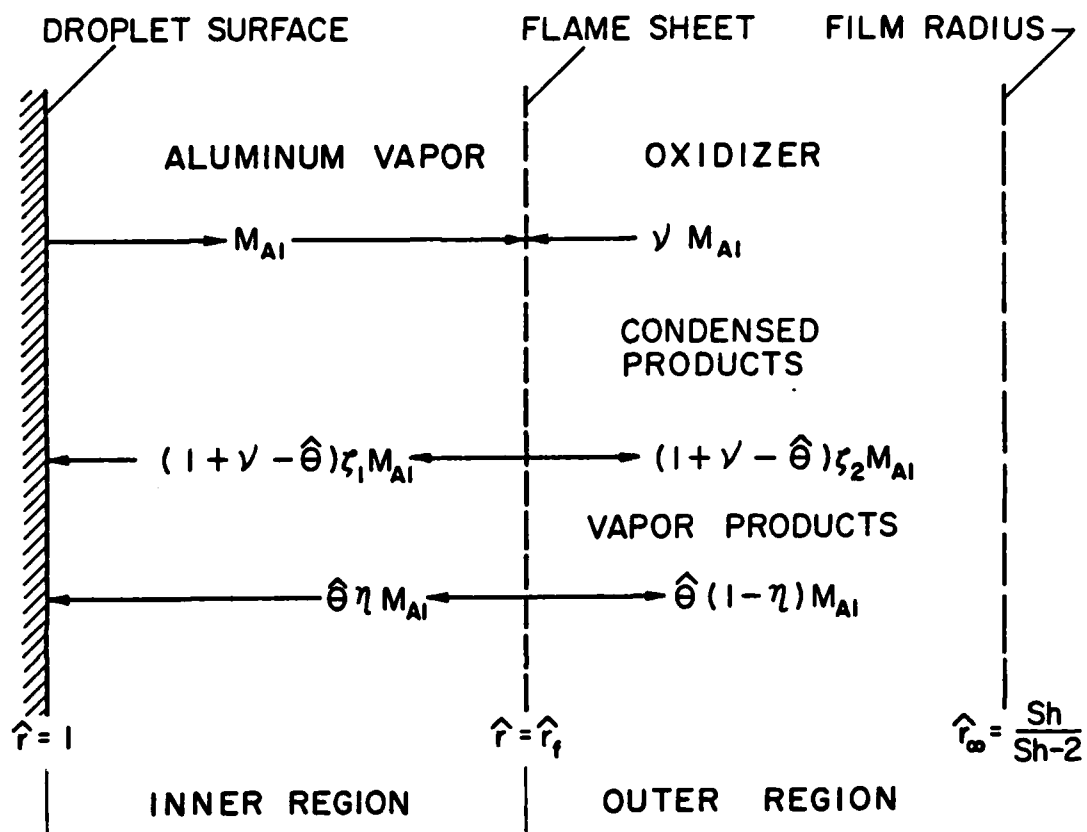


FIGURE 8. Mass fluxes of fuel, oxidizer, and combustion products used in the combustion model.

products diffuse inward to condense at the surface, while the remainder,  $1-\eta$ , move radially outward. Depending upon the directions of mean velocities in the inner region ( $1 < r < r_f$ ) and the outer region ( $r > r_f$ ), the condensed products are either trapped in the flame, ( $\zeta_2 = 0$ ), or are convected away ( $\zeta_2=1$ ). In general, a third mode is possible where condensed products are convected to the surface ( $\zeta_1=1, \zeta_2=0$ ); however, for aluminum combustion this mode does not occur. Law [34] has shown that the following inequality constraints must be satisfied for a solution to exist in each mode, respectively:

$$\zeta_1 = \zeta_2 = 0:$$

$$\begin{aligned} \max [0, (1-\nu/\hat{\theta})] < \eta < \min [1, 1/\hat{\theta}], \\ 0 < \hat{\theta} < (1+\nu) \end{aligned} \quad (35)$$

$$\zeta_1 = 0; \zeta_2 = 1:$$

$$0 < \eta < (1-\nu/\hat{\theta}), \quad \nu < \hat{\theta} < (1+\nu) \quad (36)$$

In the implementation of the combustion model, a particular mode of combustion was assumed, i.e. either  $\zeta_2=0$  or 1, and the appropriate constraints tested each time a new burning rate was evaluated. If a constraint was violated, the alternative mode of combustion was selected, and the burning rate reevaluated.

The bulk total mass flow and the bulk gaseous mass flow in the inner and outer regions, made dimensionless by division by  $4\pi\rho D r_s$ , are [34]

$$M_1 = [1-\hat{\theta}\eta - (1+\nu-\hat{\theta}) \zeta_1] M_{Al} = F_1 M_{Al} \quad (37)$$

$$M_{g,1} = [1 - \hat{\theta}\eta] M_{Al} \quad (38)$$

$$M_2 = [-\nu + \hat{\theta}(1-\eta) + (1+\nu-\hat{\theta})\zeta_2] M_{Al} = F_2 M_{Al} \quad (39)$$

$$M_{g,2} = [-\nu + \hat{\theta}(1-\eta)] M_{Al} \quad (40)$$

where the subscripts 1 and 2 designate the inner and outer regions, respectively.

#### 3.2.4 Species Conservation

Assuming that the volume occupied by any condensed oxide is small, the dimensionless diffusion equation for the  $i^{\text{th}}$  gaseous species (aluminum, products, or oxygen) can be expressed (cf. Eqn. 2)

$$M_i = MY_i - \hat{r}^2 \frac{dY_i}{d\hat{r}} \quad (41)$$

The general solution to Eqn. (41), employing flame conditions at the boundary, is

$$M(\hat{r}^{-1} - \hat{r}_f^{-1}) = \ln [(MY_{i,f} - M_i)/(MY_i - M_i)] \quad (42)$$

where the subscript  $f$  refers to the flame.

Equation (42) can be evaluated in the inner region for the aluminum vapor and products vapor. Applying the boundary conditions

$$r = r_s: \quad Y_{Al} = Y_{Al,s}, \quad Y_v = 0 \quad (43)$$

$$r = r_f: \quad Y_{Al} = 0, \quad Y_v = Y_{v,f} \quad (44)$$

yields the following two species conservation relations

$$M_{Al} F_1 (1 - \hat{r}_f^{-1}) - \ln [1 + F_1 Y_{v,f} / (\hat{\theta}\eta)] = 0 \quad (45)$$

$$M_{Al} F_1 (1 - \hat{r}_f^{-1}) + \ln [1 - F_1 Y_{Al,s}] = 0 \quad (46)$$

In the outer region, a similar procedure can be applied to yield relations involving the oxygen and vapor products. To include forced convection effects, the outer boundary of the outer region is defined by the film radius for mass transfer (Eqn. 7). The appropriate boundary conditions are

$$r = r_f: \quad Y_o = 0, \quad Y_v = Y_{v,f} \quad (47)$$

$$r = r_{\infty,m}: \quad Y_o = Y_{o,\infty}, \quad Y_v = 0 \quad (48)$$

Applying these conditions to Eqn. (42) yields

$$M_{Al} F_2 \left[ \frac{Sh-2}{Sh} - \frac{1}{\hat{r}_f} \right] - \ln \left[ 1 - \frac{F_2 Y_{v,f}}{\hat{\theta}(1-\eta)} \right] = 0 \quad (49)$$

$$M_{Al} F_2 \left[ \frac{Sh-2}{Sh} - \frac{1}{\hat{r}_f} \right] + \ln \left[ 1 + \frac{F_2 Y_{o,\infty}}{v} \right] = 0 \quad (50)$$

### 3.2.5 Energy Conservation

Conservation of energy in the region surrounding the burning aluminum droplet can be expressed in dimensionless form as [34].

$$\int M_1 \hat{h}_1 - r^2 \frac{dT}{dr} = H_1 \text{ or } H_2 = \text{constant} \quad (51)$$

where  $H_1$  and  $H_2$  are the total energy fluxes in the inner and outer regions, respectively. This form of energy conservation assumes that all radiation effects can be treated as boundary phenomena at the particle surface and at

the flame sheet. The constant  $H_1$  can be determined by evaluating Eqn. (51) at  $T_s$  and applying the following boundary condition:

$$4\pi r_s^2 k \left( \frac{dT}{dr_s} \right) = -4\pi r_s^2 q''_{r,s} + \dot{m}_{Al} \left( L - \hat{\theta} \eta \frac{Q_2}{1+\nu} \right) \quad (52)$$

where  $q''_{r,s}$  is the net radiant flux to the droplet surface,  $L$  is the heat of vaporization, and  $Q_2$  is the heat of condensation for the vapor per unit mass of aluminum. Defining a dimensionless radiant flux as

$$\hat{Q}_{r,s} = \frac{q''_{r,s} r_s}{\rho D L} \quad (53)$$

$H_1$  can be given by

$$H_1 = M_{Al} \left[ (\hat{\theta} \hat{Q} - 1) + (1 + \nu - \hat{\theta}) \hat{Q} \zeta_1 \right] + \hat{Q}_{r,s} \quad (54)$$

where  $\hat{Q}$  is sum of the heat of reaction ( $Q_1$ ) and  $Q_2$  expressed in dimensionless form. In Law's [34] original combustion model, radiation was neglected; thus, use of Eqn. (54) extends the analysis to include radiation effects.

Beyond the flame zone, the total energy flux is modified by the loss associated with any condensed oxide which may be trapped in the flame and, secondly, by the net radiation from the particles at the flame location. Thus, the enthalpy flux in the outer region can be expressed

$$H_2 = H_1 + \hat{Q}_{r,f} - M_{Al} (1 + \nu - \hat{\theta}) (-\hat{Q} + a) (1 - \zeta) \quad (55)$$

where  $\hat{Q}_{r,f}$  is the dimensionless radiant gain by the flame sheet,  $a = T_f - T_s$ , and  $\zeta = \zeta_1 + \zeta_2$ .

To evaluate the radiant fluxes the situation illustrated in Fig. 9 was considered. Assuming that the radiation from the relatively cold surroundings is negligible, the radiosity at the droplet surface consists of gray body emission together with the reflection of the incident flux, resulting from emission at the flame. In the flame, it is assumed that the individual radiating particles are black, thus the flame reflectance is zero. Performing radiant energy balances at the droplet surface and at the flame yields

$$q''_{r,s} = \epsilon_s \epsilon_f \sigma T_f^4 - \epsilon_s \sigma T_s^4 \quad (56)$$

and

$$q''_{r,f} = \epsilon_f \left( \epsilon_s \left( \frac{r_s}{r_f} \right)^2 \sigma T_s^4 + \left[ \epsilon_f (1 - \epsilon_s \left( \frac{r_s}{r_f} \right)^2) - 2 \right] \sigma T_f^4 \right) \quad (57)$$

To evaluate Eqns. (56) and (57), estimates of the total emissivity of both the particle and flame are required. Radiative properties for  $Al_2O_3$  are available in Touloukian [50], while the emissivity of molten aluminum can be found in Hu [51]. Radiative properties of the flame depend upon both the size and number of particles in the flame zone as well as the true flame geometry. The effect of the flame emissivity was studied parametrically as will be shown in a subsequent section.

Equation (51) can now be integrated subject to the following boundary conditions for the inner and outer regions:

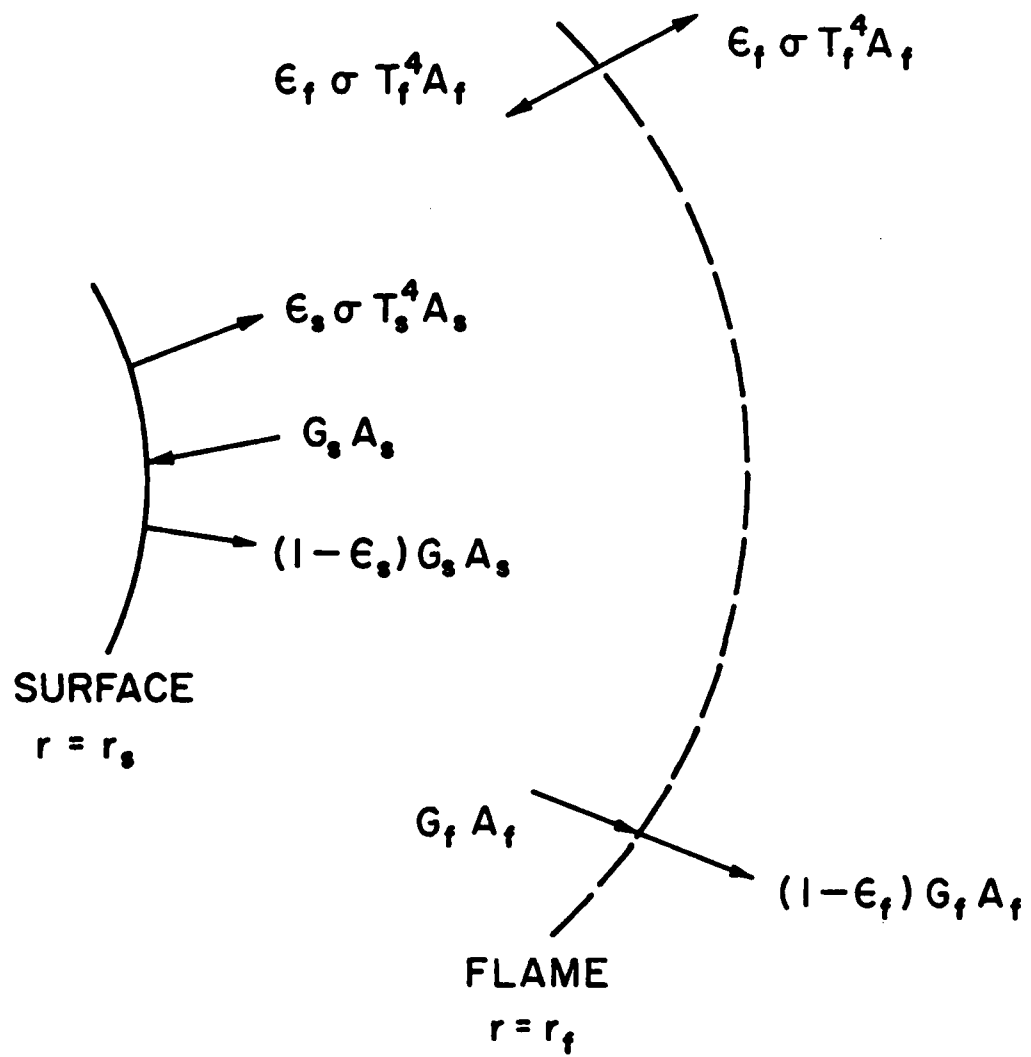


FIGURE 9. Radiant fluxes at the burning droplet surface and at the flame zone.

$$r = r_s: \quad T = T_s \quad (58)$$

$$r = r_f: \quad T = T_f \quad (59)$$

$$r = r_{\infty, T}: \quad T = T_{\infty} \quad (60)$$

The resulting solutions are

$$M_{Al} F_1 \left[ 1 - \frac{1}{\hat{r}_f} \right] - \ln \left[ 1 - \frac{aF_1}{\psi_1} \right] = 0 \quad (61)$$

$$M_{Al} F_2 \left[ \frac{Nu-2}{Nu} - \frac{1}{\hat{r}_f} \right] + \ln \left[ 1 - \frac{bF_2}{(aF_2 - \psi_2)} \right] = 0 \quad (62)$$

where  $F_1$  and  $F_2$  are defined in Eqns. (37) and (39), respectively,  $b = T_f - T_{\infty}$ , and

$$\psi_1 = \hat{\theta} \eta \hat{Q}_2 - 1 - \hat{Q}_{r,1}/M_{Al} \quad (63)$$

$$\psi_2 = \hat{\theta} (1-\eta) \hat{Q}_1 + (\hat{\theta}\eta\hat{Q}-1) + (1+\nu-\hat{\theta})[\hat{Q}-a(1-\zeta)] + (\hat{Q}_{r,1} + \hat{Q}_{r,2})/M_{Al} \quad (64)$$

### 3.2.6 Particle Mass Conservation

As illustrated in Fig. 7, the burning particle is assumed to be spherical with a partition of the molten aluminum and molten oxide into two spherical segments. The mass rate at which the aluminum is consumed is proportional to the exposed surface area of the molten aluminum and the mass burning rate per unit area determined by the gas-phase conservation relationships, i.e. Eqns. (45), (46), (49), (50), (60), and (61). From the definition of

the dimensionless burning rate  $M_{Al}$ , the mass rate of aluminum consumption per unit surface area is

$$\dot{m}''_{Al} = \rho D M_{Al} / r_s \quad (65)$$

Thus, the quasi-steady rate of change of aluminum volume can be expressed

$$\frac{dV_{Al}}{dt} = - 4\pi r_s^2 \left(1 - \frac{h}{2r_s}\right) \dot{m}''_{Al} / \rho_{Al} \quad (66)$$

where  $h$  is the height of the oxide cap illustrated in Fig. 7. As the aluminum is depleted, the oxide volume grows, and its rate of growth can be related to that of the aluminum as follows

$$\frac{dV_{ox}}{dt} = - n\theta \frac{\rho_{Al}}{\rho_{ox}} \frac{dV_{Al}}{dt} \quad (67)$$

The overall particle radius,  $r_s$ , can be readily computed from the spherical geometry as

$$r_s = [3 (V_{Al} + V_{ox}) / (4\pi)]^{1/3} \quad (68)$$

and the cap height,  $h$ , from the following cubic equation

$$V_{ox} = \frac{4\pi}{3} h^2 (3 r_s - h) \quad (69)$$

### 3.2.7 Solution Approach

To describe the history of the burning aluminum/condensing oxide droplet, Eqns. (66) and (67) are integrated numerically using the IMSL routine DVERK [46]. To evaluate the burning flux  $\dot{m}''_{Al}$  at any instant in time, it is

necessary to solve the nonlinear, coupled system of six equations (Eqns. 45, 46, 49, 50, 61, 62) for the six unknowns:  $\eta$ ,  $\hat{\theta}$ ,  $M_{A1}$ ,  $Y_{A1,s}$ ,  $Y_{v,f}$  and  $\hat{r}_f$ . The Newton-Raphson method was applied to effect a solution to this system, where the partial derivatives of the Jacobian matrix were determined using finite-difference approximations.

## IV. RESULTS AND DISCUSSION

### 4.1 GENERAL OBSERVATIONS

#### 4.1.1 Slurry Droplet Life History

4.1.1.1 CO/O<sub>2</sub>/N<sub>2</sub> Flames (Dry Environments) - A typical sequence of events for a stabilized Al/JP-10 slurry droplet is illustrated in Figs. 10 and 11. The photographs in Fig. 10 were not backlit and thus show radiation from flames and/or the glowing particle. For Fig. 11, strong backlighting was used to silhouette the particle. These figures show that the original slurry droplet swells slightly as the JP-10 burns out (Fig. 10, photographs A-D) with no visible emission from the agglomerate. The transformation from an obviously liquid droplet to a fuzzy agglomerate, as shown in Fig. 11, photograph B, occurs at about 0.2-0.3 second where the JP-10 burnout nears completion. The agglomerate of aluminum particles then heats up, as evidenced by the emitted radiation shown in Fig. 10, photograph E, and the individual particles coalesce, indicated by the sharp decline in particle diameter between approximately 0.50 and 0.55 second.

At the instant when coalescence appears complete, a vapor-phase diffusion flame surrounding the molten particle appears, with the backlit sequence of photographs showing both visible emission from the flame zone and blockage of the backlighting by the oxide smoke, particularly in the cooler wake regions. For the purposes of this study, ignition was defined as the time when coalescence was complete. This event was repeatable, easy to ascertain from the film records, and always coincided with the appearance of a vapor-phase flame.

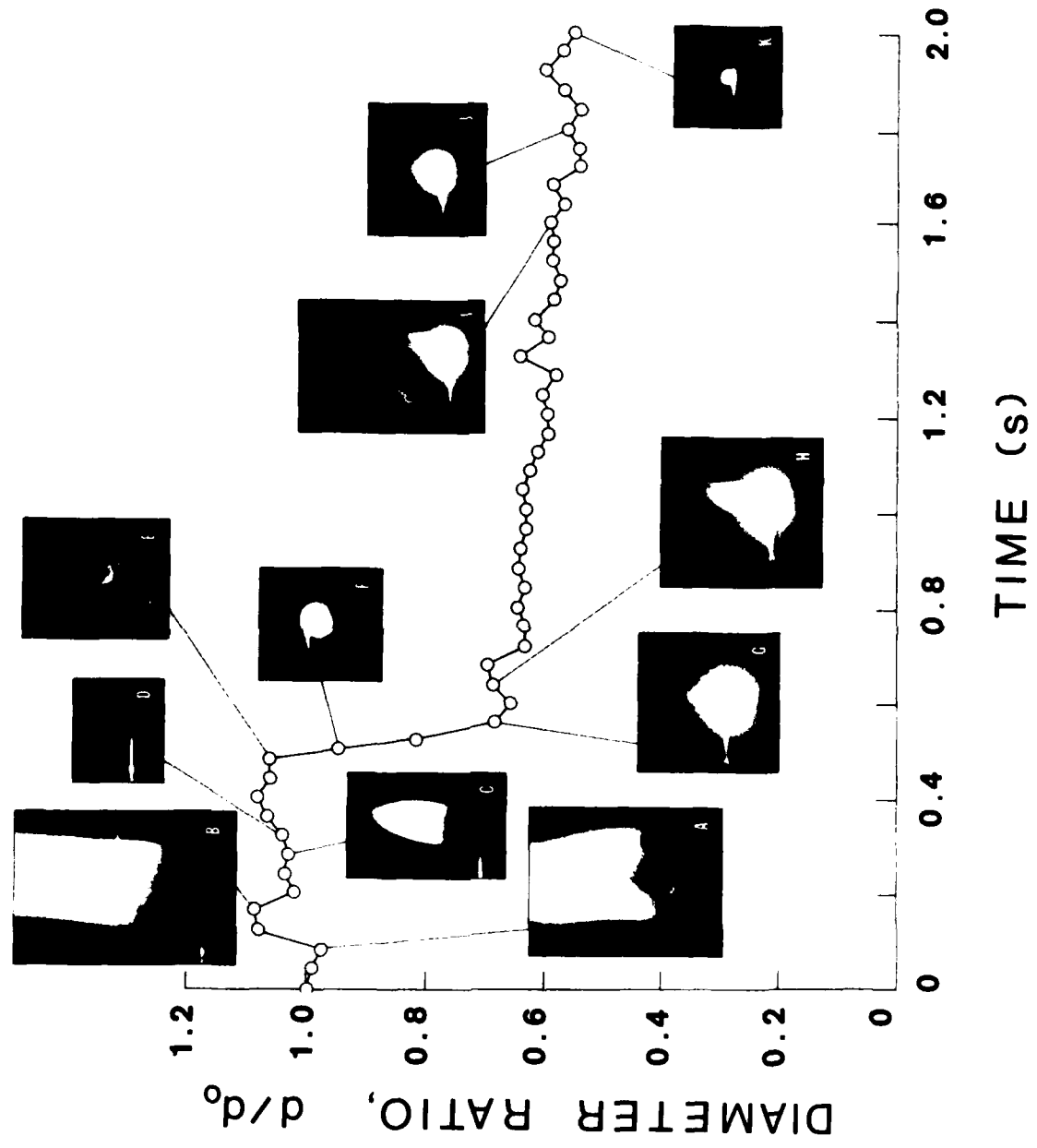


FIGURE 10. Typical aluminum slurry droplet life history--natural light.

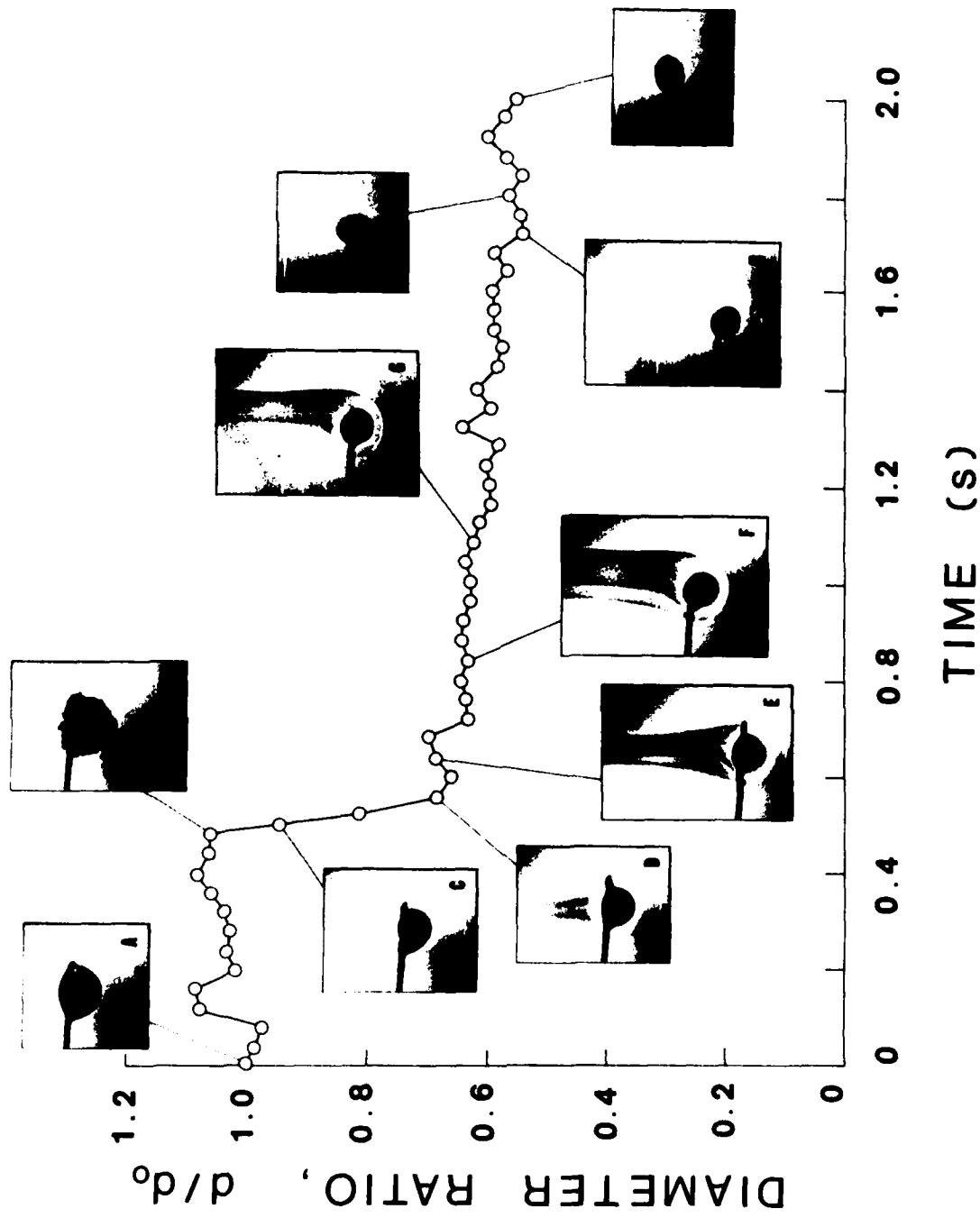


FIGURE 11. Typical aluminum slurry droplet history--backlit.

Interestingly, the backlighting intensity is such that, after ignition, some emission from the burning droplet can be seen. As a result of the difference in emissivity between the molten aluminum and the oxide, the liquid aluminum droplet can be distinguished from the oxide cap which forms on the leeward side of the particle. Shifting of the position of this cap-like structure results in asymmetrical burning as shown in Fig. 11, photographs F and G. Weak jetting from the burning droplets as shown in Fig. 10, photograph I, occurs occasionally. As burning proceeds, the overall particle diameter decreases as the relative size of the oxide cap grows. At about 1.8 seconds (Fig. 11, photograph I), the flame appears to collapse on the particle surface, and no smoke is visible. For a brief while, the particle continues to glow with some shifting of the shape of the particle, after which the particle cools, and no radiation is visible on the film records. For the purposes of this study, the end of combustion was chosen to occur when the oxide smoke was no longer discernible. Determination of this point involved some subjective judgement. Thus, measurements of combustion times, i.e., elapsed time between coalescence and smoke disappearance, result in more uncertainty than do measurements of ignition times.

Experiments were performed where argon was substituted for the nitrogen diluent to determine if this influenced the accumulation of oxide on the burning drop. Work by Prentice [12] and Wilson and Williams [7] showed that in oxygen/diluent atmospheres oxide accumulation was decreased or eliminated by the substitution of argon for nitrogen. However, no discernible differences were observed on the backlit film records for the combustion of stabilized Al/JP-10 slurry droplets in CO/O<sub>2</sub>/Ar and CO/O<sub>2</sub>/N<sub>2</sub> flame environments. This result is probably a consequence of the

relatively complex composition of the ambient gases, i.e., CO, CO<sub>2</sub>, trace H<sub>2</sub>O, etc., since Prentice [13-14] has shown that oxide accumulation is also related to the presence of carbon-containing species. Whether jetting occurred or not in CO/O<sub>2</sub>/Ar environments could not be ascertained since no natural-light photographs were taken for the CO/CO<sub>2</sub>/Ar flame condition.

4.1.1.2 CH<sub>4</sub>/O<sub>2</sub>/N<sub>2</sub> Flame (Wet Environments) The sequence of events for a stabilized Al/JP-10 slurry droplet in the wet environments was largely similar to that in dry environments. However, two major differences were observed: 1) Relatively violent eruptions or partial fragmentation of the particles occurred in wet environments, as shown in the upper half of Fig. 12. Jetting from the particles was stronger, and more frequent, in wet environments than in dry ones (cf. the lower half of Fig. 12 and Fig. 10, photograph I). Fragmentation has been observed by Prentice [13-14] to be characteristic of aluminum particles burning in wet environments. 2) Based on film records, the vapor-phase flame fronts were closer to the burning particles at the early stage after ignition for the wet environments. This may be mainly due to the higher gas velocities in the wet test conditions (cf. Table 2). However, by about half of the combustion time, the molten aluminum seemed to be nearly encapsulated by the oxide, and the smoke was confined to a smaller region where aluminum was exposed. As burning neared completion, the particles vibrated, moving up and down and back and forth on the SiC probes, producing the last vestiges of an oxide smoke. Encapsulation, which has also been observed by Prentice [13-14], may be related to the strong fragmentation in wet environments.

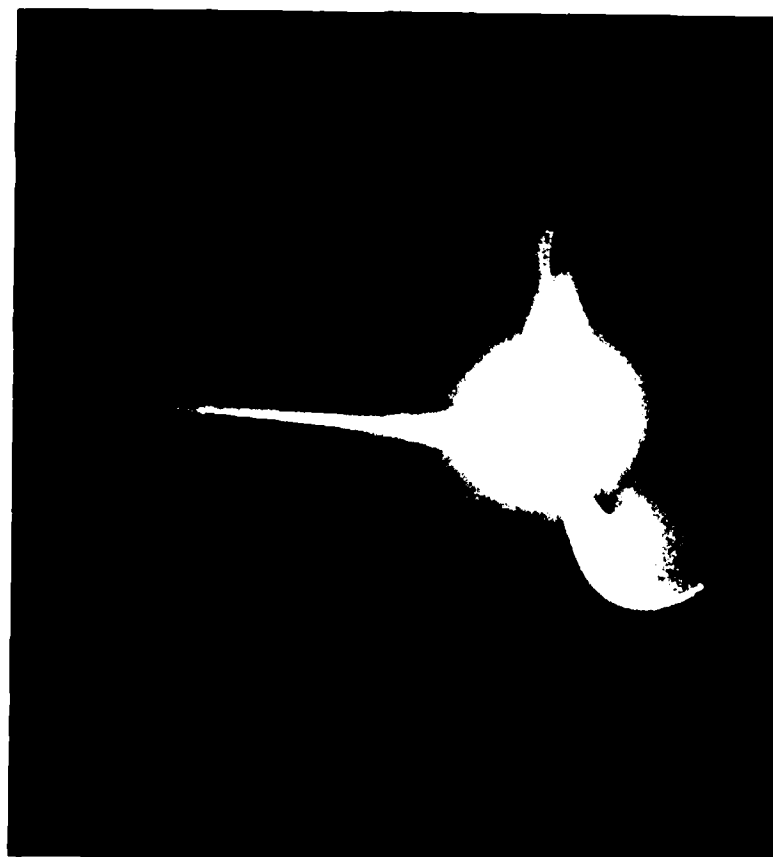


FIGURE 12. Photographs showing characteristics of jetting (lower) and partial fragmentation (upper).

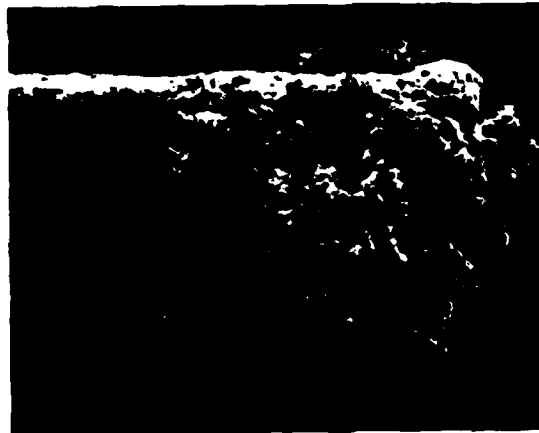
#### 4.1.2 Agglomerate Structure

Each of the three slurries tested produced different agglomerate structures. As shown in Fig. 13, the stabilized Al/JP-10 slurry produced highly porous, loosely compacted agglomerates. Typically the diameter of these agglomerates was the same size or somewhat larger than the diameter of the initial parent slurry droplet. In contrast, the unstabilized Al/JP-10 slurry produced a quite compact, yet still porous, agglomerate with a diameter substantially less than the initial diameter of the slurry droplet from which it was formed. Based on apparent diameters, the porosities of the stabilized slurry and the unstabilized slurry agglomerates were 0.75 and 0.57, respectively. In both cases, the agglomerates formed were quite friable. For the Al/C/JP-10 slurry, spherical hollow agglomerates formed with diameters approximately 10-20% larger than the parent droplets. Differences among the ignition and combustion characteristics of the three slurries will be discussed in the following section.

#### 4.1.3 Ignition and Combustion Characteristics

Figure 14 illustrates representative diameter histories for the three different slurries. Diameter histories of stabilized and unstabilized Al/JP-10 slurry droplets are shown in Fig. 14(a) and 14(b), respectively, with ignition times and burning times indicated. Aluminum/carbon slurry histories are shown in Fig. 14(c) and 14(d). The stabilized Al/JP-10 slurry droplet exhibits nearly constant-diameter behavior as the JP-10 burns out, forming a porous, loosely compacted agglomerate, similar to the one shown in Fig. 13(a). The unstabilized Al/JP-10 slurry droplet, however, shrank as the JP-10 burned, forming a more compact, yet porous, agglomerate similar to the one shown in Fig. 13(b). In both cases, the

# SLURRY AGGLOMERATES



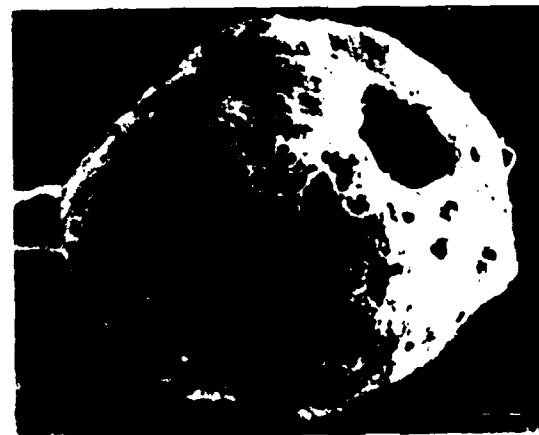
a

STABILIZED  
Al/JP-10



b

UNSTABILIZED  
Al/JP-10



c

STABILIZED  
Al/C/JP-10

FIGURE 13. SEM micrographs of agglomerates formed from three different aluminum-based slurries.

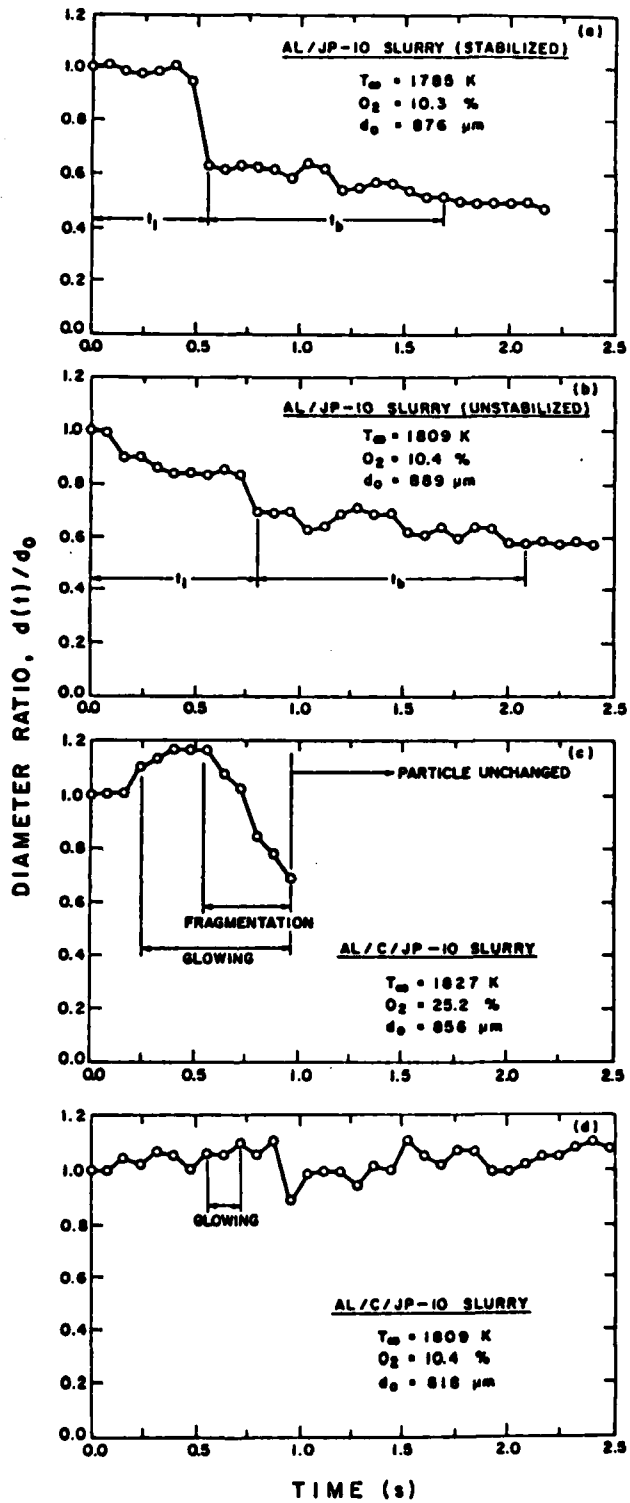


FIGURE 14. Typical diameter-versus-time plots for various aluminum-based slurry types.

individual constituent particles coalesced upon ignition, indicated by the sharp decline in particle diameter. In Fig. 14(d), where the diameter history of a stabilized Al/C/JP-10 slurry droplet in an environment with O<sub>2</sub> level of 10.4% is shown, there is no sharp decline in diameter. A spherical hollow agglomerate, similar to the one shown in Fig. 13(c) was formed. The particle was found to glow brightly during a brief interval as indicated in the figure. This glowing was presumably due to the surface combustion of the individual carbon and/or aluminum particles in the agglomerate. At a higher O<sub>2</sub> level (25.2%), however, violent shattering and fragmentation occurred. As indicated in Fig. 15(c), the shattering occurred shortly after the particle started to glow. Small amounts of fluffy white residue were found on the SiC probes. Representative diameter histories of the three types of slurry in various test conditions are tabulated in Appendix C.

Qualitative differences in the combustion characteristics of the three slurries are shown in Table 5. Other than the detailed appearance of the residual combustion products for the stabilized and unstabilized Al/JP-10 slurries, no major qualitative differences are obvious. However, as will be shown later, longer ignition times were exhibited by the unstabilized slurry. On the other hand, the Al/C/JP-10 slurry behaved quite differently than the Al/JP-10 slurries. For all of the flame conditions with O<sub>2</sub> levels of about 10.4%, no gas-phase flame was observed for the Al/C slurries, while detached flames were obvious for the Al slurries except when gas temperatures approached 1500 K. Another major difference was the shattering and fragmentation of the Al/C slurry agglomerates at the higher O<sub>2</sub> level (25.2%).

Table 5. Comparison of Slurry Characteristics in CO/O<sub>2</sub>/N<sub>2</sub> Flame Environments

Test Conditions T <sub>∞</sub> (K)	O <sub>2</sub> (%)	Stabilized Al/JP-10	Unstabilized Al/JP-10	Stabilized Al/C/JP-10
1827	25.2	Coalescence followed by highly luminous combustion producing dense smoke; white residue	---	Agglomerates fragmented; highly luminous combustion in either of two modes: coalescence and vapor-phase burning or surface oxidation without coalescence
1809	10.4	As above	Coalescence followed by highly luminous combustion producing dense (but somewhat less than stabilized Al slurry) smoke; white and/or gray residue	No coalescence; fairly strong emission; no smoke; gray spherical residue
1659	10.4	As above, but with less luminosity and smoke density; white residues for initial drop sizes greater than ~ 600 μm; gray residue for smaller droplets	Combustion similar to stabilized Al slurry, but with less smoke; dark gray residue	No coalescence; weak emission; no smoke; gray spherical residue
1548	10.3	Coalescence followed by slightly luminous combustion producing smaller quantities of smoke than above; dark gray residue	Similar to stabilized Al slurry	As above
1510	10.0	No ignition for initial droplet diameters less than ~ 500 μm; for larger particles, behavior as above	Similar to stabilized Al slurry	As above

#### 4.1.4 Heat-Up Characteristics

Temperature histories were measured for stabilized Al/JP-10 and Al/C/JP-10 slurry droplets using the methods described in Section II and shown in Fig. 15. The droplets simultaneously were visualized using backlit motion picture photography. Interestingly, plateaus at the boiling point of the JP-10 and the melting point of aluminum did not appear as expected. This was presumably because thermocouple beads were not completely wetted by either the JP-10 or molten aluminum owing to the porous structure formed as JP-10 burned out, and thus were partially heated by the ambient hot gases. Since the Pt/Pt-10% Rh thermocouple wires broke as particle temperatures exceeded the melting point of platinum (2045 K), no temperature data were obtained beyond this point. By comparing the temperature data and film records, it was found that breakage of the thermocouples for Al/JP-10 slurry droplets occurred slightly before coalescence ( $\sim 0.02$  s), while for Al/C/JP-10 droplets, breakage occurred shortly after the agglomerates started to glow. In a low temperature environment, the thermocouple survived the combustion of the Al/C/JP-10 slurry droplet and yielded a complete temperature history, as shown in Fig. 15(c). Again, an abrupt temperature rise was found accompanying the glowing of the particle. As the glowing died out, the particle temperature also gradually decreased to an equilibrium value. In all the above cases, the agglomerates were heated well beyond the ambient temperatures.

The inference to be drawn from the observations discussed above is that chemical reaction played an important role during the heat-up processes of the Al or Al/C agglomerates. This suggests that the experimentally determined ignition times based on complete coalescence are somewhat longer than the time required for thermal runaway, a more usual criterion for

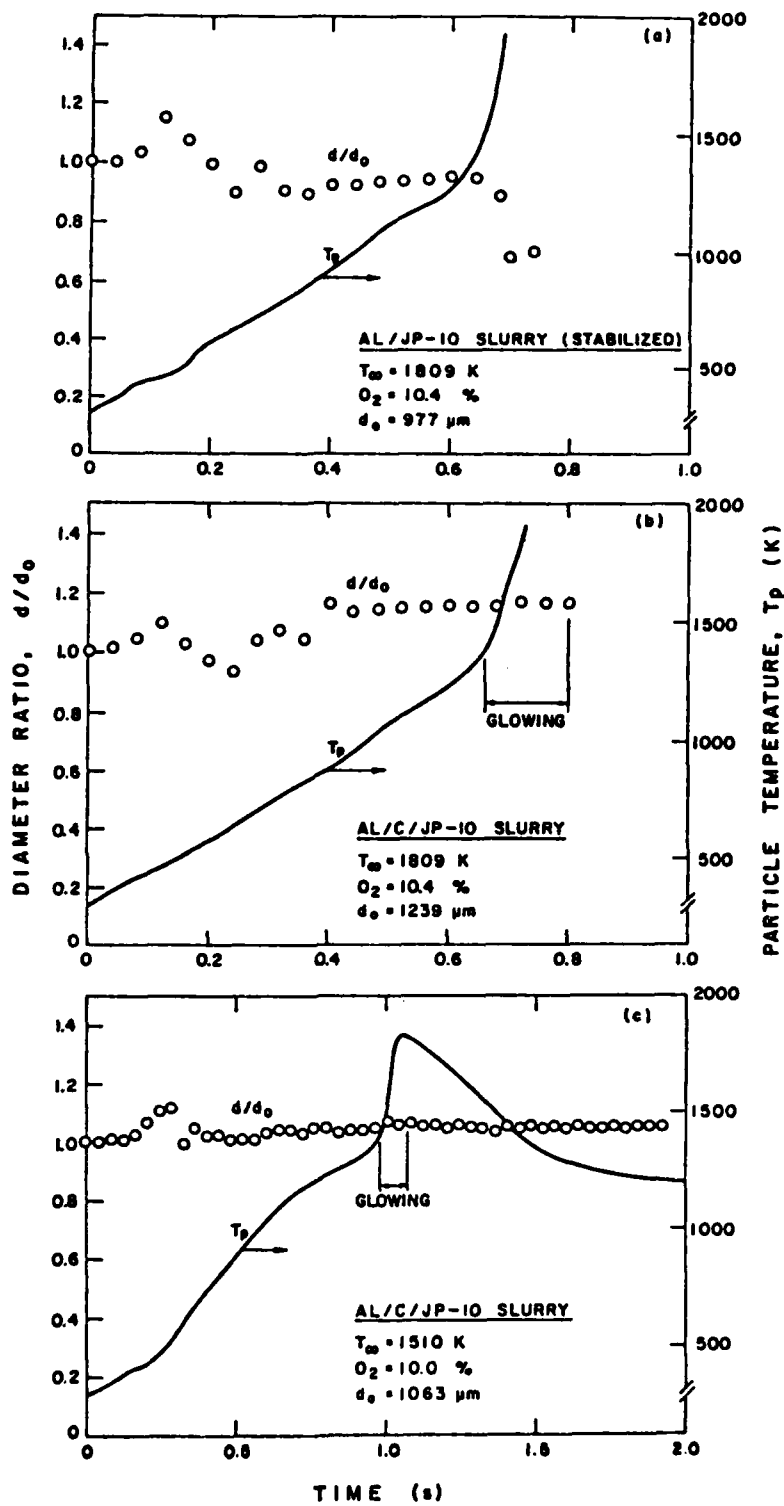


FIGURE 15. Typical temperature-versus-time plots for stabilized Al/JP-10 slurry droplets.

ignition. Examination of Figs. 15(a) and 15(b) shows that rapid increases in agglomerate temperatures, i.e. thermal runaway, occurred at about 1200-1300K. With this criterion for ignition, experimental ignition times would appear to be about 10% less than the time to complete coalescence. Interestingly, the "ignition temperatures" deduced from application of the theoretical model are in good agreement with the experimental thermal runaway temperature of 1200-1300K.

## 4.2 IGNITION

### 4.2.1 Aluminum Slurries

4.2.1.1 Ignition Limits - The minimum ambient gas temperatures required to initiate vapor-phase combustion of the aluminum agglomerates were experimentally determined. The results shown in Fig. 16 as a function of initial diameter were obtained for stabilized Al/JP-10 slurry droplets in dry flame gases with an oxygen level of 10.4%. For the range of droplet sizes investigated, minimum gas temperatures for ignition ranged from about 1300-1500K. These results clearly show that significant reaction of the aluminum is possible without the requirement of heating the particle to the oxide melting point (2300K), as is frequently suggested as a condition for aluminum particle ignition [21,25]. Obviously, the oxide coating on the individual particles is not completely preventing oxygen from reaching the aluminum. The fact that the aluminum agglomerates partially heat-up in a non-oxidizing environment of vaporizing JP-10 may prevent oxide coating growth which would otherwise occur in an oxygen-rich environment. However, agglomerates which were formed at low temperatures (match dried) were also found to ignite in the ca 1850 K burner flames.

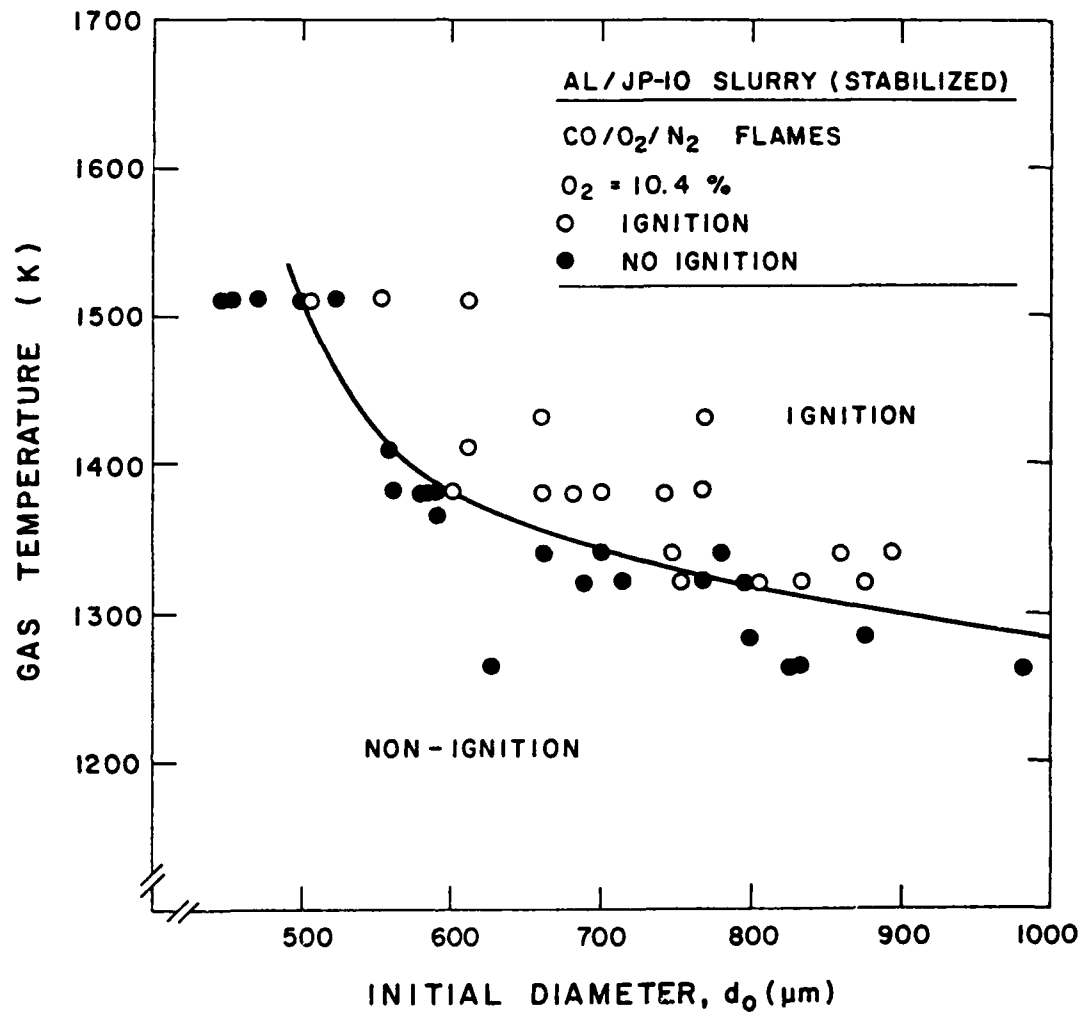


FIGURE 16. Minimum ambient gas temperatures required for ignition versus initial diameter for stabilized Al/JP-10 slurry.

The shape of the ignition limit curve also provides some insight into the mechanism of agglomerate ignition. For example, if agglomerate ignition is achieved essentially instantaneously following a mechanical breakdown of the oxide coating--this breakdown occurring at a fixed temperature--then a balance of heat gained by the agglomerate by convection with the heat lost by radiation would define ignition at the limit condition. With a fixed ignition temperature,  $T_i$ , the minimum ambient gas temperature should increase as the particle diameter increases as follows:

$$T_{\infty} = T_i + \frac{\epsilon \sigma T_i^4}{k \text{Nu}} D \quad (70)$$

In the limiting case of a stagnant environment or a small particle ( $\text{Nu}=2$ ), the minimum ambient temperature would be directly proportional to particle diameter. Allowing for convection would decrease this diameter dependence; however, the trend would still be an increase of  $T_{\infty}$  with diameter. Clearly, the decreasing trend of the data does not support the concept of ignition at a constant temperature.

Another view of ignition would be to assume that the agglomerate is heated by surface reactions with heat removed by convection (and radiation). Assuming a smooth agglomerate, the condition for ignition would be:

$$\frac{k \text{Nu}}{D} (T_i - T_{\infty}) = C \exp (-B/T_i) \quad (71)$$

where the right-hand side of Eqn. (71) represents the chemical heat release per unit surface area. The criterion which determines the ignition

temperature  $T_i$  is that the slopes of the convective loss and heat release with respect to  $T_i$  be equal, i.e.

$$\frac{\partial q''_c}{\partial T_i} = \frac{\partial q''_{chem}}{\partial T_i} \quad (72)$$

or

$$\frac{k \text{ Nu}}{D} = BC T_i^{-2} \exp(-B/T_i) \quad (73)$$

Physically, Eqns. (72) and (73) express that if the particle temperature is perturbed to a value above  $T_i$  thermal runaway will occur. Analysis of Eqns. (71) and (73) reveals that the minimum ambient gas temperature required for ignition decreases with increasing diameter in a manner consistent with the experimental results. The result is also consistent with both the experimental and analytical studies of Polishchuk [28].

4.2.1.2 Diameter Effects - Experimental and theoretically predicted ignition times at a fixed flame condition are shown in Fig. 17 for slurry droplets having initial diameters ranging approximately from 500 to 1100  $\mu\text{m}$ . With the use of both a constant ignition temperature ( $=1250 \text{ K}$ ) and a constant  $\xi$  ( $=2.18$ ), reasonable agreement is shown between theory and experiment over the range of diameters tested. However, the predicted ignition times are somewhat high at the large diameters and conversely somewhat low at small diameters. This discrepancy is consistent with the use of a single value of  $\xi$  for all cases, since one would expect that both the transport enhancement effect and chemical heat release at the surface of aluminum particles would increase as the number of particles in the

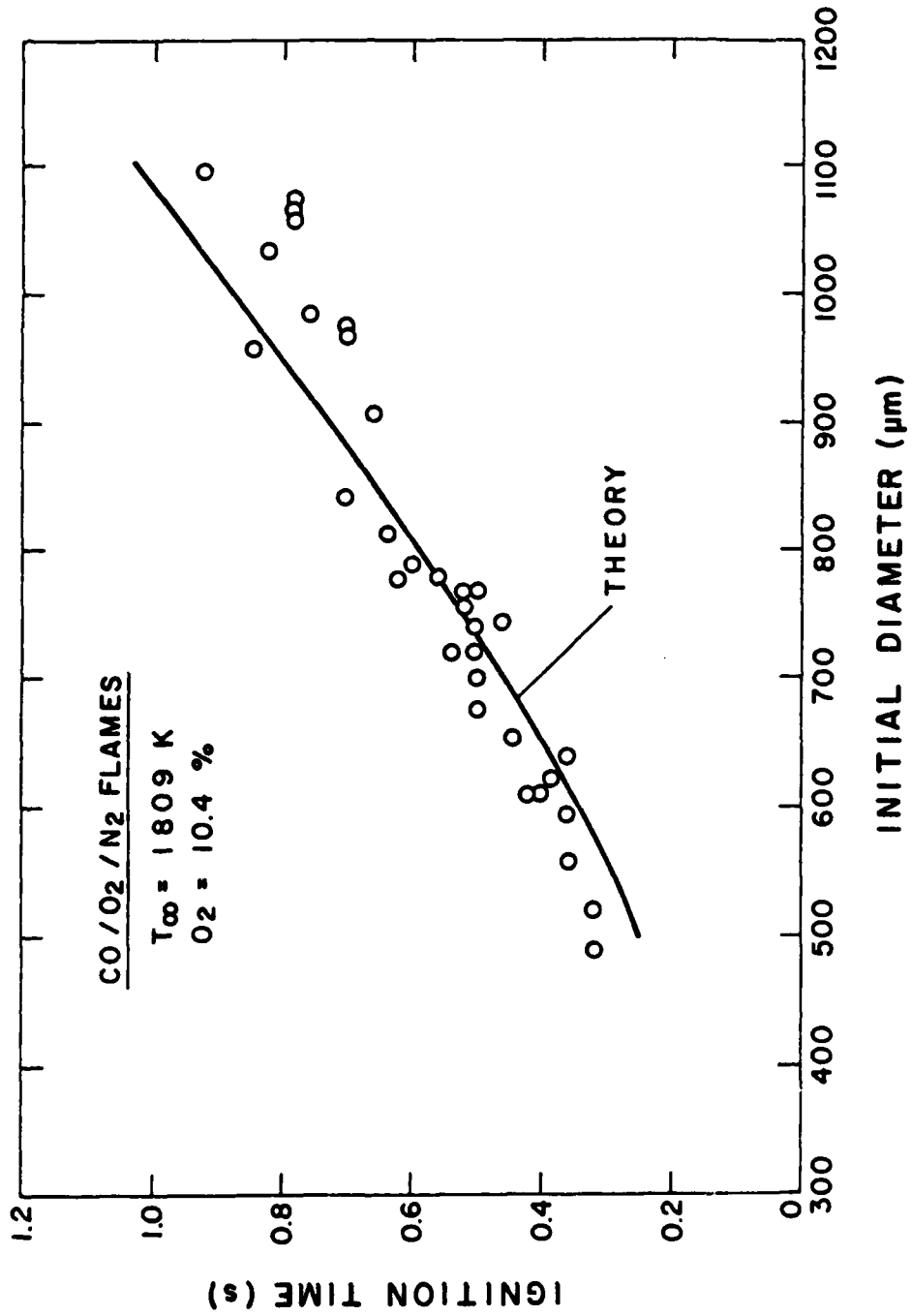


FIGURE 17. Ignition times versus initial droplet diameter for stabilized Al/JP-10 slurry.

agglomerate increases, i.e. as the surface-area-to-volume ratio of the agglomerate increases. Regression of the experimental data in Fig. 17 to a power-law form yielded an exponent of  $1.28 \pm 0.18$ .

4.2.1.3 Temperature Effects - Flame conditions were varied to provide a range of gas temperatures at an essentially constant  $O_2$  level. Results of these experiments are shown in Fig. 18 for wet atmospheres with an average  $O_2$  level of 10.8%. The data points shown were obtained from a best fit of ignition time versus initial diameter at each temperature level. A tabulation of ignition data for each test condition can be found in Appendix B. The cusp in the theoretical curves results from the fact that the flow velocity increased when the gas temperature fell below 1520 K since an extended chimney with a developing flow was used to control temperatures below this point. Agreement between theory and experiment is especially good for the 500  $\mu\text{m}$  droplets, and at the higher temperatures for both diameters. The model, however, predicts the reverse order for the ignition limits of the large and small particles because chemical reaction was neglected and a constant transport enhancement factor was used for all diameters. Similar behavior as shown in Fig. 18 was obtained in dry environments.

4.2.1.4. Slurry Composition Effects - A comparison of ignition times for stabilized and unstabilized aluminum slurries at  $d_0=500$  and 800  $\mu\text{m}$  is presented in Fig. 19. Again the data shown were obtained through interpolation on the ignition-time-versus-diameter plots for each test condition (Appendix B). Except for some low-temperature, unstabilized-slurry cases, ignition time uncertainties are estimated to be 5%. From Fig. 19 it can be seen that at all temperature levels, the unstabilized

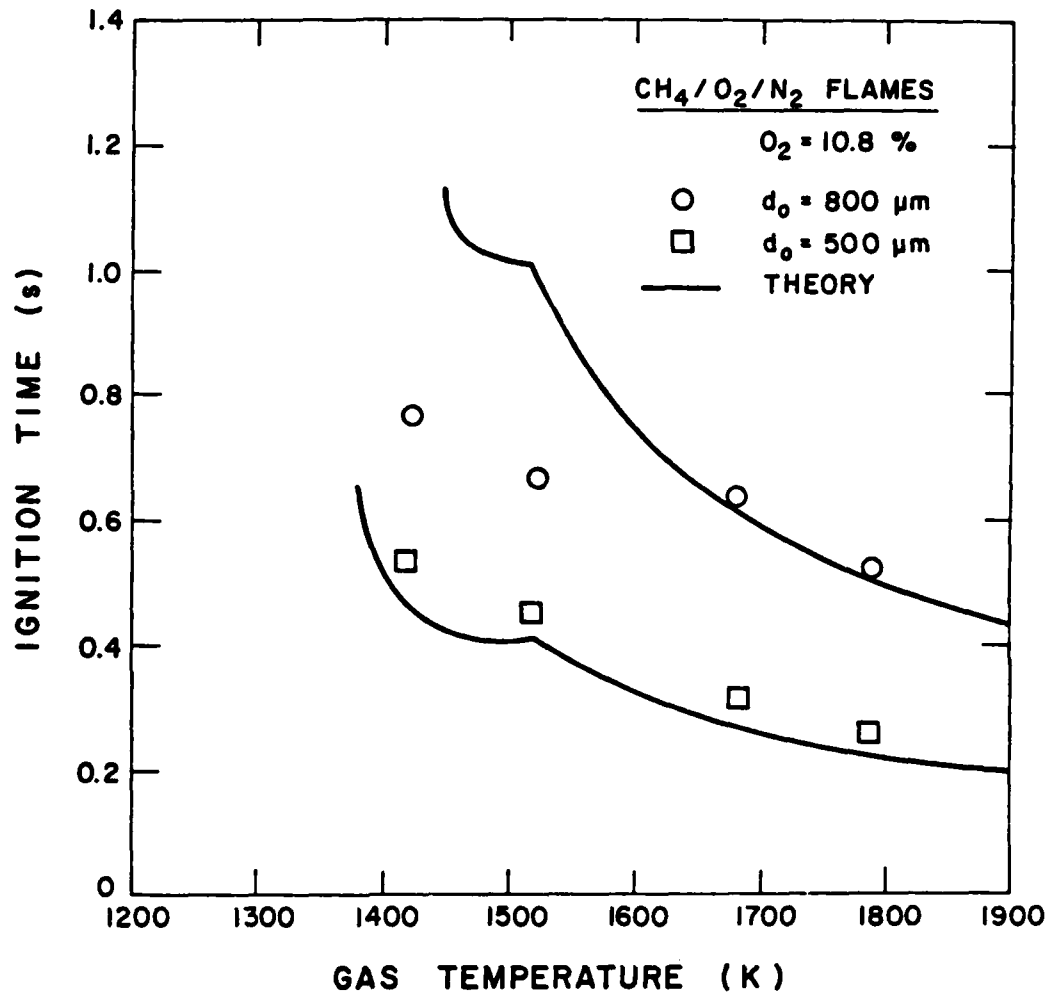


FIGURE 18. Ignition times versus gas temperature for stabilized Al/JP-10 slurries.

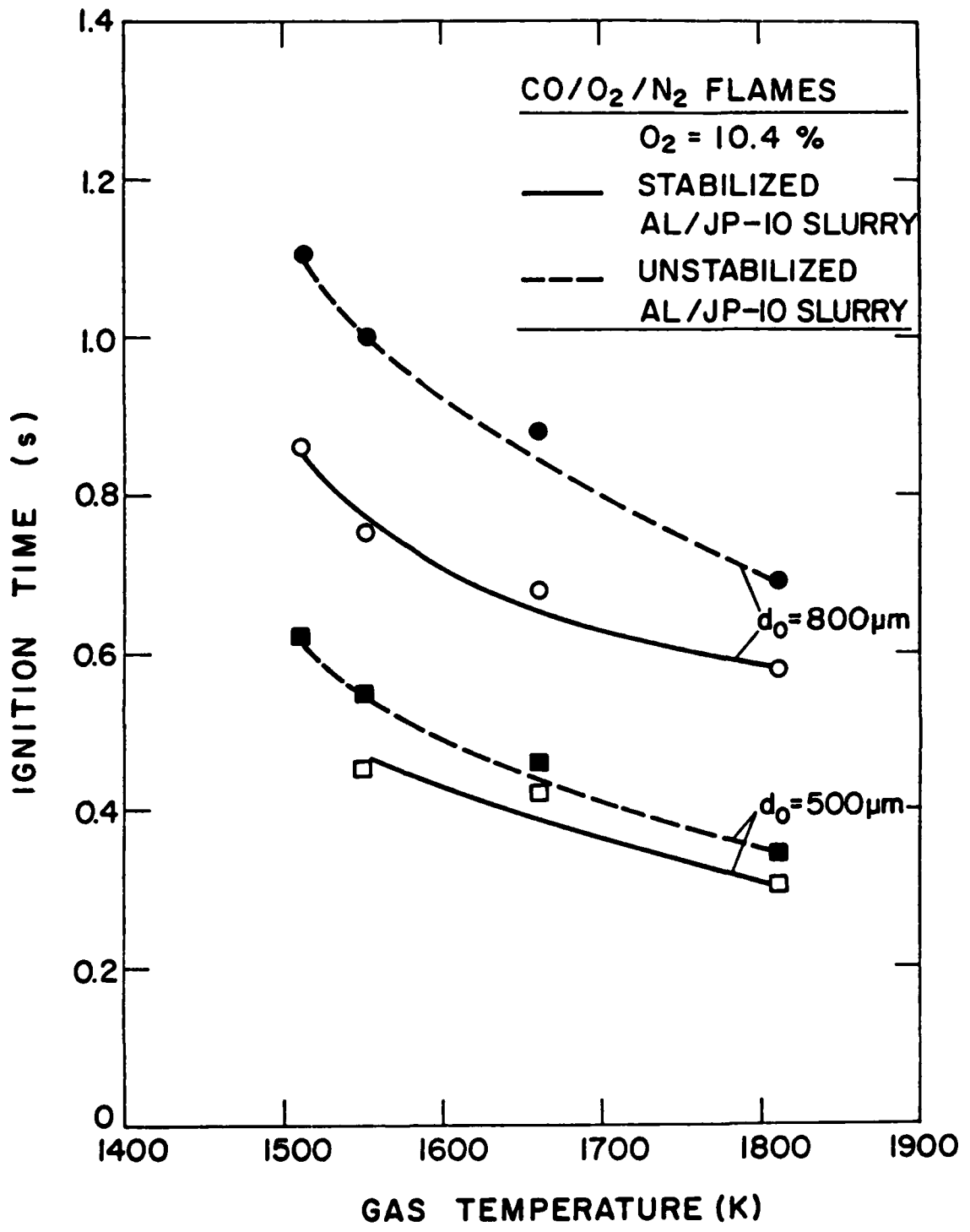


FIGURE 19. Ignition times versus gas temperature for stabilized and unstabilized Al/JP-10 slurries.

slurry ignition times were greater than for the stabilized slurry, with increases ranging from 10 to 30 percent. Three major factors contribute to this result: First, the liquid burnout process is slowed because the size of the droplet shrinks, rather than remaining constant or swelling, as the liquid component evaporates, thus increasing the time until agglomerate heat-up can begin. Second, the compact structure of the unstabilized slurry agglomerate (Fig. 13) has a heat-transfer characteristic more representative of a solid sphere compared to the rough, stabilized-slurry agglomerate. Third, less heat would be liberated by chemical reactions because of the less accessible surfaces structure.

4.2.1.5 Oxygen Mole Fraction Effects - The effect of ambient oxygen mole fraction on ignition times is illustrated in Fig. 20, where experimental data and theoretical predictions are shown for initial diameters of 500, 800 and 900  $\mu\text{m}$ . The predicted influence of  $\text{O}_2$  level is somewhat less than was experimentally observed; however, a 2.5 times increase in  $\text{O}_2$  decreased ignition times at most about 30%. In the theoretical predictions, the principal cause of decreased ignition times with  $\text{O}_2$  level was the more rapid oxidation of the JP-10. The experimental results, therefore, suggest that chemical reaction of the aluminum agglomerate may have some influence on ignition times, with thermal effects dominating.

#### 4.2.2 Aluminum/Carbon Slurries

As was indicated previously in the typical diameter-versus-time plots of Fig. 14, the aluminum/carbon slurry agglomerates did not exhibit coalescence followed by vapor-phase burning. Two representative temperature-versus-time measurements have been shown in Figs. 15(b) and

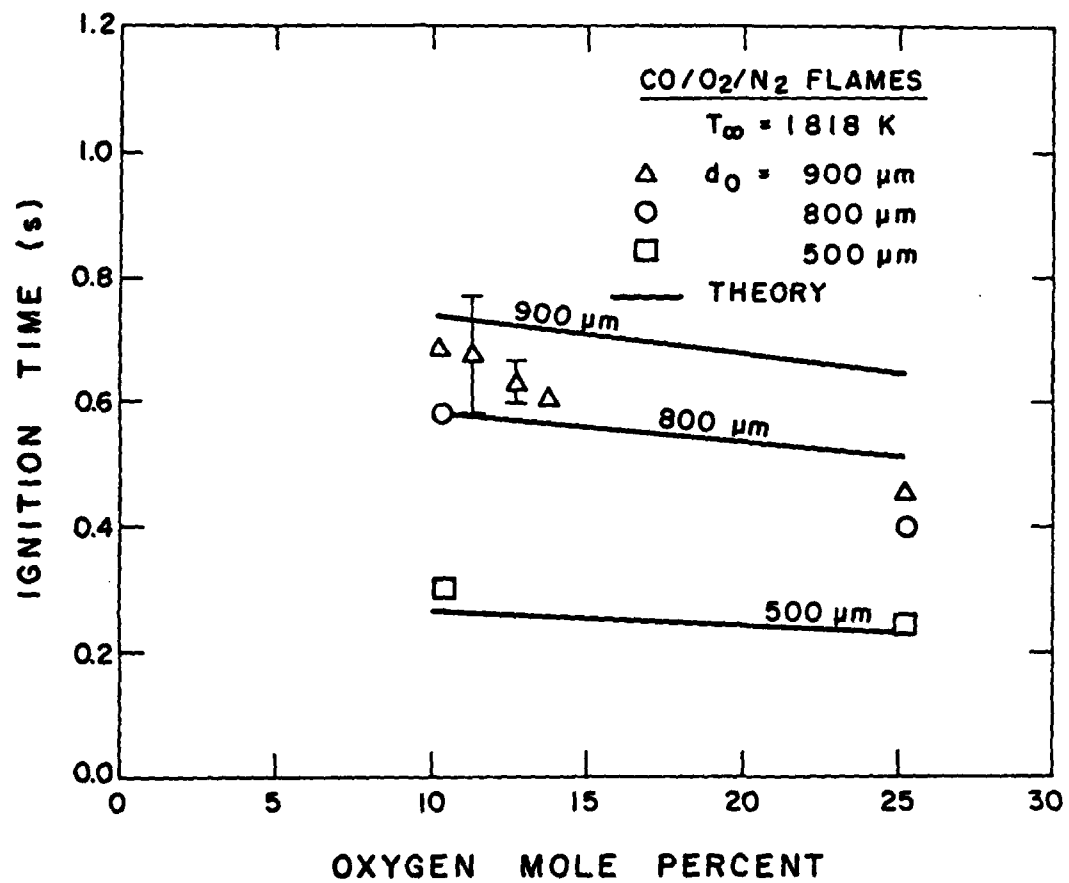


FIGURE 20. Ignition time versus ambient oxygen mole fraction for stabilized Al/JP-10 slurry.

15(c) and discussed in Section 4.1.4. The typical behavior observed for O<sub>2</sub> levels of about 10% was a brief period of particle glowing with no change in particle diameter. At the higher O<sub>2</sub> level (ca 25%), however, strong fragmentation took place after the particle was strongly glowing until the completion of combustion. Two different behaviors, characterized by the absence and existence of the coalescence occurred, leaving small amounts of fluffy white residue on the SiC probes in the first case, and leaving compact crystalline residues in the second case. The latter behavior was most frequently observed when particle diameters were larger than 1000 μm.

#### 4.2.3 Transport Enhancement Determination

In order to determine the size influence on the transport (convection) enhancement factor,  $\xi$ , values of  $\xi$  at  $d_0 = 500, 800$  and  $900 \mu\text{m}$  were calculated for stabilized Al/JP-10 slurry agglomerates at several test conditions. The ignition temperatures used in the calculations were 1300, 1320 and 1510 K for  $d_0 = 500, 800$  and  $900 \mu\text{m}$ , respectively (cf. Fig. 16). Since the determination of  $\xi$  was rather sensitive to the experimental ignition time, a  $\pm 10\%$  uncertainty range of ignition times--which bracketed all experimental data--was also examined for each case. The results are shown in Fig. 21, with only some representative uncertainty ranges of  $\xi$  indicated for clarity. It should be pointed out that the calculations of  $\xi$  were based on experimental ignition (i.e. coalescence) times, which overestimate the time to ignition (thermal runaway) by 10-15% (cf. Section 4.1.4). Thus, the values of  $\xi$  shown in Fig. 21 are somewhat smaller than if the time to thermal runaway were used in their calculation, and the upper limit of the error bars is closer to the actual values.

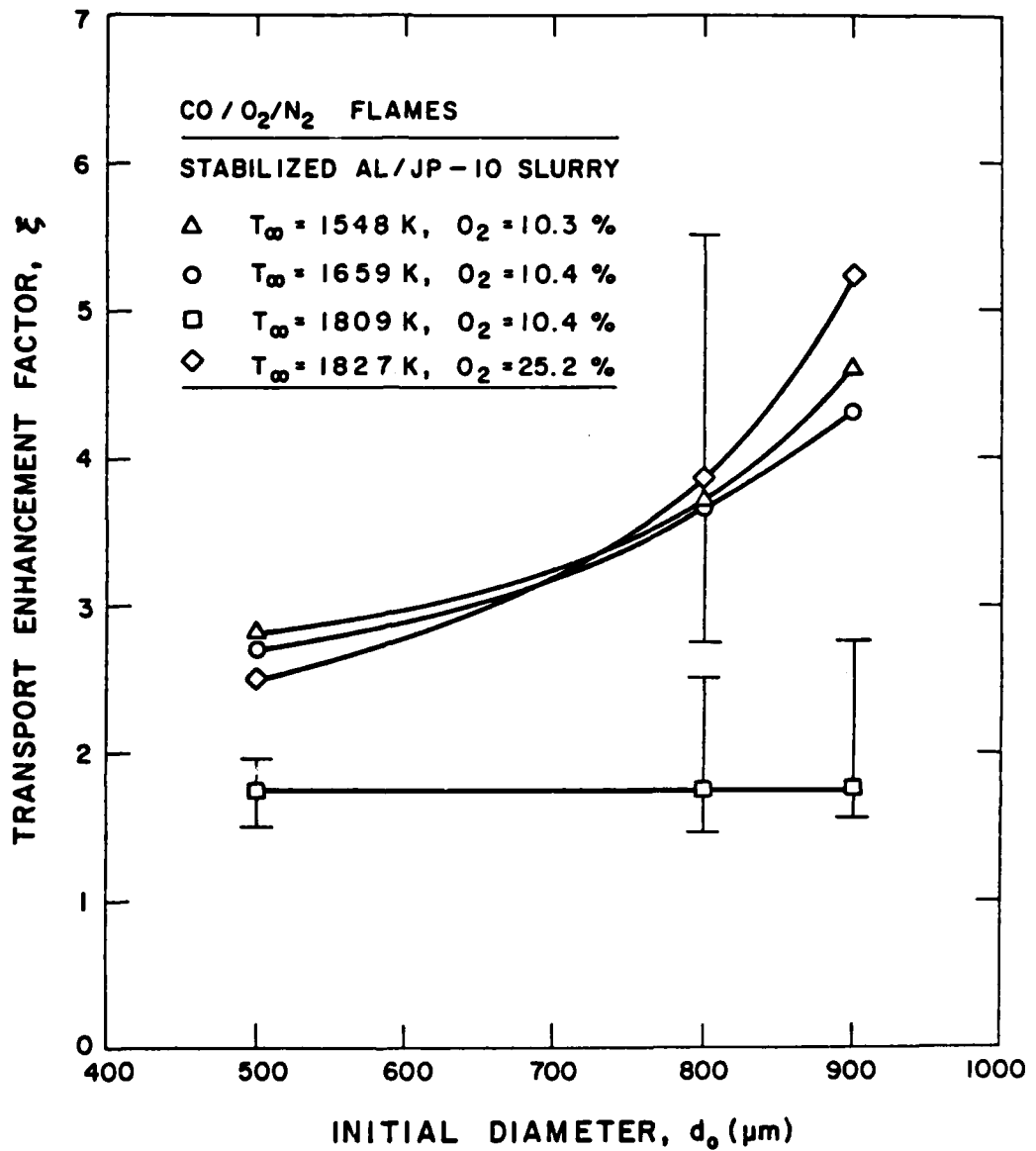


FIGURE 21. Transport enhancement factor versus initial slurry droplet diameter for stabilized Al/JP-10 slurry.

As expected, for a given test condition the transport enhancement factor generally increased with increasing diameter. For the same diameter, however,  $\xi$  was found to change with ambient temperature ( $T_\infty = 1659$  K and  $T_\infty = 1809$  K) and with oxygen mole fraction ( $T_\infty = 1809$  K,  $O_2 = 10.4\%$  and  $T_\infty = 1827$  K,  $O_2 = 25.2\%$ ). This implies that the assumption of negligible chemical reaction effects may be inappropriate because  $\xi$  should otherwise be essentially independent of both environment temperature and oxygen mole fraction. Further experiments are required to separate properly chemical and convective effects.

#### 4.3 COMBUSTION

##### 4.3.1 Aluminum Slurries

4.3.1.1 Typical Theoretical Results - To assist in interpreting the experimental data, the theoretical model was exercised. A typical theoretical result is shown in Fig. 22. The zero time represents the time of ignition, and  $d_m$  is the diameter of the coalesced molten aluminum droplet. As the aluminum mass is depleted, oxide vapor produced in the flame diffuses back to the droplet surface where it condenses and builds the oxide cap which grows with time. When the aluminum is totally consumed, the oxide accumulation represents over 40% of the original mass of the aluminum, assuming a solid nonporous product, and the final particle size is about 65% of the original droplet size. Because of the experimental difficulty in defining the end of combustion and because of the relatively long theoretical time required to consume the last few percent of the aluminum, theoretical combustion times for 95% complete combustion were used to compare with the experimental data.

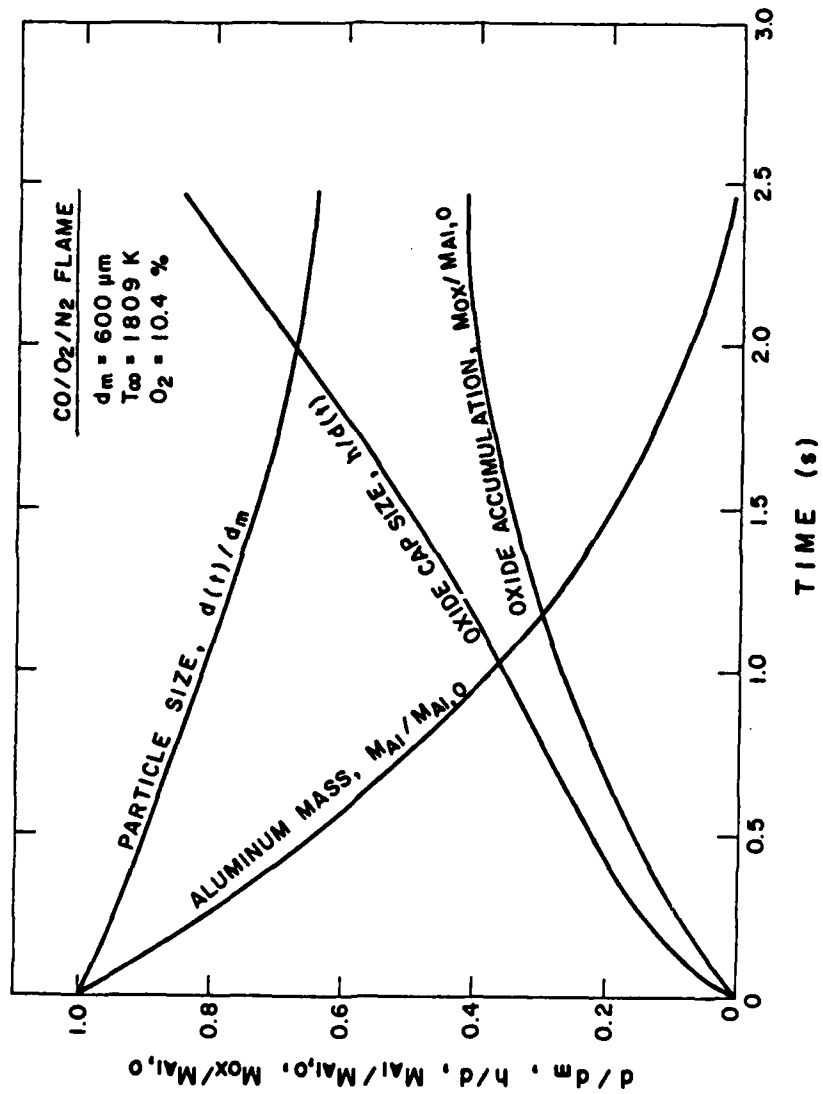


FIGURE 22. Predicted life history of aluminum agglomerate after ignition.

It should be pointed out that in applying the model developed in Section III to the present experimental conditions, radiation effects were deleted. This was done for two reasons: First, the emissivity of the flame zone is at best difficult to determine, and in effect would contribute an additional undesirable adjustable parameter to the model. Second, a parametric study was performed to determine the influence of radiation on the model predictions. This study showed that radiation effects had a minimal effect on burning rates, and hence, burning times; however, it also showed that radiation losses could be sufficiently large to prevent oxide dissociation in the flame and thereby remove the mechanism for the experimentally observed oxide accumulation on the surface of the burning droplet. These results are illustrated in Fig. 23. As the flame emissivity increases beyond  $10^{-3}$ , dissociation falls off rapidly, although the burning rate remains nearly constant. This coupling of radiation and oxide accumulation mechanism suggests an important and exciting area for further research.

4.3.1.2 Initial Diameter Effects - In Fig. 24, experimental and theoretical burning times versus initial molten droplet size are compared. Two theoretical curves are shown which essentially bracket the data: The upper curve ( $F=0$ ) employs the assumption of an impervious oxide cap, while the lower curve ( $F=1$ ) assumes that there are sufficient fissures or fumaroles in the cap to completely wet the cap with vaporizing aluminum. It can be seen that the experimental data lie closer to the totally wet cap limit (i.e.  $F=1$ ). Justification for including some leakage of aluminum through the oxide can be found in the flame structure seen in Fig. 10, photographs E-G, where a strong concentration of smoke is seen directly

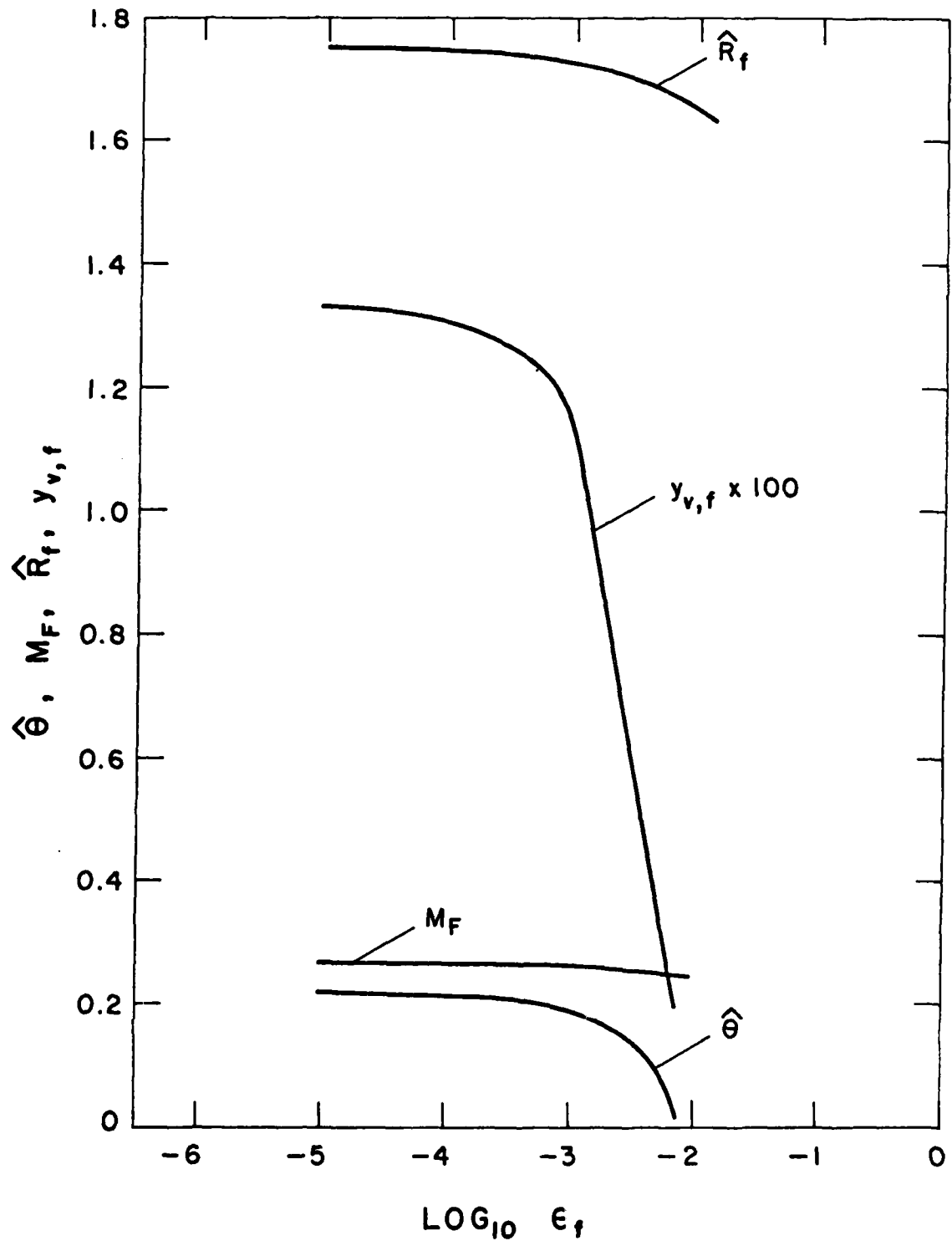


FIGURE 23. Predicted influence of flame emissivity on dimensionless burning rate, flame radius, product vapor mass fraction at the flame, and the fraction of oxidizer dissociated.

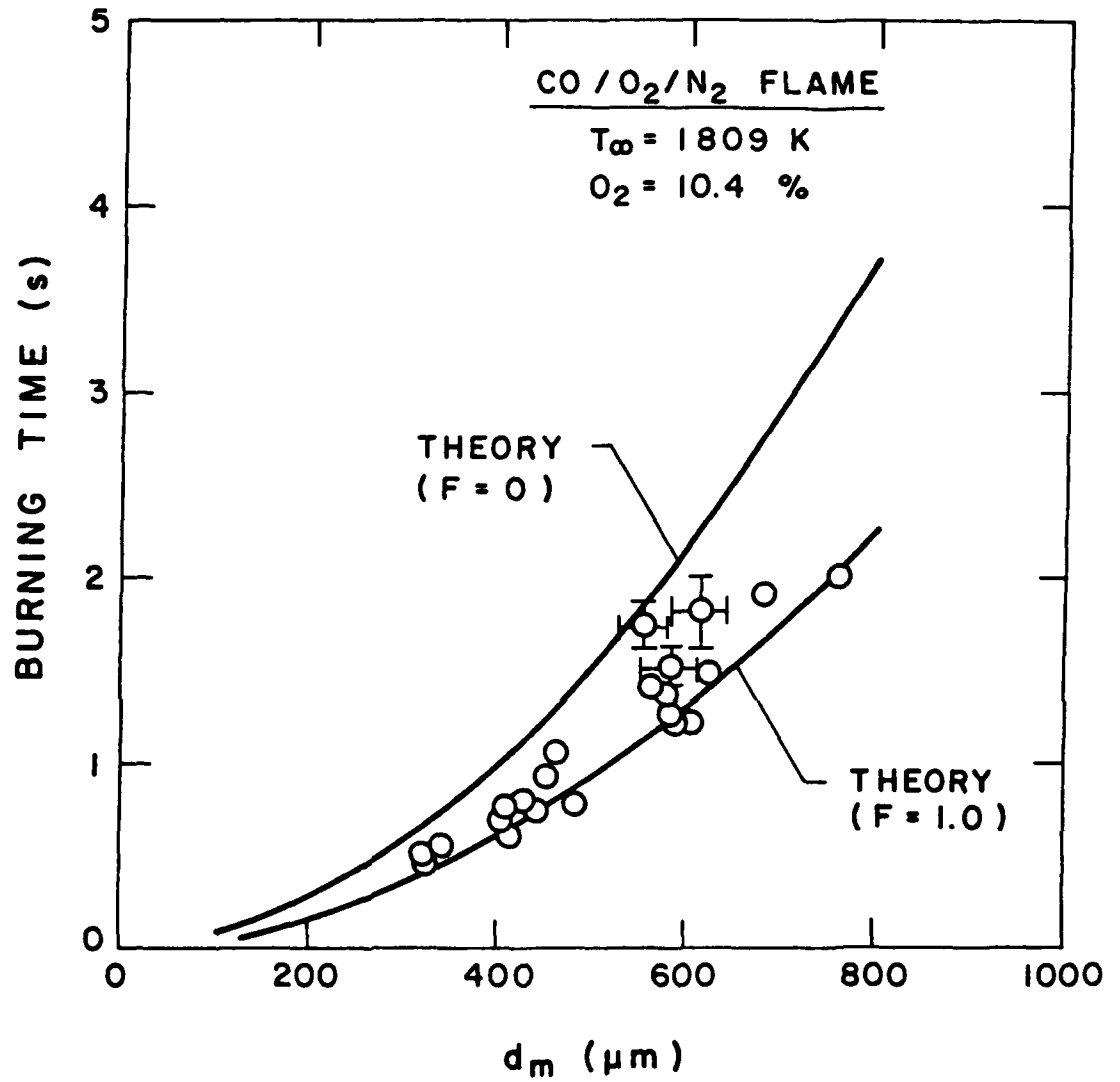
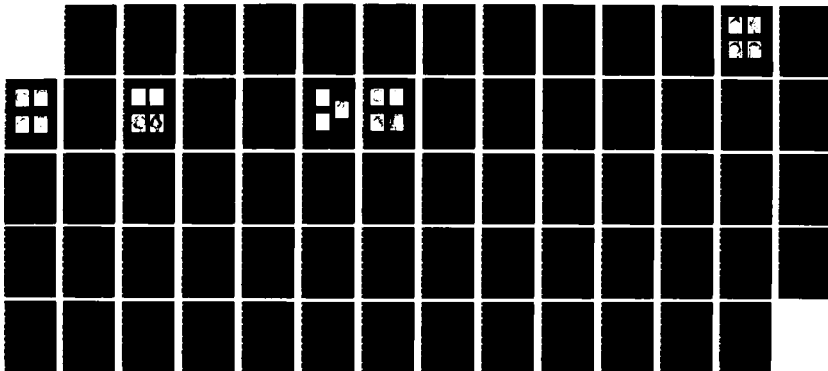
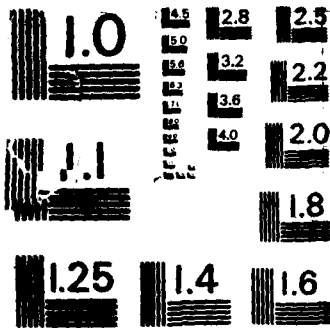


FIGURE 24. Burning times versus diameter of molten droplet following coalescence.

AD-A171 252 IGNITION AND COMBUSTION OF ALUMINUM AND ALUMINUM/CARBON 2/2  
SLURRY AGGLOMERAT (U) PENNSYLVANIA STATE UNIV  
UNIVERSITY PARK DEPT OF MECHANICAL EN

UNCLASSIFIED S C WONG ET AL MAY 86 PSU-ME-85-R-0063 F/G 21/2 NL





MICROCOPY RESOLUTION TEST CHART  
NATIONAL BUREAU OF STANDARDS-1963-A

above the oxide cap. In fact, it appears that separate flames may exist for the completely exposed aluminum surface and for the surface covered by the cap. The facts that the two theoretical limit cases bracket the data and that the trend with respect to diameter is well predicted suggest that the basic physics incorporated into the model is reasonable. Power-law regression of the data in Fig. 24 shows burning time proportional to diameter raised to the  $1.77 \pm 0.20$  power.

In Fig. 25, the burning times of the coalesced molten aluminum droplets measured in the present study are plotted along with the measurements for single aluminum particles by other workers [7, 14]. The consistency between the data shows that the combustion process for aluminum slurries is essentially the same as for single aluminum particles, as would be expected since the constituent particles coalesced into a single molten drop.

4.3.1.3 Oxygen Mole Fraction Effects - The theoretical and experimental results for the influence of oxygen mole fraction are compared in Fig. 26. The data were obtained through interpolation at  $d_m = 400$  and  $600 \mu\text{m}$  on burning-time-versus- $d_m$  plots similar to Fig. 24. It has been pointed out in Section 4.1.1.1 that more uncertainty existed in the measurements of burning times than of ignition times. As shown in Fig. 24, the burning time data exhibit considerable scatter. However, the uncertainty ranges are generally within  $\pm 15\%$  for stabilized Al/JP-10 slurry droplets. It can be seen from Fig. 26 that both absolute and trendwise agreement occur between theory and experiment. The experimental data again are bracketed by the two theoretical curves ( $F=0$  and  $F=1$ ) and lie closer to the totally wet cap limit (i.e.  $F=1$ ). Both theoretical and experimental results show that the  $O_2$  level has a strong effect on burning time.

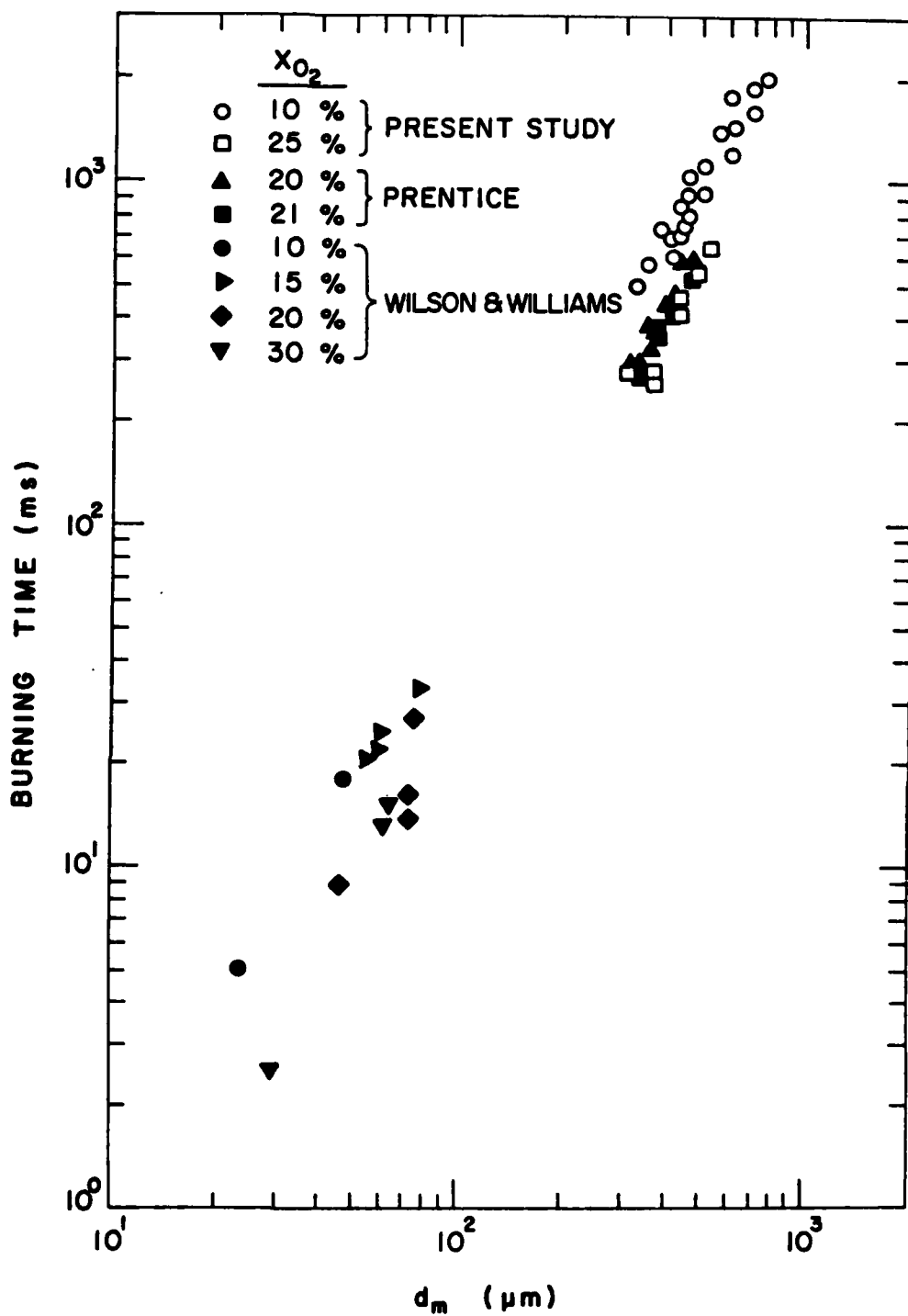


FIGURE 25. Comparison between the burning times of stabilized aluminum slurry droplets and single aluminum particles.

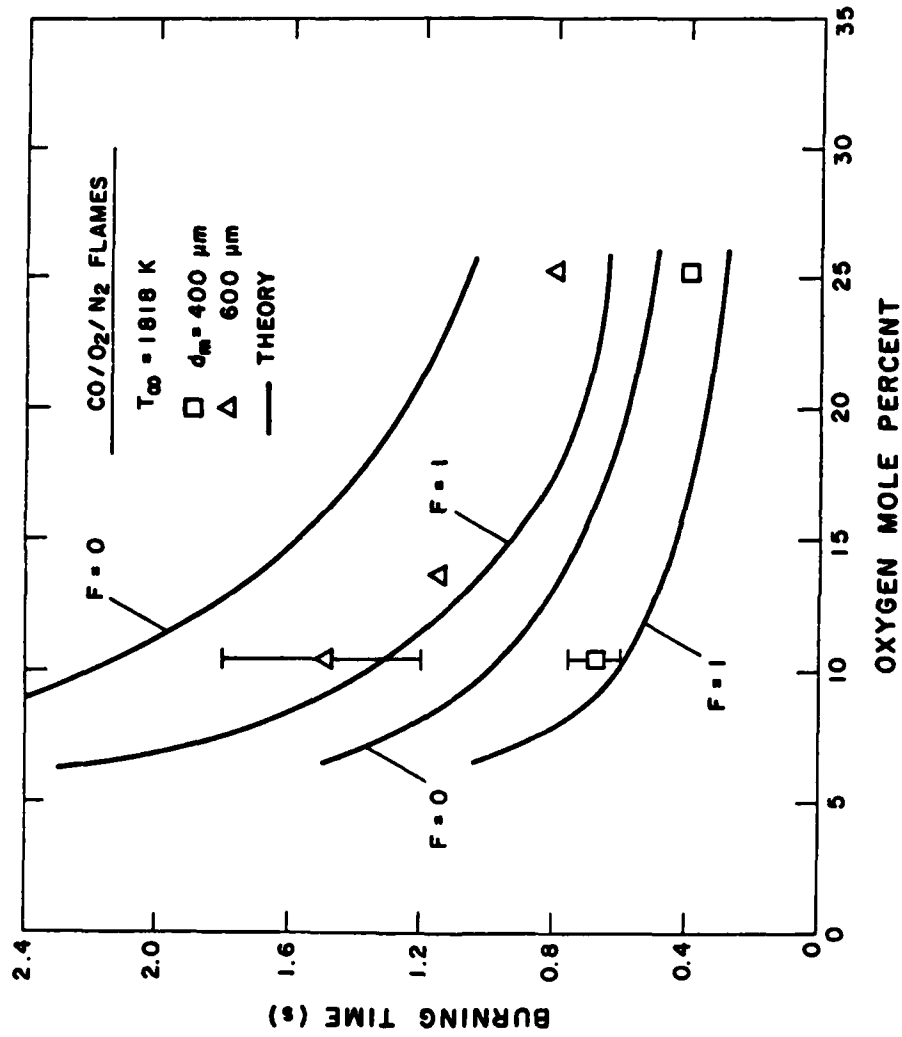


FIGURE 26. Aluminum droplet burning times versus oxygen mole fraction.

4.3.1.4 Ambient Temperature Effects - In Fig. 27, the theoretical and experimental results for the influence of gas temperature are compared for dry and wet environments, respectively. Again, the data were obtained through interpolation. For the dry-environment results, agreement between theory and experiment is very good, and, as in Fig. 24 and 26, the experimental data lie closer to the totally wet cap limit. Good agreement between predictions and experiment can also be found for wet-environment results. However, some complicated phenomena, such as fragmentation, etc., which were not considered in the theoretical model, were observed in wet environments. The effects of the presence of water vapor on the burning of aluminum particles are discussed in the following section.

4.3.1.5 Water Vapor Effects - In the present study, the differences between the theoretical predictions for wet and dry environments arise principally because of different convective velocities and minor property differences. Experimentally, however, the oxide appeared to encapsulate the molten aluminum, apparently causing relatively violent eruptions or partial fragmentation of the particles in wet atmospheres, as previously shown in Fig. 11. Hence, the burning of aluminum particles in wet environments obviously cannot be fully modeled without considering these complicated phenomena. Therefore, the theoretically-predicted burning times for wet environments should be viewed with caution. Nonetheless, qualitative information can be obtained from the results.

Figure 27 shows that the burning times were somewhat shorter in wet than in dry environments, as was observed by Prentice [13,14]. However, the shortening observed in the present study is mainly a result of convective

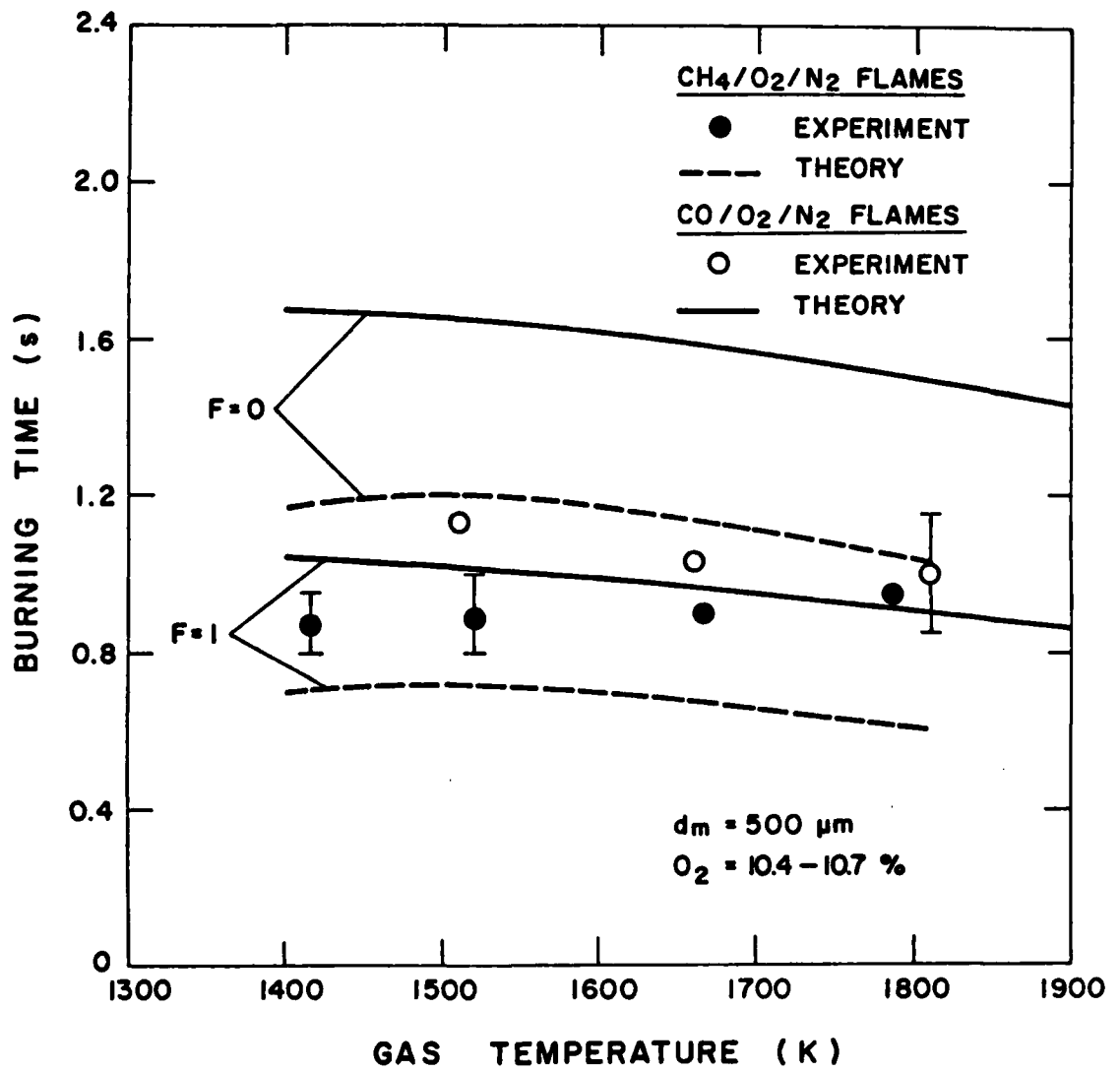


FIGURE 27. Aluminum droplet burning times versus ambient gas temperature.

effects because a similar trend was also obtained by the theoretical model. Intuitively, encapsulation would increase the burning times while fragmentation would decrease them. This suggests that these two phenomena taken together produce no significant net effect.

4.3.1.6 Slurry Composition Effects - The burning times of stabilized and unstabilized Al/JP-10 slurry droplets are compared in Fig. 28. Again data were obtained through interpolation of the burning-time-versus- $d_m$  plots. Data scatter was more serious for unstabilized slurry droplets than for the stabilized slurry (Appendix B) with the uncertainty of burning times reaching  $\pm 20\%$ . With this understanding, it can be seen from Fig. 28 that the burning times were essentially the same for stabilized and unstabilized slurries at high-temperature conditions ( $T_\infty > 1659$  K). Also, except for the apparently slightly less oxide smoke produced for unstabilized slurry droplets, no significant differences were observed on either backlit or natural-light film records at these high-temperature conditions. At the low-temperature condition ( $T_\infty = 1510$  K), however, the ignition times are slightly shorter for unstabilized slurry droplets. At this condition, the backlit film records show that a condensed product at the surface appeared earlier, and for a significant period of time the vapor-phase burning was confined to a limited region around the droplet destroying the symmetry.

4.3.1.7 Comparison of Aluminum and JP-10 Burning Times - A comparison between the burning times of coalesced aluminum agglomerates and those of JP-10 droplets (both with and without the stabilizing additives) is shown in Fig. 29. For corresponding test conditions, the burning times of aluminum droplets are found to be about 4 times those of JP-10 droplets at

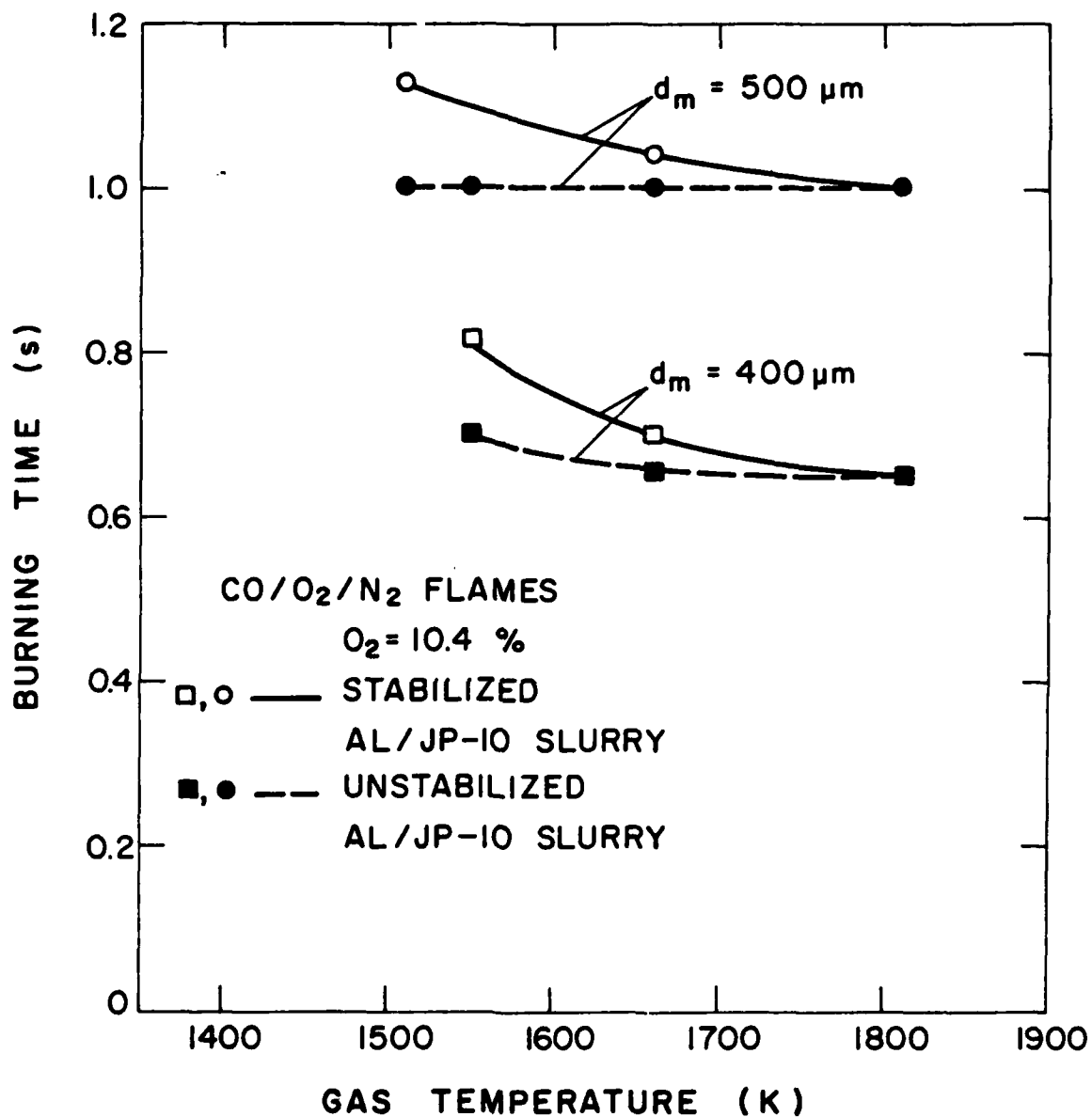


FIGURE 28. Aluminum droplet burning times versus ambient gas temperature for stabilized and unstabilized Al/JP-10 slurries.

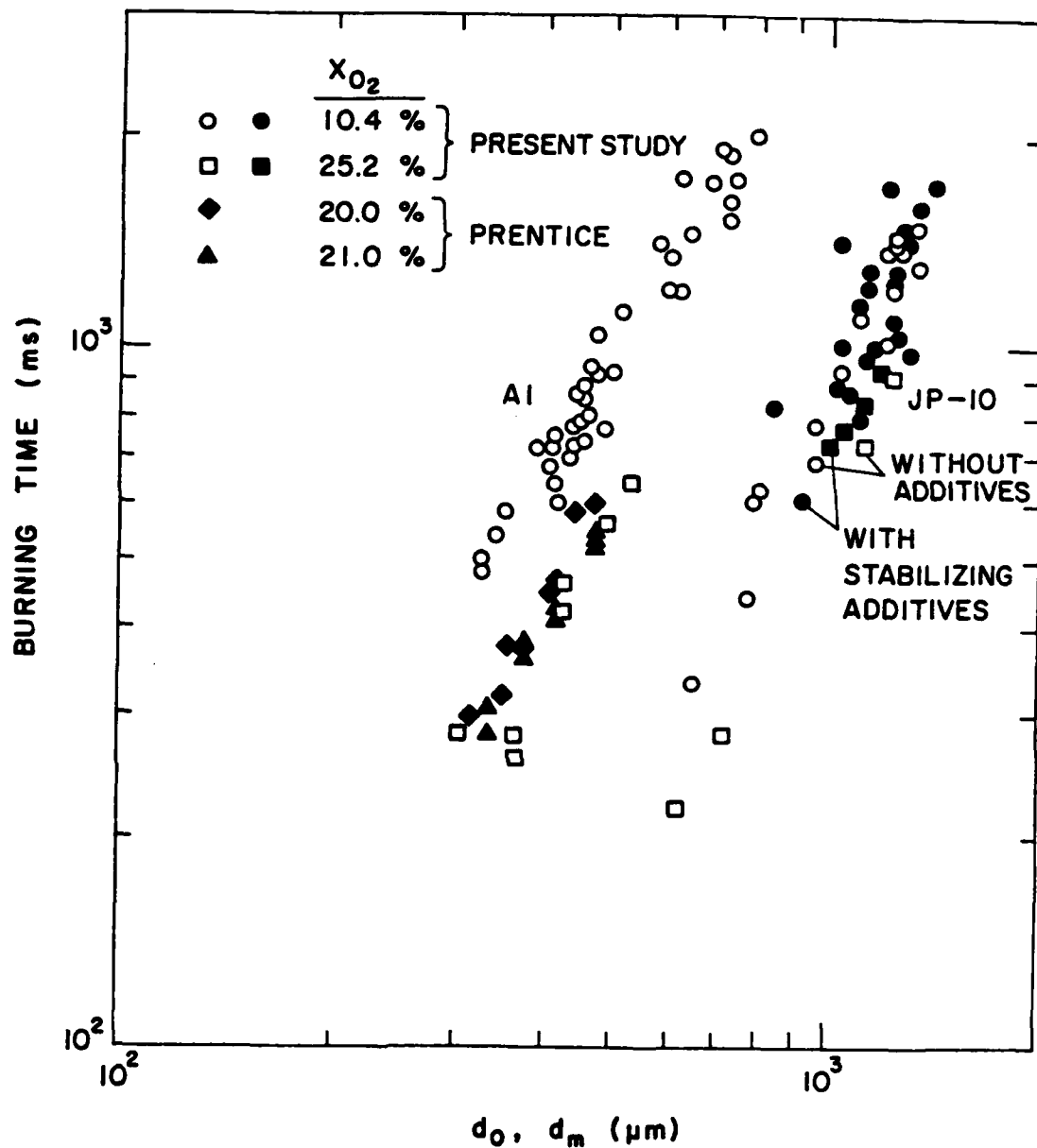


FIGURE 29. Comparison between the burning times of aluminum droplets and JP-10 droplets.

diameters of 600-700 microns. It can also be seen that the burning times of aluminum droplets are little influenced by ambient temperatures, with oxygen effects dominating. The burning times of JP-10 droplets, on the other hand, depend on ambient temperature as well as oxygen level<sup>1</sup>. In our test range, the burning-rate exponent,  $n$ , in the " $d^n$  law" is estimated to be  $n = 1.7 \pm 0.2$  for the burning of aluminum particles, while  $n$  is closer to 2 for the burning of JP-10 droplets. The effect of stabilizing additives on the burning times of JP-10 droplets is not significant except for the high-oxygen test condition ( $T_\infty = 1827$  K,  $O_2 = 25.2\%$ ), where the additives caused increased burning times. This result is consistent with the findings of Polishchuk et al. [52] which showed that evaporation rates of kerosene thickened with polyisobutylene depended upon both the ambient conditions and the concentration of the additive. Moreover, evaporation times were typically increased by the presence of the additive, but in some cases, decreases were observed [52].

#### 4.3.2 Aluminum/Carbon Slurries

Because of the shattering which occurred at high  $O_2$  levels and the physical inability to measure burning times at low  $O_2$  levels, no quantitative results for combustion of the Al/C slurry were obtained. However, residual combustion products were analyzed and are discussed in the next section.

---

<sup>1</sup>The dependence of the burning times of JP-10 droplets on ambient temperature is not clearly shown in Fig. 29 because, for clarity, no distinction is made with respect to ambient temperature. The seemingly scattered data are actually consistent ones corresponding to various test conditions. A clearer idea of the dependence can be obtained from the tables in Appendix D.

#### 4.4 COMBUSTION PRODUCT ANALYSIS

##### 4.4.1 Accumulated Products

4.4.1.1 Aluminum Slurries - Residual combustion products remaining on the particle support probes were investigated with a scanning electron microscope (SEM) and analyzed for composition by X-ray diffraction.

Figure 30 shows SEM micrographs of products obtained for a sequence of tests with the stabilized Al/JP-10 slurry in wet environments at essentially constant oxygen levels. The highest temperature results show a compact mass of  $\alpha$ -Al<sub>2</sub>O<sub>3</sub> crystals with the individual crystals having a characteristic size of about 10-15 microns. As the gas temperature was lowered, the individual crystal sizes increased, reaching about 50-60 microns for  $T_{\infty} = 1417$  K. As shown in Table 6, the composition remained  $\alpha$ -Al<sub>2</sub>O<sub>3</sub>. The last micrograph in the sequence shows an agglomerate which failed to ignite.

For dry environments, the individual crystals were much less apparent with a generally more smooth appearance as can be seen in Fig. 31. The chemical composition, however, was comparable in both wet and dry environments for high-temperature conditions ( $T_{\infty} \geq 1659$  K), as can be seen in Tables 6 and 7. For low-temperature conditions ( $T_{\infty} \leq 1548$  K), however, some unburned aluminum was found in the residual combustion products.

Figure 32 shows SEM micrographs of products obtained for the unstabilized Al/JP-10 slurry in dry environments with essentially constant oxygen levels. Except for the highest temperature result, the samples appear smooth, without any individual crystals. The unstabilized Al/JP-10 slurry products showed the presence of both  $\delta$ -Al<sub>2</sub>O<sub>3</sub> and Al along with  $\alpha$ -Al<sub>2</sub>O<sub>3</sub> (see Table 7). Thus it appears that the influence of the stabilizing additives extends all

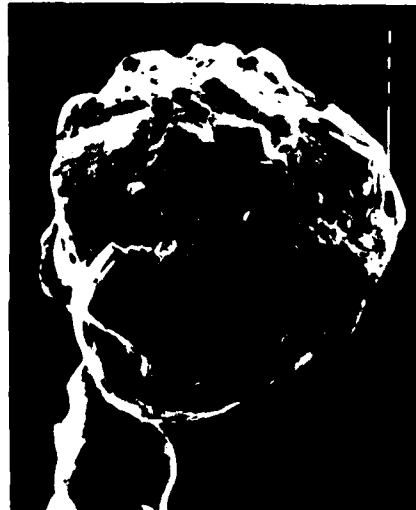
STABILIZED Al/JP-10 SLURRY - WET FLAMES



$T_{\infty} = 1785 \text{ K}$   $O_2 = 10.3 \%$



$T_{\infty} = 1519 \text{ K}$   $O_2 = 10.9 \%$



$T_{\infty} = 1417 \text{ K}$   $O_2 = 10.9 \%$



$T_{\infty} = 1250 \text{ K}$   $O_2 = 10.9 \%$

FIGURE 30. SEM micrographs of residual combustion products for stabilized Al/JP-10 slurry in wet flames.

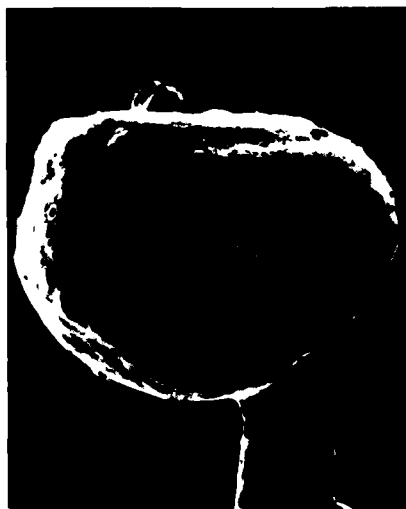
TABLE 6. Residual Combustion Product Analysis--CH<sub>4</sub>/O<sub>2</sub>/N<sub>2</sub> Flame Environments

T (K)	Test Condition		Stabilized Al/JP-10	Stabilized Al/C/JP-10
	O <sub>2</sub> (%)	H <sub>2</sub> O (%)		
1785	10.3	16.2	α-Al <sub>2</sub> O <sub>3</sub>	α-Al <sub>2</sub> O <sub>3</sub>
1519	10.9	12.4	α-Al <sub>2</sub> O <sub>3</sub>	- 50% α-Al <sub>2</sub> O <sub>3</sub>
				- 25% δ-Al <sub>2</sub> O <sub>3</sub>
				- 35% Al <sub>4</sub> C <sub>3</sub>
1417	10.9	12.4	α-Al <sub>2</sub> O <sub>3</sub>	- 50% α-Al <sub>2</sub> O <sub>3</sub> - 50% Al <sub>4</sub> C <sub>3</sub> Trace δ-Al <sub>2</sub> O <sub>3</sub>
1381	10.9	12.4	α-Al <sub>2</sub> O <sub>3</sub> Trace δ-Al <sub>2</sub> O <sub>3</sub>	---
1250	10.9	12.4	Al	---

STABILIZED Al/JP-10 SLURRY-DRY FLAMES



$T_{\infty} = 1827 \text{ K}$   $O_2 = 25.2 \%$



$T_{\infty} = 1548 \text{ K}$   $O_2 = 10.3 \%$



$T_{\infty} = 1510 \text{ K}$   $O_2 = 10.0 \%$



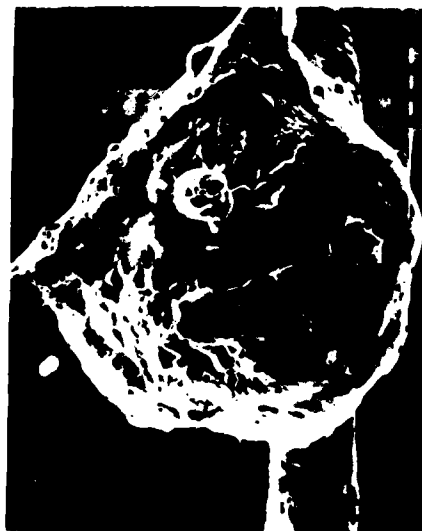
$T_{\infty} = 1510 \text{ K}$   $O_2 = 10.0 \%$

FIGURE 31. SEM micrographs of residual combustion products for stabilized Al/JP-10 slurry in dry flames.

TABLE 7. Residual Combustion Product Analysis--CO/O<sub>2</sub>/N<sub>2</sub> Flame Environments

Test Conditions T (K)	O <sub>2</sub> (%)	Stabilized Al/JP-10	Unstabilized Al/JP-10	Stabilized Al/C/JP-10
1827	25.2	α-Al <sub>2</sub> O <sub>3</sub>	---	α-Al <sub>2</sub> O <sub>3</sub> Trace δ-Al <sub>2</sub> O <sub>3</sub>
1809	10.4	α-Al <sub>2</sub> O <sub>3</sub>	Mostly α-Al <sub>2</sub> O <sub>3</sub> Small amount δ-Al <sub>2</sub> O <sub>3</sub> Trace Al	~50% α-Al <sub>2</sub> O <sub>3</sub> ~15% δ-Al <sub>2</sub> O <sub>3</sub> ~35% Al <sub>4</sub> C <sub>3</sub>
1659	10.4	α-Al <sub>2</sub> O <sub>3</sub>	α-Al <sub>2</sub> O <sub>3</sub> Trace Al	---
1548	10.3	~75% coarse-grained ~25% fine-grained Al	α-Al <sub>2</sub> O <sub>3</sub> Trace Al	---
1510	10.0	Unignited sample- highly oriented Al small amount α-Al <sub>2</sub> O <sub>3</sub>  Ignited sample- not available	67% α-Al <sub>2</sub> O <sub>3</sub> 33% δ-Al <sub>2</sub> O <sub>3</sub>	---

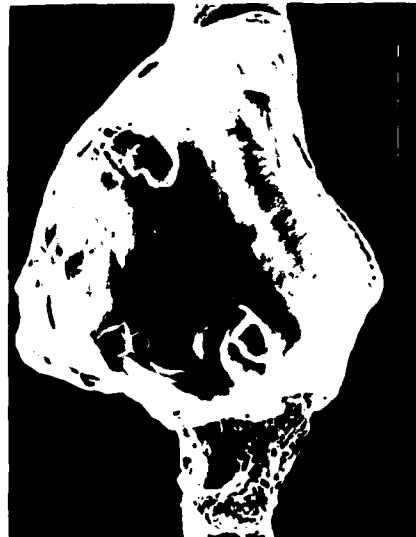
UNSTABILIZED Al/JP-10 SLURRY - DRY FLAMES



$T_{\infty} = 1809 \text{ K}$   $O_2 = 10.4 \%$



$T_{\infty} = 1659 \text{ K}$   $O_2 = 10.4 \%$



$T_{\infty} = 1548 \text{ K}$   $O_2 = 10.3 \%$



$T_{\infty} = 1510 \text{ K}$   $O_2 = 10.0 \%$

FIGURE 32. SEM micrographs of residual combustion products for unstabilized Al/JP-10 slurry in dry flames.

the way to the final combustion products for low-temperature conditions. For high-temperature conditions, however, only ignition times appear to be affected.

4.4.1.2 Aluminum/Carbon Slurries - An interesting finding for the aluminum/carbon slurry was the presence of aluminum carbide ( $\text{Al}_4\text{C}_3$ ) in the product residue (Tables 6 and 7). Thus it appears that heterogeneous reactions occurred for the Al/C agglomerates, producing both  $\text{Al}_2\text{O}_3$  and  $\text{Al}_4\text{C}_3$ . Results for the tests where Al/C slurry droplets were burned at a low-temperature condition ( $T_\infty = 1519 \text{ K}$ ,  $\text{O}_2 = 10.9\%$ ) and subsequently exposed to a high-temperature condition ( $T_\infty = 1785 \text{ K}$ ,  $\text{O}_2 = 10.3\%$ ) showed slow conversion of the  $\text{Al}_4\text{C}_3$  at both conditions as illustrated in Table 8. The equilibrium mole fraction of  $\text{Al}_4\text{C}_3$  at both conditions, estimated using CEC76 [42], were less than  $5 \cdot 10^{-6}$ . Consequently, it appears once  $\text{Al}_4\text{C}_3$  is formed it is difficult to produce the final oxidation product,  $\text{Al}_2\text{O}_3$ , within a short time at  $\text{O}_2$  levels of about 10%. Diffusional resistance of the oxidant through the agglomerate matrix probably contributes to the kinetic limitation.

At high  $\text{O}_2$  levels, however,  $\alpha\text{-Al}_2\text{O}_3$  was the predominant species present. Moreover, it was only at this high  $\text{O}_2$  test condition that coalescence was observed for Al/C agglomerates. As ambient temperatures were decreased, a greater proportion of  $\text{Al}_4\text{C}_3$  was found. Vapor-phase combustion was not obvious at any of the test conditions. SEM micrographs of the Al/C slurry products formed in dry and wet environments are shown in Fig. 33 and 34, respectively. It can be seen from Fig. 33 that two possible types of residual products were found to occur at the 25.2%  $\text{O}_2$  condition: a fluffy, hollow sphere with holes through the wall, and a compact crystalline

TABLE 8. Conversion of  $\text{Al}_4\text{C}_3$  to  $\text{Al}_2\text{O}_3$  at  $T_{\infty} = 1785 \text{ K}$ ,  $\text{O}_2 = 10.3\%$

Time Exposed to High-Temperature (seconds)	$\alpha$ - and $\delta$ - $\text{Al}_2\text{O}_3$	$\text{Al}_4\text{C}_3$
0	50%	50%
15	50%	50%
30	75%	25%
60	80%	20%

STABILIZED AI/C/JP-10 SLURRY - DRY FLAMES



$T_{\infty} = 1827\text{K}$   $O_2 = 25.2\%$



$T_{\infty} = 1827\text{K}$   $O_2 = 25.2\%$



$T_{\infty} = 1809\text{K}$   $O_2 = 10.4\%$

FIGURE 33. SEM micrographs of residual combustion products for stabilized AI/C/JP-10 slurry in dry flames.

STABILIZED Al/C/JP-10 SLURRY - WET FLAMES



$T_{\infty} = 1785\text{K}$   $O_2 = 10.3\%$



$T_{\infty} = 1677\text{K}$   $O_2 = 10.9\%$



$T_{\infty} = 1519\text{K}$   $O_2 = 10.9\%$



$T_{\infty} = 1417\text{K}$   $O_2 = 10.9\%$

FIGURE 34. SEM micrographs of residual combustion products for stabilized Al/C/JP-10 slurry in wet flames.

structure, similar to those produced with the Al slurries. Both types of products were essentially all  $\alpha$ -Al<sub>2</sub>O<sub>3</sub>.

#### 4.4.2 Dispersed Products

Smoke samples were collected on quartz slides for the stabilized Al/JP-10 slurry at the  $T_{\infty} = 1809$  K,  $O_2 = 10.4\%$  test condition. SEM analysis showed most particles were roughly spherical. A smoke-particle size distribution determined for a 200 particle sample is shown in Fig. 35. It can be seen that the number of particles decreases continuously above the 0.1  $\mu$ m size. Because of the limited resolution of the SEM, particle sizes less than approximately 0.1  $\mu$ m could not be clearly resolved. Thus, it is quite possible that Fig. 35 shows the tail of a distribution curve with the modal diameter smaller than 0.1  $\mu$ m.

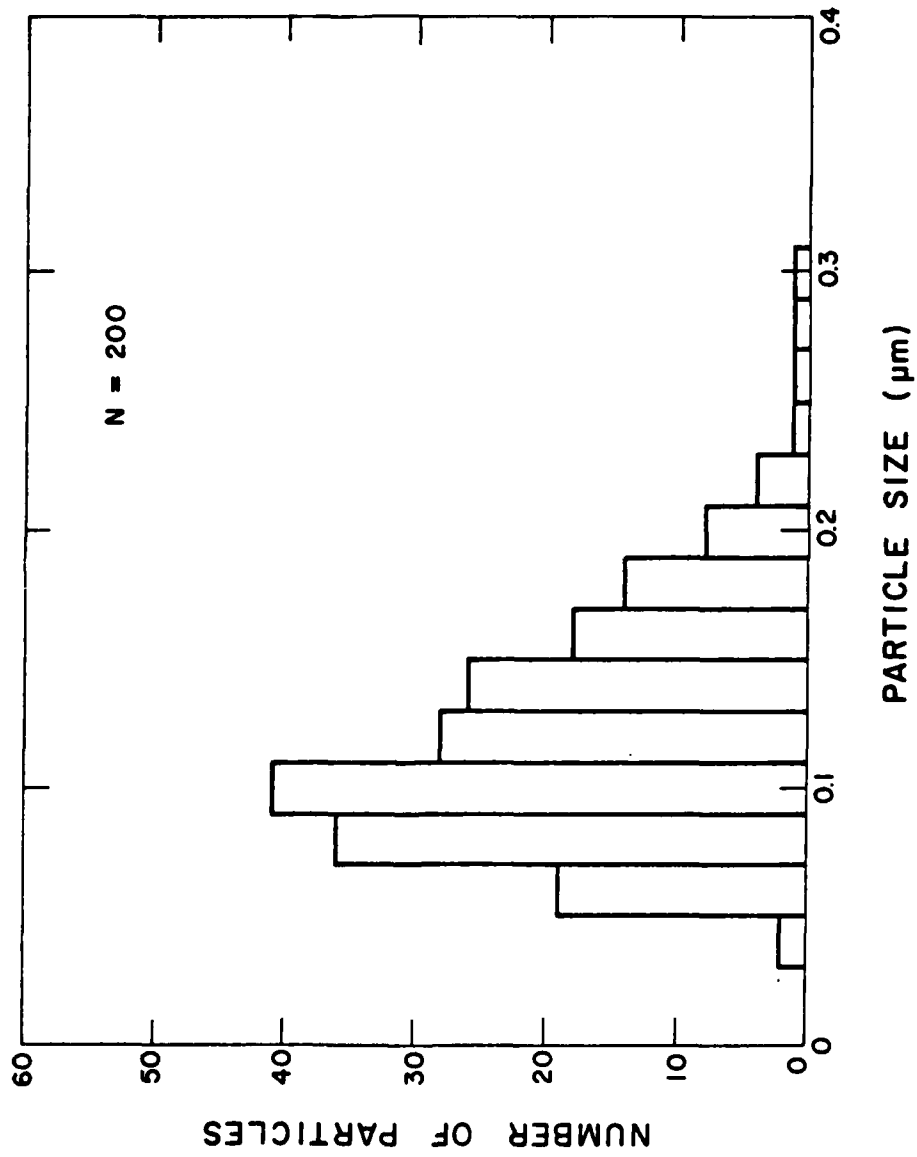


FIGURE 35. Smoke particle size distribution for stabilized Al/JP-10 slurry at  $T_{\infty}=1809$  K,  $O_2=10.4\%$ .

## V. SUMMARY AND CONCLUSIONS

### 5.1 SUMMARY

In this study, ignition and combustion of aluminum-based slurry droplets were explored both experimentally and analytically. Specifically, the effects of droplet diameter, ambient gas temperature, ambient oxygen mole fraction, and slurry composition on ignition and combustion times were studied together with the influence of these parameters on the mode of combustion and the nature of the residual condensed products.

Experimentally, the ignition and combustion of slurry droplets were studied by photographically observing probe-supported droplets in the post-flame gases of a flat-flame burner, similar to the previous studies conducted in our laboratory [2,5,6]. Individual slurry droplets having initial diameters ranging from about 500-1100  $\mu\text{m}$  were suspended on 125  $\mu\text{m}$  diameter silicon carbide filaments and rapidly exposed to the hot gases by quickly withdrawing a shield. Tests were conducted in a variety of essentially dry flames ( $\text{CO}/\text{O}_2/\text{N}_2$ ) and wet flames ( $\text{CH}_4/\text{O}_2/\text{N}_2$ ). For the dry environments, conditions were selected to provide a range of gas temperatures with nearly constant oxygen mole fraction, and vice versa. Oxygen mole fractions ranged from 0.10 to 0.25 and gas temperatures from 1250-1900 K. The surface structures of both unreacted agglomerates formed by the evaporation of the liquid JP-10 from the slurry and the residual products found on the support probe after combustion were studied using scanning electron microscopy. Identification of chemical compounds in the condensed phase combustion products, together with estimates of their relative proportions, were obtained using X-ray diffraction techniques. Stabilized and unstabilized Al/JP-10 slurries with approximately 42% solids loading,

as well as a stabilized Al/C/JP-10 slurry with approximately 36% and 9% Al and C loadings, respectively, were studied.

Theoretical aluminum slurry ignition and aluminum combustion models were applied to predict ignition times and burning times. To predict ignition times, the processes of slurry droplet heat-up, liquid fuel combustion, and agglomerate heat-up were modeled. Slurry droplet heat-up and liquid burnout were treated essentially in a conventional manner [43]. To account for the enhanced convective heat transfer compared to a solid sphere that occurs for the porous, and sometimes filigreed, aluminum agglomerates, an empirical transport enhancement factor was used as in previous work [2-5]. The criterion chosen for ignition was the attainment of a particular ignition temperature for the dry agglomerate. This criterion is consistent with the concept of mechanical breakdown of an oxide coating on the individual constituent aluminum particles and has been used by others in models of aluminum ignition [21,25].

Experimentally it was observed that after the agglomerate constituent particles coalesced, combustion generally proceeded with an axisymmetric flame zone around the aluminum droplet and surface accumulation of oxide on the leeward side. To model this combustion process with a minimum of complexity, the theoretical vapor-phase combustion analysis of Law [34] was adapted and extended to account for quasi-steady oxide build-up.

In a typical sequence of events for a stabilized Al/JP-10 slurry droplet, the original droplet swells as the JP-10 burns with transformation from an obviously liquid droplet to a fuzzy agglomerate where the JP-10 burnout nears completion. The agglomerate then heats up and the individual particles rapidly coalesce, indicated by a sharp decline in particle

diameter. Ignition was defined as the time at which coalescence was complete, and always coincided with the appearance of a vapor-phase flame for the Al/JP-10 slurries. After ignition, emission from the burning particle allows the liquid aluminum droplet to be distinguished from the oxide cap which forms. As burning proceeds, the overall particle diameter decreases as the relative size of the oxide cap grows. Later the flame appears to collapse on the surface and no smoke is visible. This event was chosen to signify the end of combustion.

Each of the three slurries tested produced a different agglomerate structure which was found to be an important factor in determining ignition times. The addition of stabilizing agents to an Al/JP-10 slurry formed loose-structured agglomerates with beneficial ignition characteristics compared to the compact agglomerates formed from the unstabilized slurry. Results were shown that quantify this effect. The minimum ignition temperatures as a function of initial diameter ranging from 450-1000  $\mu\text{m}$  were obtained for stabilized Al/JP-10 slurry droplets. The thermal ignition theory utilizing the concept of a constant ignition temperature ( $T_{\text{ign}} \approx 1250 \text{ K}$ ) and an empirical transport enhancement factor [2-5] ( $\xi \approx 2.2$ ) provided a reasonable interpretation of the agglomerate ignition time data except for slight deviation presumably due to the use of a single value of  $\xi$  for all diameters. The study of the oxygen mole fraction effect on ignition times, however, suggested that chemical reaction of the aluminum agglomerate may have some influence on ignition times with thermal effects dominating. The study of the diameter influence on  $\xi$  also suggested that further investigation of chemical effects during heat-up of aluminum agglomerates is warranted.

Experimental and theoretical burning times as functions of coalesced aluminum droplet size were compared. Two limiting theoretical cases were shown which essentially bracket the data. The first case employs the assumption of an impervious oxide cap, while the second case assumes that there are sufficient fissures and/or fumaroles in the cap to completely wet the cap with vaporizing aluminum. Similar absolute and trendwise agreement between theory and experiment was found for both the influence of oxygen mole fraction and gas temperature. In all cases, the experimental data were closer to the totally wet cap limit.

X-ray diffraction analysis of residual combustion products showed that  $\alpha\text{-Al}_2\text{O}_3$  was the sole product for the stabilized Al/JP-10 slurry where ignition was achieved. For the unstabilized Al/JP-10 slurry, small quantities of  $\delta\text{-Al}_2\text{O}_3$  were also present with the  $\alpha\text{-Al}_2\text{O}_3$ , along with traces of unburned aluminum. The aluminum/carbon SEM analysis of the smoke-particle size distribution showed that the predominant smoke particle size is probably smaller than  $0.1\ \mu\text{m}$ .

## 5.2 CONCLUSIONS

Based on combined experimental and theoretical studies of aluminum and aluminum/carbon slurries, the following conclusions were reached:

1. The composition of a slurry fuel is a strong factor in determining the structure of the agglomerate which is formed after the liquid fuel is consumed. The addition of stabilizing agents to an Al/JP-10 slurry formed a loose-structured agglomerate with beneficial ignition and combustion characteristics, especially for low-temperature conditions.

2. A thermal ignition theory utilizing the concept of an empirical constant ignition temperature,  $T_{ign} \approx 1250$  K, and an empirical convective enhancement factor,  $\xi \approx 2.2$ , provided a reasonable interpretation of agglomerate ignition data. However, the experimental ignition time dependence on ambient oxygen concentration, together with the observed decrease of minimum ambient gas temperature for ignition with diameter, suggests that chemical effects should be incorporated in an improved model.
3. Upon particle coalescence and ignition, vapor-phase burning occurred for Al/JP-10 slurry droplets, similar to that observed by others for single aluminum particles. The appearance of multiple flame zones, together with burning-time calculations, suggests that molten aluminum leaks through the oxide cap, which was observed to form on the leeward side of the aluminum droplets.
4. A relatively simple aluminum combustion model provided reasonable agreement with qualitative features of aluminum burning, as well as quantitative agreement with observed burning times, as long as particle fragmentation did not occur. Inclusion of radiation in the model suggests that dissociation of the oxide products in the flame and subsequent product diffusion to the surface are not responsible for surface oxide accumulation for particles in the size range studied, thus alternative mechanisms such as convection, thermophoresis and surface reactions may be responsible.

5. Complete oxidation of an aluminum/carbon slurry occurred only at the highest-temperature wet and dry flame conditions. For combustion at lower temperatures, appreciable quantities of aluminum carbide were found along with alumina in the condensed products. Subsequent oxidation of the aluminum carbide in a high-temperature flame was quite slow. Since equilibrium calculations indicated that the  $\text{Al}_4\text{C}_3$  should be essentially non-existent at the experimental conditions, it is likely that  $\text{Al}_4\text{C}_3$  conversion to  $\text{Al}_2\text{O}_3$  is limited by either chemical kinetics or diffusional resistance within the agglomerate, or both.

## REFERENCES

1. Szekely, Jr., G.A., "Experimental Evaluation of a Carbon Slurry Droplet Combustion Model," Ph.D. Thesis, The Pennsylvania State University, University Park, PA, 1982.
2. Szekely, Jr., G.A. and Faeth, G.M., "Combustion Properties of Carbon Slurry Drops," AIAA J., Vol. 20 (1982) 422.
3. Szekely, Jr., G.A. and Faeth, G.M., "Reaction of Carbon Black Slurry Agglomerates in Combustion Gases," Nineteenth Symposium (International) on Combustion, The Combustion Institute, Pittsburgh (1982) 1077-1085.
4. Szekely, Jr., G.A., Turns, S.R. and Faeth, G.M., "Effects of Carbon Black Properties on the Combustion of Carbon Black Slurry Agglomerates," Comb. and Flame, Vol. 58 (1984) 31.
5. Turns, S.R., Holl, J.T., Solomon, A.S.P. and Faeth, G.M., "Gasification of Boron Oxide and Boron Slurry Agglomerates in Combustion Gases," CPIA Pub. 412, Vol. I (1984) 31-44.
6. Holl, J.T., Turns, S.R., Solomon, A.S.P. and Faeth, G.M., "Ignition and Combustion of Boron Slurry Agglomerates," Comb. Sci. and Tech., Vol. 45 (1985) 147.
7. Wilson, Jr., R.P. and Williams, F.A., "Experimental Study of the Combustion of Single Aluminum Particles in O<sub>2</sub>/Ar," Thirteenth Symposium (International) on Combustion, The Combustion Institute, Pittsburgh (1971) 833-845.
8. Friedman, R. and Macek, A., "Ignition and Combustion of Aluminum Particles in Hot Ambient Gases," Comb. and Flame, Vol. 6 (1962) 9-19.
9. Friedman, R. and Macek, A., "Combustion Studies of Single Aluminum Particles," Ninth Symposium (International) on Combustion, The Combustion Institute, Pittsburgh (1963) 703-712.
10. Macek, A., "Fundamentals of Combustion of Single Aluminum and Beryllium Particles," Eleventh Symposium (International) on Combustion, The Combustion Institute, Pittsburgh (1967) 203-217.
11. Bartlett, R.W., Ong, Jr., J.N., Fassell, Jr., W.M., and Papp, C.A., "Estimating Aluminum Particle Combustion Kinetics," Comb. and Flame, Vol. 7 (1963) 227-234.
12. Prentice, J.L. and Nelson, L.S., "Differences Between the Combustion of Aluminum Droplets in Air and in an Oxygen-Argon Mixture," J. Electrochem. Soc., Vol. 115 (1968) 809.
13. Prentice, J.L. "Combustion of Pulse-Heated Single Particles of Aluminum and Beryllium," Comb. Sci. and Tech., Vol. 1 (1970) 385.

14. Prentice J.L., "Aluminum Droplet Combustion: Rates and Mechanisms in Wet and Dry Oxidizers," Naval Weapons Center, Rept. TP 5569, Apr. 1974.
15. Gurevich, M.A., Lapkina, K.I., and Ozerov, E.S., "Ignition Limits of Aluminum Particles," Comb. Expl. and Shockwaves, Vol. 6, No. 2 (1970) 154-157.
16. Derevyaga, M.E., Stesik, L.N., and Fedorin, E.A., "Ignition and Combustion of Aluminum and Zinc in Air," Comb. Expl. and Shockwaves, Vol. 13 (1977) 722-726.
17. Bourianes, R., "Combustion of Aluminum in Carbon-Dioxide and Oxygen Atmosphere," Comb. and Flame, Vol. 31 (1978) 89-91.
18. Smelkov, G.I., Aleksandrov, A.A., Pekhotikov, V.A., and Grishin, E.V., "Combustion of Large Aluminum Particles in an Air Flow," Comb. Expl. and Shockwaves, Vol. 14, No. 5 (1978) 581-584.
19. Ermakov, V.A., et al., "Temperature of Aluminum Particles at the Time of Ignition and Combustion," Comb. Expl. and Shockwaves, Vol. 18 (1982) 256.
20. Brzustowski, T.A. and Glassman, I., "Vapor-Phase Diffusion Flames in the Combustion of Magnesium and Aluminum: II. Experimental Observations in Oxygen Atmospheres," Progress in Astronautics and Aeronautics, Vol. 15, AIAA, Academic Press, New York (1964) 117-158.
21. Mellor, A.M. and Glassman, I., "A Physical Criterion for Metal Ignition," Pyrodynamics, Vol. 3 (1965) 43-64.
22. Kuehl, D.K., "The Ignition and Combustion of Small Diameter Aluminum Wires," Pyrodynamics, Vol. 3 (1965) 65-79.
23. Kuehl, D.K., "Ignition and Combustion of Aluminum and Beryllium," AIAA J., Vol. 3 (1965) 2239.
24. Mellor, A.M. and Glassman, I., "Augmented Ignition Efficiency for Aluminum," Combust. Sci. and Tech., Vol. 1 (1970) 437.
25. Price, E.W., "Combustion of Metalized Propellants," Progress in Astronautics and Aeronautics, Vol. 90, AIAA, New York, NY (1983) 479-513.
26. Polishchuk, D.I., Velikanova, V.L. and Nechitailo, I.N., "Combustion of Multicomponent Aluminum-Containing Systems," Advances in Aerosol Physics, Vol. 4 (1973) 89.
27. Velikanova, V.L., Polishchuk, D.I. and Nechitailo, I.N., "Ignition Temperature of Conglomerates Formed After Burning-Up of the Binder from Suspensions of Aluminum Powder in Kerosene," Advances in Aerosol Physics, Vol. 7 (1973) 101.

28. Polishchuk, D.I., et al., "Critical Ignition Conditions for Conglomerates of Aluminum Particles," Comb. Expl. and Shockwaves, Vol. 14 (1978) 175.
29. Khaikin, B.I., Bloshenko, V.N., and Merzhanov, A.G., "On the Ignition of Metal Particles," Comb. Expl. and Shockwaves, Vol. 6, No. 4 (1970) 412-422.
30. Brzustowski, T.A. and Glassman, I., "Vapor-Phase Diffusion Flames in the Combustion of Magnesium and Aluminum: I. Analytical Developments," Progress in Astronautics and Aeronautics, Vol. 15, AIAA, Academic Press, New York (1964) 75-115.
31. Kuehl, D.K. and Zwillenberg, M.L., "Predictions of Burning Times of Metal Particles," AIAA Paper No. 68-494, 1968.
32. Wilson, Jr., R.P., "Studies on Combustion of Aluminum Particles," Western States Section--The Combustion Institute, Spring Meeting, China Lake, CA, 1969.
33. Klyachko, L.A., "Combustion of a Stationary Particle of Low-Boiling Metal," Comb. Expl. and Shockwaves, Vol. 5, No. 3 (1969) 279-284.
34. Law, C.K., "A Simplified Theoretical Model for the Vapor-Phase Combustion of Metal Particles," Combust. Sci. and Tech., Vol. 7 (1973) 197-212.
35. Gremyachkin, V.M., Istratov, A.G., and Leipunskii, O.I., "Model for the Combustion of Metal Droplets," Comb. Expl. and Shockwaves, Vol. 11, No. 3 (1975) 313-318.
36. Keshavan, R. and Brzustowski, T.A., "Ignition of Aluminum Particle Streams," Combust. Sci. and Tech., Vol. 6 (1972) 203.
37. Kent, J.H., "A Noncatalytic Coating for Platinum-Rhodium Thermocouples," Combustion and Flame, Vol. 14 (1970) 279-282.
38. Taylor, P.H., "Physical and Chemical Inhibition of Premixed, Partially Quenched, Fuel-Rich Flames Upon Addition of Aqueous Alkali Salt Solutions," Ph.D. Thesis, The Pennsylvania State University, University Park, PA, 1984.
39. Grosshandler, W., Engel, M., and Russell, A., "Emissivity of Thermocouples of Combustion Measurements," Western States Section--The Combustion Institute, April, 1980.
40. Grosshandler, W., and Sawyer, R., "Pollutant Measurements in a Methanol Furnace," Western States Section--The Combustion Institute, March, 1977.
41. Langhaar, H.L., "Steady Flow in the Transition Length of a Straight Tube," Jr. Appl. Mech., June (1942) A-55-A-58.

42. Gordon, S. and McBride, B.J., "Computer Program for the Calculation of Complex Chemical Equilibrium Compositions, Rocket Performance, Incident and Reflected Shocks and Chapman-Jouget Detonations," NASA SP-273, 1971.
43. Faeth, G.M., "Current Status of Droplet and Liquid Combustion," Prog. Energy Combust. Sci., Vol. 3 (1977) 191.
44. Williams, F.A., Combustion Theory, Addison-Wesley, Reading, MA, 1965.
45. Faeth, G.M., "Status of Boron Combustion Research," CPIA Pub. 412, Vol. I (1984).
46. Anon., IMSL Library Reference Manual, IMSL, Inc., 1980, p. DVERK-1.
47. Wakao, N. and Kaguel, S., Heat and Mass Transfer in Packed Beds, Gordon and Breach Science Publishers, NY, 1982.
48. Glassman, I., Combustion, Academic Press, Inc., New York, 1977.
49. Svehla, R.A., "Estimated Viscosities and Thermal Conductivities of Gases at High Temperatures," NASA Technical Report R-132, 1962.
50. Touloukian, Y.S., et al, Thermal Radiative Properties, Vol. 8, Plenum Publishing Corporation, New York, 1970.
51. Hu, C.-Y., M.S. Thesis, West Virginia University, Morgantown, WV, 1964.
52. Polishchuk, D.I., Yankevich, V.L., and Nechitailo, I.N., "Evaporation and Combustion Kinetics of Thickened Hydrocarbon Fuels," Advances in Aerosol Physics, No. 2 (1972) 119-124.

APPENDIX A

JP-10 EVAPORATION CALIBRATION

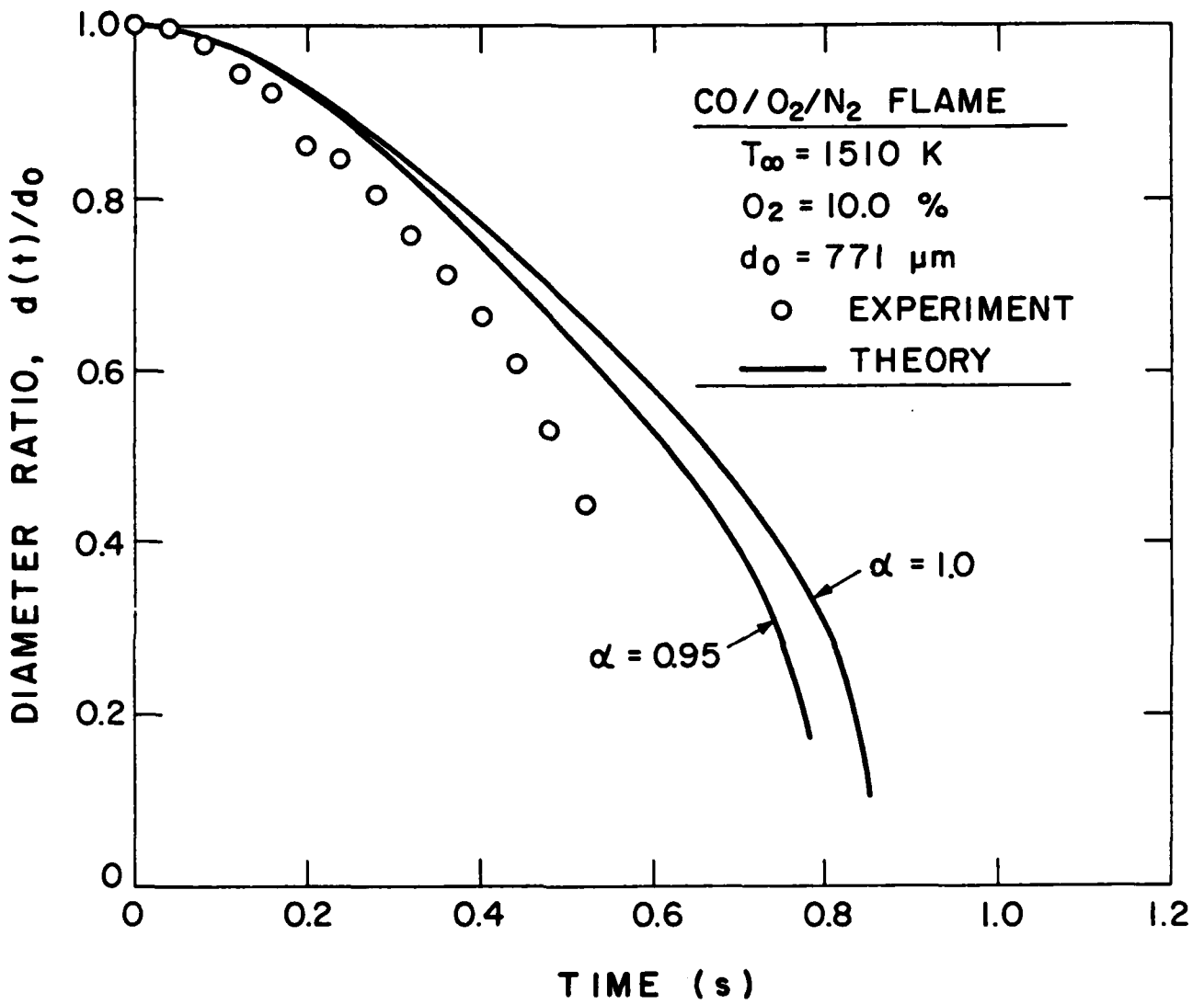


FIGURE A.1 Calibration for  $\alpha$  at  $T_{\infty}=1510 \text{ K}$ ,  $O_2=10.0\%$  dry flame condition.

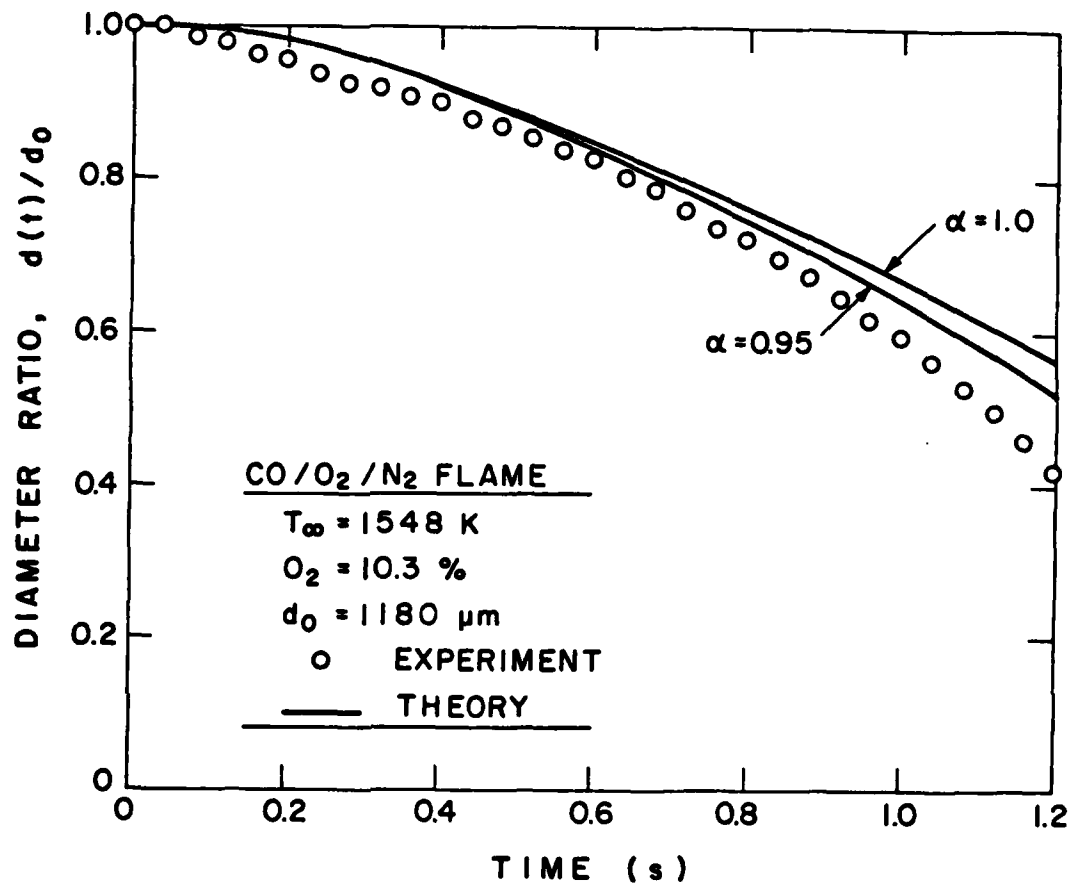


FIGURE A.2 Calibration for  $\alpha$  at  $T_{\infty}=1548 \text{ K}$ ,  $O_2=10.3\%$  dry flame condition.

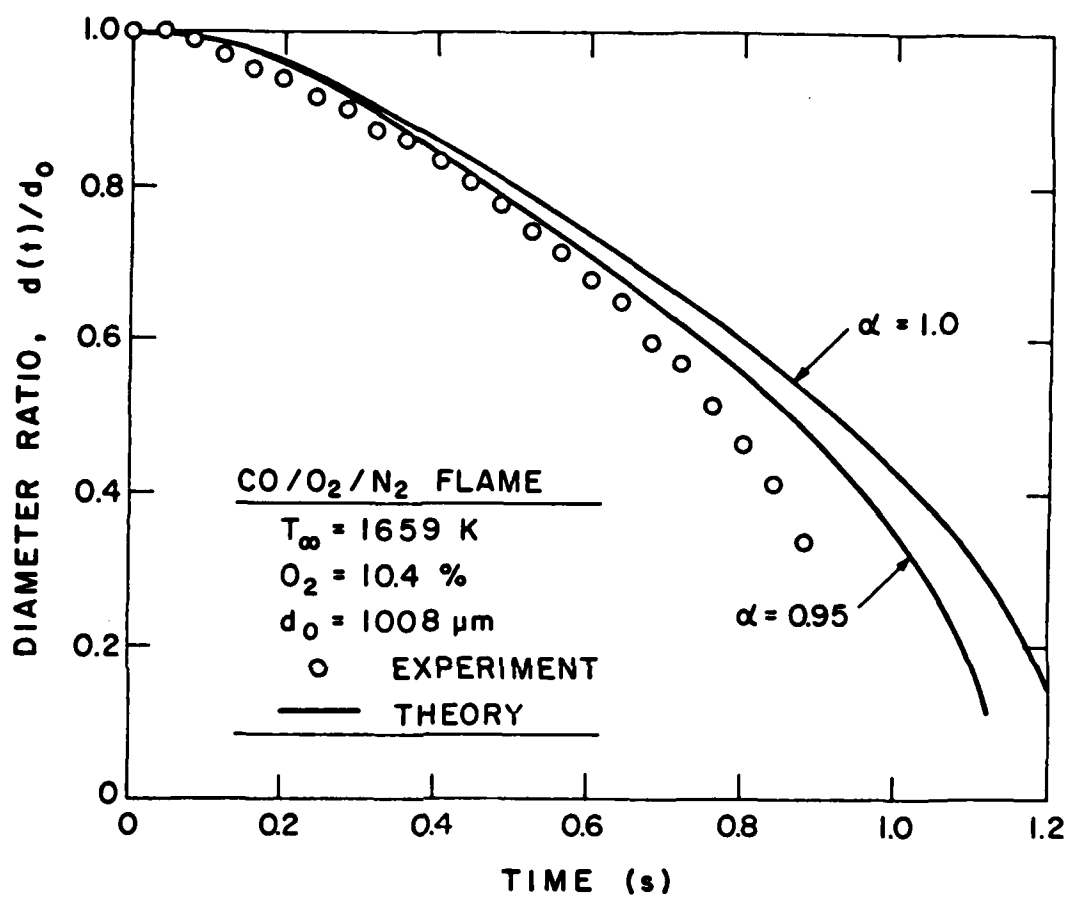


FIGURE A.3 Calibration for  $\alpha$  at  $T_{\infty}=1659 \text{ K}$ ,  $O_2=10.4\%$  dry flame condition.

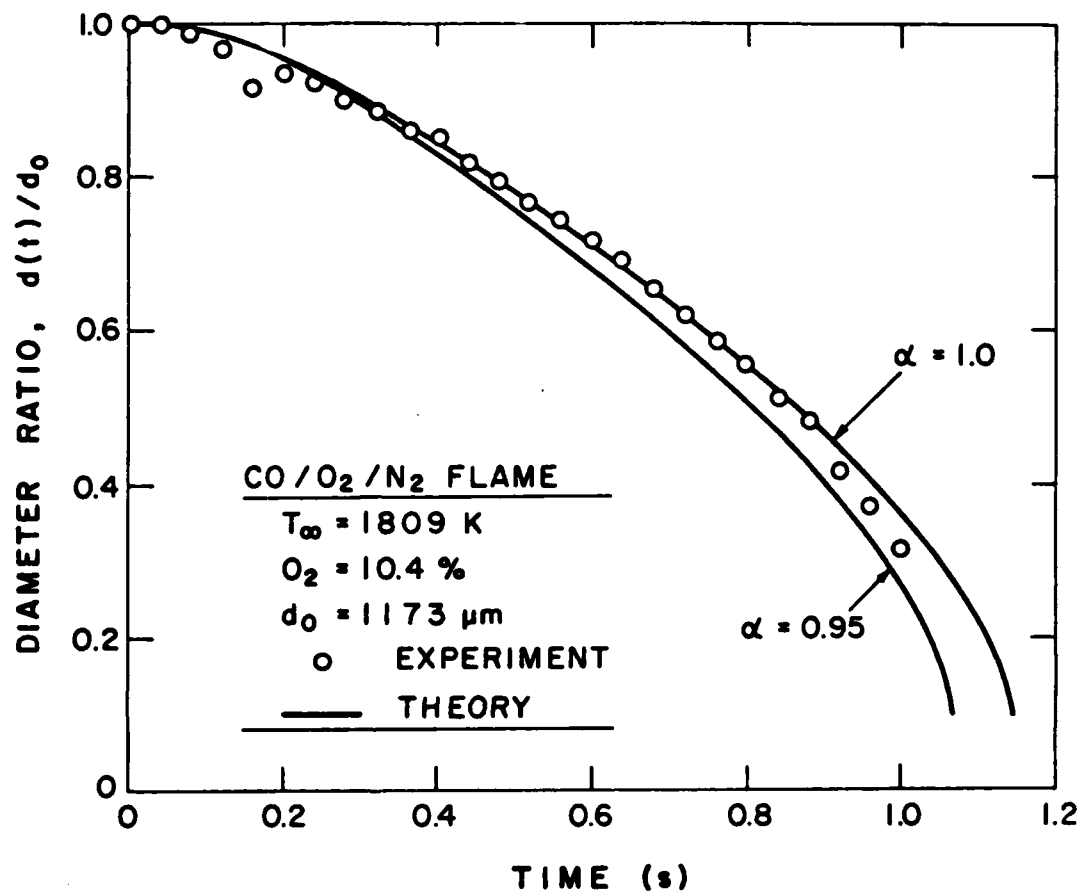


FIGURE A.4 Calibration for  $\alpha$  at  $T_{\infty}=1809 \text{ K}$ ,  $O_2=10.4\%$  dry flame condition.

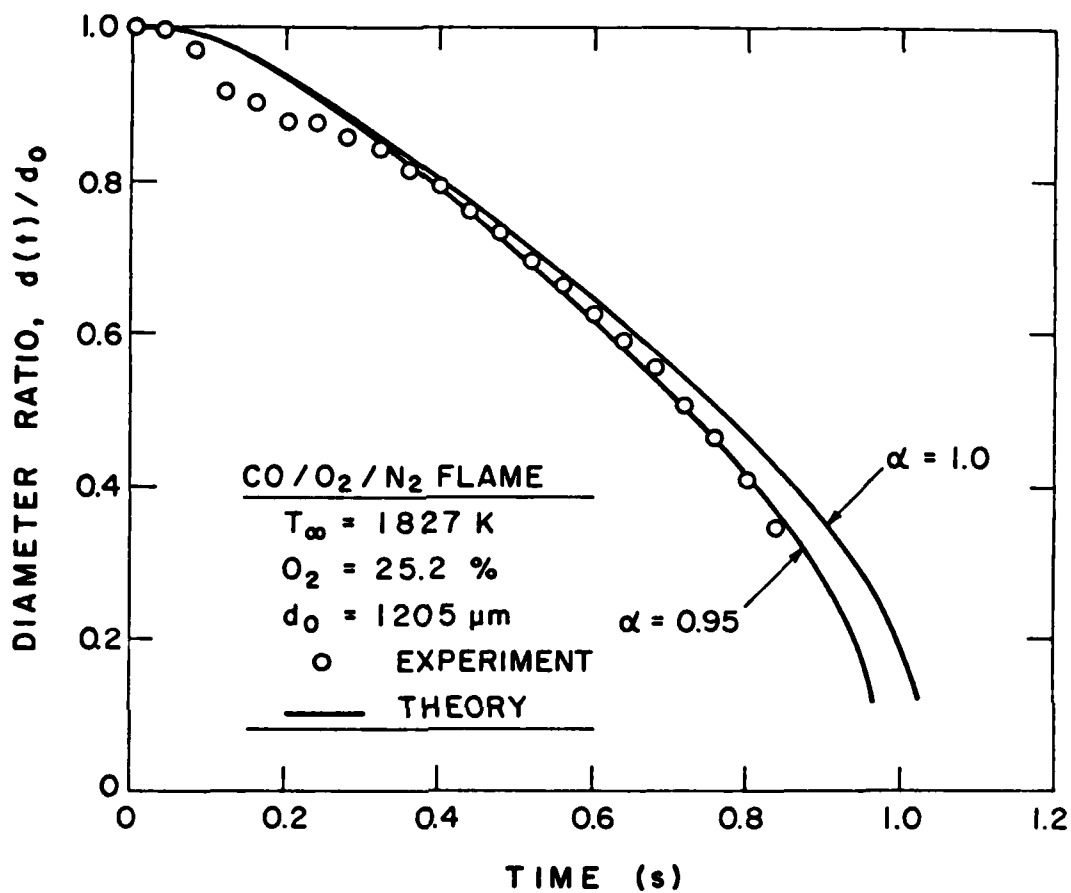


FIGURE A.5 Calibration for  $\alpha$  at  $T_{\infty}=1827 \text{ K}$ ,  $O_2=25.2\%$  dry flame condition.

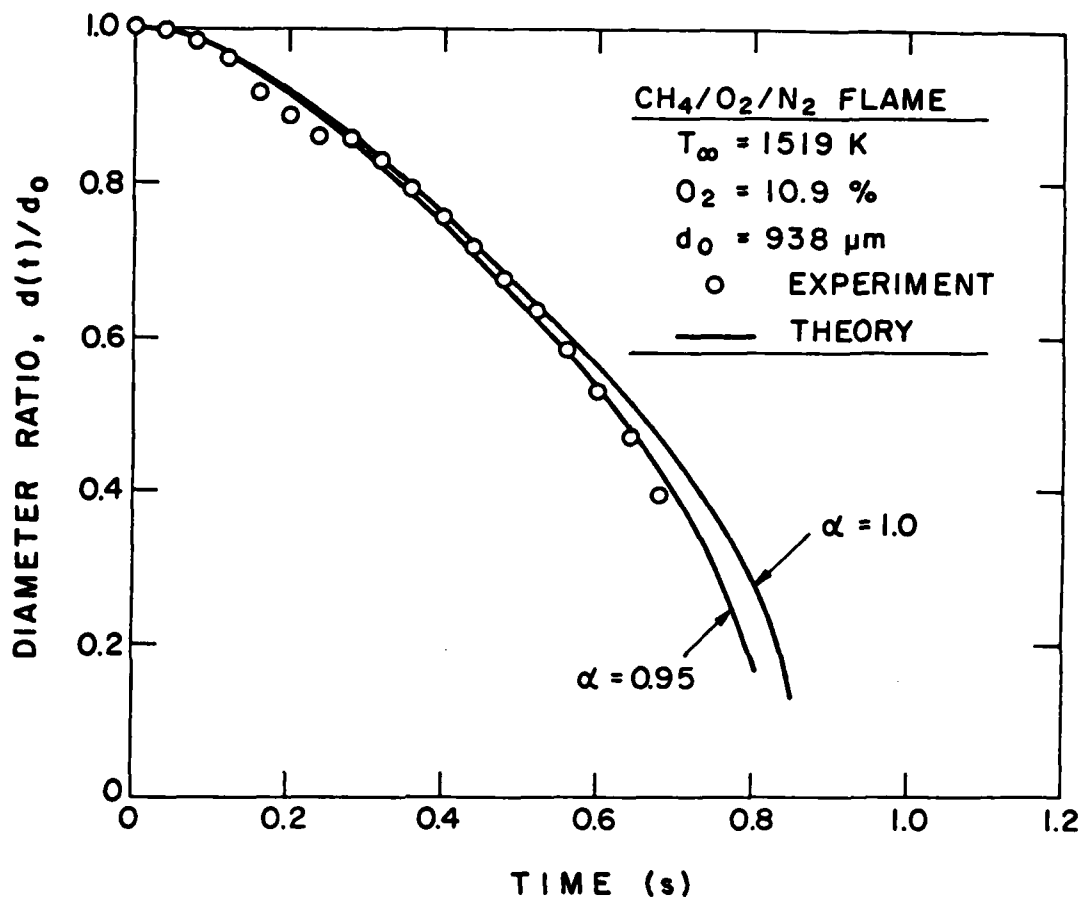


FIGURE A.6 Calibration for  $\alpha$  at  $T_{\infty}=1519 \text{ K}$ ,  $O_2=10.9\%$  wet flame condition.

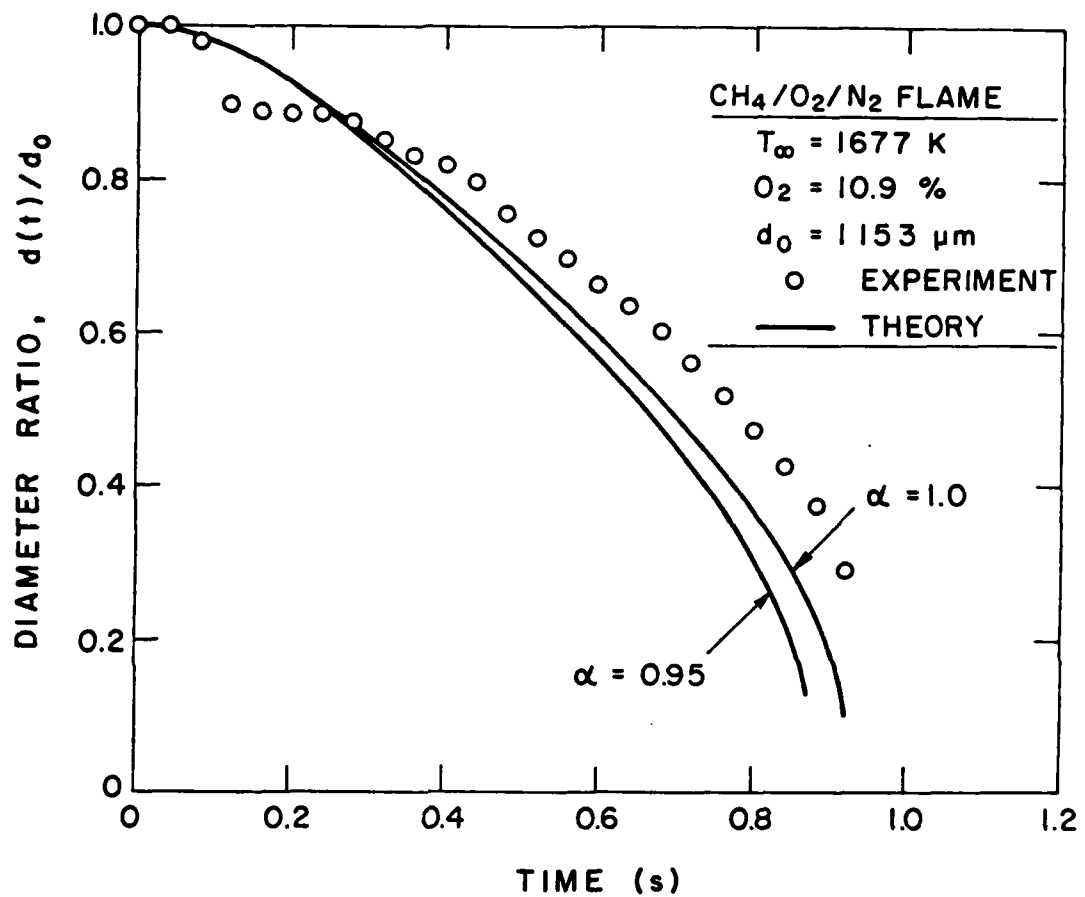


FIGURE A.7 Calibration for  $\alpha$  at  $T_{\infty}=1677 \text{ K}$ ,  $O_2=10.9\%$ , wet flame condition.

APPENDIX B

SLURRY IGNITION AND BURNING TIME DATA

TABLE B.1 - Ignition and Burning Times for Stabilized Al Slurry,  
 $T_{\infty} = 1510 \text{ K}$ ,  $\phi = 0.54$ ,  $O_2 = 10.0\%$ , Dry

$d_o(\mu\text{m})$	$d_m(\mu\text{m})$	Al Loading <sup>a</sup>	Ignition Time(s)	Burning Time(s)
445	-	-	no ignition	-
524	-	-	no ignition	-
635	441	0.50	0.74	0.80
745	458	0.40	0.76	0.86
826	502	0.38	0.92	1.12

<sup>a</sup> Each aluminum loading entry was estimated according to the following relation:

$$\text{Al loading} = \frac{\rho_{Al}}{\rho_{Al} + \rho_{JP} \left[ \left( \frac{d_o}{d_m} \right)^3 - \frac{\rho_{Al}}{\rho_{Al,o}} \right]}$$

where  $\rho_{JP}$  is the density of JP-10 at 300 K; and  $\rho_{Al,o}$  and  $\rho_{Al}$  are the densities of aluminum at 300 K and at the temperature when the agglomerate coalesces (assuming the melting point of  $Al_2O_3$ , i.e. 2303 K), respectively;  $d_o$ ,  $d_m$  are the initial droplet diameter and the molten aluminum droplet diameter at the instant of coalescence, respectively. Generally, values obtained are larger than the original loading of the slurries (ca. 0.42) because a certain amount of the JP-10 evaporated from the slurry droplets during preparation.

TABLE B.2 - Ignition and Burning Times for Stabilized Al Slurry,  
 $T_{\infty} = 1548 \text{ K}$ ,  $\phi = 0.59$ ,  $O_2 = 10.3\%$ , Dry

$d_o (\mu\text{m})$	$d_m (\mu\text{m})$	Al Loading	Ignition Time(s)	Burning Time(s)
458	306	0.47	0.40	0.24
523	351	0.47	0.48	0.40
610	380	0.40	0.56	0.72
682	403	0.36	0.62	0.92
813	-	-	0.76	-

TABLE B.3 - Ignition and Burning Times for Stabilized Al Slurry,  
 $T_{\infty} = 1659 \text{ K}$ ,  $\phi = 0.66$ ,  $O_2 = 10.4\%$ , Dry

$d_o (\mu\text{m})$	$d_m (\mu\text{m})$	Al Loading	Ignition Time(s)	Burning Time(s)
575	372	0.44	0.40	0.60
587	345	0.35	0.44	0.58
652	413	0.42	0.48	0.78
728	401	0.30	0.56	0.72
744	442	0.36	0.60	0.84
771	445	0.34	0.62	0.88
823	460	0.31	0.66	0.92

TABLE B.4 - Ignition and Burning Times for Stabilized Al Slurry,  
 $T_{\infty} = 1809 \text{ K}$ ,  $\phi = 0.58$ ,  $O_2 = 10.4\%$ , Dry

$d_o (\mu\text{m})$	$d_m (\mu\text{m})$	Al Loading	Ignition Time(s)	Burning Time(s)
489	320	0.45	0.32	0.50
519	335	0.43	0.32	0.54
557	321	0.34	0.36	0.48
593	368	0.40	0.36	0.52
610	403	0.46	0.40	0.68
611	408	0.47	0.42	0.64
621	405	0.44	0.38	0.64
653	410	0.41	0.44	0.60
676	428	0.42	0.50	0.78
721	449	0.40	0.52	0.94
721	474	0.45	0.50	0.76
742	440	0.36	0.46	0.74
759	493	0.44	0.52	-
768	499	0.44	0.52	-
769	458	0.36	0.50	1.04
778	506	0.44	0.56	-
785	510	0.44	0.60	-
788	578	0.56	0.62	1.34
815	530	0.44	0.64	-
815	559	0.49	0.88	-
847	558	0.45	0.70	1.40
848	582	0.49	0.84	-
849	599	0.52	0.92	1.21
852	582	0.49	0.96	1.20
881	603	0.49	0.80	-
900	620	0.50	0.94	1.46
908	597	0.45	0.66	1.74
957	679	0.53	0.84	1.92
969	659	0.48	0.70	1.70
986	701	0.53	0.76	1.52
1035	715	0.50	0.82	1.74
1061	697	0.45	0.78	1.60
1066	757	0.53	0.78	2.00
1096	706	0.43	0.92	1.88

TABLE B.5 - Ignition and Burning Times for Stabilized Al Slurry,  
 $T_{\infty} = 1868 \text{ K}$ ,  $\phi = 0.58$ ,  $O_2 = 11.4\%$ , Dry

$d_o (\mu\text{m})$	$d_m (\mu\text{m})$	Al Loading	Ignition Time(s)	Burning Time(s)
885	675	0.60	0.58	1.46
965	664	0.50	0.56	1.10
1050	724	0.50	0.84	1.72

TABLE B.6 - Ignition and Burning Times for Stabilized Al Slurry,  
 $T_{\infty} = 1888 \text{ K}$ ,  $\phi = 0.58$ ,  $O_2 = 12.9\%$ , Dry

$d_o (\mu\text{m})$	$d_m (\mu\text{m})$	Al Loading	Ignition Time(s)	Burning Time(s)
916	662	0.55	0.68	1.62
939	615	0.45	0.68	1.36
991	685	0.50	0.60	1.52

TABLE B.7 - Ignition and Burning Times for Stabilized Al Slurry,  
 $T_{\infty} = 1869 \text{ K}$ ,  $\phi = 0.58$ ,  $O_2 = 13.8\%$ , Dry

$d_o (\mu\text{m})$	$d_m (\mu\text{m})$	Al Loading	Ignition Time(s)	Burning Time(s)
904	624	0.50	0.60	1.26
1010	654	0.44	0.64	1.40

TABLE B.8 - Ignition and Burning Times for Stabilized Al Slurry,  
 $T_{\infty} = 1827 \text{ K}$ ,  $\phi = 0.37$ ,  $O_2 = 25.2\%$ , Dry

$d_o (\mu\text{m})$	$d_m (\mu\text{m})$	Al Loading	Ignition Time(s)	Burning Time(s)
471	310	0.45	0.22	0.28
538	354	0.45	0.24	0.30
600	394	0.45	0.32	0.42
699	419	0.37	0.36	0.46
700	481	0.49	0.36	0.56
806	519	0.43	0.40	0.64

TABLE B.9 - Ignition and Burning Times for Stabilized Al Slurry,  
 $T_{\infty} = 1907 \text{ K}$ ,  $\phi = 0.58$ ,  $O_2 = 10.4\%$ , Dry with Ar Diluent

$d_o (\mu\text{m})$	$d_m (\mu\text{m})$	Al Loading	Ignition Time(s)	Burning Time(s)
660	428	0.44	0.48	0.72
689	436	0.42	0.44	0.86
689	439	0.42	0.48	0.80
695	443	0.42	0.50	0.70
721	490	0.48	0.58	0.90

TABLE B.10 - Ignition and Burning Times for Stabilized Al Slurry,  
 $T_{\infty} = 1417 \text{ K}$ ,  $\phi = 0.50$ ,  $O_2 = 10.9\%$ , Wet

$d_o (\mu\text{m})$	$d_m (\mu\text{m})$	Al Loading	Ignition Time(s)	Burning Time(s)
519	367	0.52	0.54	0.54
525	366	0.51	0.48	0.38
627	381	0.38	0.48	0.56
727	496	0.49	0.70	0.84
811	545	0.47	0.76	0.98
935	548	0.35	0.94	1.08

TABLE B.11 - Ignition and Burning Times for Stabilized Al Slurry,  
 $T_{\infty} = 1519 \text{ K}$ ,  $\phi = 0.50$ ,  $O_2 = 10.9\%$ , Wet

$d_o (\mu\text{m})$	$d_m (\mu\text{m})$	Al Loading	Ignition Time(s)	Burning Time(s)
512	403	0.64	0.40	0.50
549	393	0.54	0.44	0.68
629	489	0.62	0.58	0.90
662	518	0.63	0.58	-
683	513	0.59	0.64	1.0
809	496	0.39	0.68	1.02
843	532	0.41	0.80	-

TABLE B.12 - Ignition and Burning Times for Stabilized Al Slurry,  
 $T_{\infty} = 1677 \text{ K}$ ,  $\phi = 0.58$ ,  $O_2 = 10.9\%$ , Wet

$d_o (\mu\text{m})$	$d_m (\mu\text{m})$	Al Loading	Ignition Time(s)	Burning Time(s)
541	312	0.50	0.28	0.32
519	336	0.44	0.34	-
552	400	0.55	0.38	0.60
669	413	0.39	0.48	1.00
807	524	0.44	0.62	1.14

TABLE B.13 - Ignition and Burning Times for Stabilized Al Slurry,  
 $T_{\infty} = 1785 \text{ K}$ ,  $\phi = 0.62$ ,  $O_2 = 10.3\%$ , Wet

$d_o (\mu\text{m})$	$d_m (\mu\text{m})$	Al Loading	Ignition Time(s)	Burning Time(s)
441	304	0.50	0.24	0.42
572	373	0.44	0.32	0.56
616	435	0.52	0.34	0.74
683	458	0.47	0.44	0.84
685	488	0.53	0.39	0.91
714	434	0.38	0.46	0.72
876	550	0.41	0.52	1.12

TABLE B.14 - Ignition and Burning Times for Unstabilized Al Slurry,  
 $T_{\infty} = 1510 \text{ K}$ ,  $\phi = 0.54$ ,  $O_2 = 10.0\%$ , Dry

$d_o (\mu\text{m})$	$d_m (\mu\text{m})$	Al Loading	Ignition Time(s)	Burning Time(s)
523	414	0.64	0.64	-
681	525	0.62	-	1.20
685	496	0.55	0.92	-
701	521	0.58	0.92	0.96
813	583	0.54	1.00	1.44
832	564	0.48	-	1.24
862	622	0.54	-	1.26
915	621	0.48	-	1.44
991	686	0.50	1.74	1.50

TABLE B.15 - Ignition and Burning Times for Unstabilized Al Slurry,  
 $T_{\infty} = 1548 \text{ K}$ ,  $\phi = 0.59$ ,  $O_2 = 10.3\%$ , Dry

$d_o (\mu\text{m})$	$d_m (\mu\text{m})$	Al Loading	Ignition Time(s)	Burning Time(s)
594	443	0.58	0.58	0.72
627	470	0.58	0.68	-
684	491	0.54	0.76	0.90
695	538	0.62	0.76	0.90
794	548	0.50	1.16	1.24
851	574	0.48	0.98	1.26
877	636	0.55	-	1.20
911	611	0.47	1.16	1.34
927	728	0.64	-	1.44
1018	641	0.41	1.32	1.22

TABLE B.16 - Ignition and Burning Times for Unstabilized Al Slurry,  
 $T_{\infty} = 1659 \text{ K}$ ,  $\phi = 0.66$ ,  $O_2 = 10.4\%$ , Dry

$d_o (\mu\text{m})$	$d_m (\mu\text{m})$	Al Loading	Ignition Time(s)	Burning Time(s)
569	471	0.69	0.54	0.74
574	450	0.63	0.52	0.70
617	466	0.59	0.58	0.84
733	552	0.59	0.80	1.08
769	606	0.64	0.70	1.06
849	623	0.56	0.92	1.52
875	-	-	1.00	-
953	688	0.54	1.10	1.34

TABLE B.17 - Ignition and Burning Times for Unstabilized Al Slurry,  
 $T_{\infty} = 1809 \text{ K}$ ,  $\phi = 0.58$ ,  $O_2 = 10.4\%$ , Dry

$d_o(\mu\text{m})$	$d_m(\mu\text{m})$	Al Loading	Ignition Time(s)	Burning Time(s)
557	427	0.61	0.38	0.74
591	494	0.71	0.42	0.98
653	451	0.50	0.50	0.92
654	479	0.56	0.48	0.94
752	555	0.57	0.60	-
759	506	0.46	0.62	1.08
761	577	0.60	0.64	1.48
790	547	0.50	0.68	1.04
829	508	0.39	0.66	1.08
876	643	0.56	0.72	1.74
882	-	-	0.78	-
889	616	0.50	0.80	1.26
929	639	0.49	0.84	1.32
935	660	0.52	0.88	1.74
970	640	0.45	0.94	1.60
992	590	0.36	0.86	1.16

APPENDIX C

SLURRY DROPLET DIAMETER HISTORIES

TABLE C.1 - Diameter Versus Time,  $T_{\infty} = 1510$  K,  $\phi = 0.54$ ,  $O_2 = 10.0\%$ , Dry

Time(s)	<u>Stabilized Al/JP-10</u>		<u>Al/C/JP-10</u>	
	d(t)	d(t)/d <sub>0</sub>	d(t)	d(t)/d <sub>0</sub>
0.0	826	1.00	821	1.00
0.08	842	1.02	808	0.98
0.16	742	0.90	727	0.89
0.24	903	1.09	834	1.02
0.32	817	0.99	898	1.09
0.40	669	0.81	847	1.03
0.48	573	0.69	927	1.13
0.56	745	0.90	921	1.12
0.64	806	0.98	945	1.15
0.72	772	0.94	903	1.10
0.80	743	0.90	856	1.04
0.88	655	0.79	892	1.09
0.96	502	0.61	852	1.04
1.04	516	0.63	795	0.97
1.12	466	0.56	848	1.03
1.20	490	0.59	863	1.05
1.28	479	0.58	785	0.96
1.36	464	0.56	815	1.03
1.44	421	0.51	767	0.93
1.52	427	0.52	777	0.95
1.60	525	0.64	815	0.99
1.68	503	0.61	805	0.98
1.76	455	0.55	845	1.03
1.84	416	0.50	779	0.95
1.92	449	0.54	838	1.02
2.00	428	0.52	816	0.99
2.08	419	0.51	838	1.02
2.16	426	0.52	770	0.94
2.24	428	0.52	859	1.05
2.32	412	0.50	837	1.02
2.40	410	0.50	833	1.01

TABLE C.2 ~ Diameter Versus Time,  $T_{\infty} = 1659 \text{ K}$ ,  $\phi = 0.66$ ,  $O_2 = 10.4\%$ , Dry

Time(s)	<u>Stabilized Al/JP-10</u>		<u>Unstabilized Al/JP-10</u>		<u>Al/C/JP-10</u>	
	d(t)	d(t)/d <sub>0</sub>	d(t)	d(t)/d <sub>0</sub>	d(t)	d(t)/d <sub>0</sub>
0.0	823	1.00	769	1.00	846	1.00
0.04	811	0.99	766	1.00	846	1.00
0.08	832	1.01	763	0.99	854	1.01
0.12	881	1.07	764	0.99	896	1.06
0.16	900	1.09	629	0.82	894	1.06
0.20	860	1.04	697	0.91	880	1.04
0.24	828	1.01	708	0.92	850	1.00
0.28	815	0.99	716	0.93	811	0.96
0.32	802	0.97	718	0.93	917	1.08
0.36	795	0.97	719	0.93	918	1.09
0.40	798	0.97	718	0.93	883	1.04
0.44	837	1.02	730	0.95	775	0.92
0.48	850	1.03	722	0.94	880	1.04
0.52	789	0.96	723	0.94	919	1.09
0.56	864	1.05	724	0.94	897	1.06
0.60	801	0.97	721	0.94	897	1.06
0.64	554	0.67	717	0.93	930	1.10
0.68	457	0.56	654	0.85	872	1.03
0.72	489	0.59	618	0.80	831	0.98
0.76	490	0.60	620	0.81	918	1.09
0.80	477	0.58	603	0.78	842	1.00
0.84	440	0.54	561	0.73	826	0.98
0.88	421	0.51	563	0.73	916	1.08
0.92	458	0.56	568	0.74	921	1.09
0.96	447	0.54	571	0.74	845	1.00
1.00	446	0.54	569	0.74	875	1.03
1.04	441	0.54	557	0.72	847	1.00
1.08	454	0.55	556	0.72	873	1.03
1.12	418	0.51	555	0.72	883	1.04
1.16	454	0.55	550	0.71	857	1.01
1.20	453	0.55	551	0.72	816	0.97
1.24	451	0.55	542	0.71	900	1.06
1.28	442	0.54	529	0.69	824	0.97
1.32	449	0.55	537	0.70	841	0.99
1.36	441	0.54	543	0.71	906	1.07
1.40	416	0.51	572	0.74	895	1.06
1.44	418	0.51	556	0.72	891	1.05
1.48	419	0.51	553	0.72	923	1.09
1.52	437	0.53	531	0.69	833	0.98
1.56	419	0.51	560	0.73	817	0.97
1.60	406	0.49	596	0.77	728	0.86
1.64	450	0.55	569	0.74	856	1.01
1.68	422	0.51	582	0.76	851	1.01
1.72	422	0.51	512	0.67	793	0.94
1.76	386	0.47	512	0.67	713	0.84

TABLE C.2 (Continued)

1.80	429	0.52	511	0.66	878	1.04
1.84	402	0.49	510	0.66	734	0.87
1.88	422	0.51	497	0.65	757	0.90
1.92	413	0.50	500	0.65	865	1.02
1.96	413	0.50	496	0.65	829	0.98

---

TABLE C.3 - Diameter Versus Time,  $T_{\infty} = 1809 \text{ K}$ ,  $\phi = 0.58$ ,  $O_2 = 10.4\%$ , Dry

Time(s)	<u>Stabilized Al/JP-10</u>		<u>Unstabilized Al/JP-10</u>		<u>Al/C/JP-10</u>	
	d(t)	d(t)/d <sub>0</sub>	d(t)	d(t)/d <sub>0</sub>	d(t)	d(t)/d <sub>0</sub>
0.0	847	1.00	889	1.00	818	1.00
0.04	844	1.00	899	1.01	811	0.99
0.08	845	1.00	877	0.99	814	1.00
0.12	870	1.03	853	0.96	908	1.11
0.16	867	1.02	795	0.89	851	1.04
0.20	849	1.00	782	0.88	793	0.97
0.24	840	0.99	797	0.90	829	1.01
0.28	861	1.02	794	0.89	783	0.96
0.32	804	0.95	763	0.86	869	1.06
0.36	757	0.89	745	0.84	851	1.04
0.40	767	0.91	742	0.83	859	1.05
0.44	785	0.93	740	0.83	862	1.05
0.48	801	0.95	746	0.84	816	1.00
0.52	793	0.94	753	0.85	852	1.04
0.56	799	0.94	736	0.83	865	1.06
0.60	806	0.95	750	0.84	878	1.07
0.64	786	0.93	757	0.85	860	1.05
0.68	578	0.68	753	0.85	871	1.06
0.72	544	0.64	735	0.83	897	1.10
0.76	556	0.66	670	0.75	888	1.09
0.80	570	0.67	616	0.69	859	1.05
0.84	566	0.67	618	0.70	864	1.06
0.88	549	0.65	612	0.69	903	1.10
0.92	561	0.66	663	0.75	839	1.03
0.96	518	0.61	616	0.69	724	0.89
1.00	516	0.61	593	0.67	843	1.03
1.04	515	0.61	557	0.63	802	0.98
1.08	508	0.60	580	0.65	853	1.04
1.12	512	0.60	570	0.64	811	0.99
1.16	507	0.60	591	0.66	863	1.06
1.20	508	0.60	609	0.69	808	0.99
1.24	528	0.62	607	0.68	840	1.03
1.28	507	0.60	631	0.71	766	0.94
1.32	498	0.59	609	0.69	815	1.00
1.36	509	0.60	609	0.69	828	1.01
1.40	508	0.60	615	0.69	818	1.00
1.44	477	0.56	613	0.69	814	1.00
1.48	475	0.56	612	0.69	894	1.09
1.52	476	0.56	548	0.62	905	1.11
1.56	467	0.55	533	0.60	816	1.00
1.60	473	0.56	538	0.61	857	1.05
1.64	487	0.57	553	0.62	862	1.05
1.68	496	0.59	565	0.64	827	1.01
1.72	526	0.62	536	0.60	780	0.95
1.76	489	0.58	527	0.59	872	1.07

TABLE C.3 (Continued)

1.80	482	0.57	531	0.60	852	1.04
1.84	477	0.56	566	0.64	868	1.06
1.88	457	0.54	575	0.65	855	1.05
1.92	464	0.55	559	0.63	809	0.99
1.96	453	0.54	572	0.64	815	1.00
2.00	453	0.53	513	0.58	809	0.99
2.04	453	0.53	508	0.57	753	0.92

---

TABLE C.4 - Diameter Versus Time,  $T_{\infty} = 1827 \text{ K}$ ,  $\phi = 0.37$ ,  $O_2 = 25.2\%$ , Dry

Time(s)	<u>Stabilized Al/JP-10</u>		<u>Al/C/JP-10</u>	
	d(t)	d(t)/d <sub>0</sub>	d(t)	d(t)/d <sub>0</sub>
0.00	806	1.00	856	1.00
0.04	809	1.00	849	0.99
0.08	854	1.06	857	1.00
0.12	742	0.92	951	1.11
0.16	790	0.98	860	1.00
0.20	738	0.92	946	1.11
0.24	797	0.99	943	1.10
0.28	774	0.96	966	1.13
0.32	843	1.05	972	1.14
0.36	798	0.99	1013	1.18
0.40	519	0.64	1001	1.17
0.44	571	0.71	998	1.17
0.48	536	0.66	997	1.17
0.52	530	0.66	989	1.16
0.56	505	0.63	996	1.16
0.60	508	0.63	967	1.13
0.64	444	0.55	923	1.08
0.68	436	0.54	891	1.04
0.72	452	0.56	875	1.02
0.76	458	0.57	809	0.95
0.80	445	0.55	722	0.84
0.84	410	0.51	713	0.83
0.88	370	0.46	669	0.78
0.92	375	0.47	591	0.69
0.96	380	0.47	590	0.69
1.00	381	0.47	590	0.69

TABLE C.5 - Diameter Versus Time for Stabilized Al/JP-10 Slurry,  
 $T_{\infty} = 1907 \text{ K}$ ,  $\phi = 0.58$ ,  $O_2 = 10.4\%$ ,  $CO/O_2/Ar$

Time(s)	Run 1		Run 2		Run 3	
	d(t)	d(t)/d <sub>0</sub>	d(t)	d(t)/d <sub>0</sub>	d(t)	d(t)/d <sub>0</sub>
0.00	689	1.00	689	1.00	695	1.00
0.04	672	0.98	679	0.98	698	1.01
0.08	687	1.00	691	1.00	697	1.00
0.12	718	1.04	708	1.03	717	1.03
0.16	695	1.01	705	1.02	703	1.01
0.20	680	0.99	690	1.00	702	1.01
0.24	679	0.99	647	0.94	737	1.06
0.28	676	0.98	678	0.98	819	1.18
0.32	761	1.10	694	1.01	856	1.23
0.36	767	1.11	689	1.00	865	1.25
0.40	747	1.08	748	1.09	832	1.20
0.44	462	0.67	716	1.04	885	1.27
0.48	484	0.70	439	0.64	523	0.75
0.52	470	0.68	454	0.66	443	0.64
0.56	452	0.66	455	0.66	464	0.67
0.60	479	0.70	442	0.64	448	0.64
0.64	454	0.66	433	0.63	457	0.66
0.68	427	0.62	423	0.61	459	0.66
0.72	444	0.64	436	0.63	454	0.65
0.76	442	0.64	397	0.58	450	0.65
0.80	452	0.66	417	0.60	429	0.62
0.84	461	0.67	387	0.56	441	0.63
0.88	457	0.66	405	0.59	458	0.66
0.92	432	0.63	430	0.62	466	0.67
0.96	459	0.67	407	0.59	446	0.64
1.00	442	0.64	380	0.55	462	0.67
1.04	425	0.62	401	0.58	427	0.61
1.08	421	0.61	386	0.56	417	0.60
1.12	434	0.63	408	0.59	431	0.62
1.16	409	0.59	390	0.57	393	0.57
1.20	407	0.59	355	0.52	379	0.55
1.24	401	0.58	385	0.56	364	0.52
1.28	421	0.61	402	0.58	401	0.58
1.32	384	0.56	396	0.57	420	0.60
1.36	385	0.56	407	0.59	394	0.57
1.40	393	0.57	407	0.59	410	0.59
1.44	390	0.57	411	0.60	389	0.56
1.48	384	0.56	435	0.63	379	0.55
1.52	394	0.57	415	0.60	398	0.57
1.56	399	0.58	434	0.63	383	0.55
1.60	382	0.55	389	0.56	383	0.55

TABLE C.6 - Diameter Versus Time,  $T_{\infty} = 1417 \text{ K}$ ,  $\phi = 0.50$ ,  $O_2 = 10.9\%$ , Wet

Time(s)	<u>Stabilized Al/JP-10</u>		<u>Al/C/JP-10</u>	
	d(t)	d(t)/d <sub>0</sub>	d(t)	d(t)/d <sub>0</sub>
0.00	935	1.00	926	1.00
0.04	940	1.01	926	1.00
0.08	928	0.99	936	1.01
0.12	981	1.05	995	1.07
0.16	1006	1.08	1026	1.11
0.20	887	0.95	1004	1.08
0.24	1138	1.22	979	1.06
0.28	933	1.00	948	1.02
0.32	885	0.95	1001	1.08
0.36	857	0.92	1000	1.08
0.40	899	0.96	1015	1.10
0.44	866	0.93	1030	1.11
0.48	908	0.97	1022	1.10
0.52	914	0.98	1029	1.11
0.56	904	0.97	1029	1.11
0.60	913	0.98	1029	1.11
0.64	909	0.97	1047	1.13
0.68	921	0.98	1020	1.10
0.72	926	0.99	1012	1.09
0.76	922	0.99	1020	1.10
0.80	919	0.98	1007	1.09
0.84	896	0.96	1020	1.10
0.88	893	0.95	1012	1.09
0.92	611	0.65	1013	1.09
0.96	548	0.59	1005	1.09
1.00	596	0.64	1002	1.08
1.04	528	0.56	1003	1.08
1.08	578	0.62	1007	1.09
1.12	555	0.59	1007	1.09
1.16	584	0.62	1000	1.08
1.20	583	0.62	1006	1.09
1.24	563	0.60	1005	1.09
1.28	579	0.62	1006	1.09
1.32	583	0.62	1001	1.08
1.36	542	0.58	1010	1.09
1.40	563	0.60	1006	1.09
1.44	563	0.60	998	1.08
1.48	575	0.62	1002	1.08
1.52	582	0.62	1007	1.09
1.56	559	0.60	1001	1.08
1.60	572	0.61	1009	1.09
1.64	583	0.62	1006	1.09
1.68	541	0.58	999	1.08
1.72	552	0.59	999	1.08
1.76	573	0.61	999	1.08

TABLE C.6 (Continued)

1.80	597	0.64	1001	1.08
1.84	567	0.61	997	1.08
1.88	523	0.56	999	1.08
1.92	557	0.60	1004	1.08
1.96	529	0.57	1012	1.09
2.00	526	0.56	1011	1.09

---

TABLE C.7 - Diameter Versus Time,  $T_{\infty} = 1519 \text{ K}$ ,  $\phi = 0.50$ ,  $O_2 = 10.9\%$ , Wet

Time(s)	Stabilized Al/JP-10		Al/C/JP-10	
	d(t)	d(t)/d <sub>0</sub>	d(t)	d(t)/d <sub>0</sub>
0.0	809	1.00	872	1.00
0.04	796	0.98	871	1.00
0.08	783	0.97	825	0.95
0.12	856	1.06	808	0.93
0.16	747	0.92	962	1.10
0.20	776	0.96	906	1.04
0.24	736	0.91	930	1.07
0.28	745	0.92	889	1.02
0.32	716	0.88	934	1.07
0.36	727	0.90	948	1.09
0.40	743	0.92	908	1.04
0.44	697	0.86	948	1.09
0.48	731	0.90	898	1.03
0.52	743	0.92	858	0.98
0.56	714	0.88	868	1.00
0.60	722	0.89	1013	1.16
0.64	613	0.76	884	1.01
0.68	496	0.61	886	1.02
0.72	522	0.65	1005	1.15
0.76	533	0.66	901	1.03
0.80	491	0.61	888	1.02
0.84	434	0.54	940	1.08
0.88	529	0.65	872	1.00
0.92	484	0.60	891	1.02
0.96	572	0.71	908	1.04
1.00	563	0.70	928	1.06
1.04	572	0.71	885	1.02
1.08	542	0.67	913	1.05
1.12	563	0.70	880	1.01
1.16	513	0.63	918	1.05
1.20	562	0.69	890	1.02
1.24	572	0.71	935	1.07
1.28	551	0.68	847	0.97
1.32	546	0.67	847	0.97
1.36	518	0.64	858	0.97
1.40	502	0.62	895	1.03
1.44	479	0.59	922	1.06
1.48	464	0.57	928	1.07
1.52	528	0.65	882	1.01
1.56	447	0.55	882	1.01
1.60	489	0.60	884	1.01
1.64	484	0.60	831	0.95
1.68	455	0.56	873	1.00
1.72	467	0.58	923	1.06
1.76	481	0.59	899	1.03
1.80	466	0.58	954	1.09

TABLE C.8 \* Diameter Versus Time,  $T_{\infty} = 1547$  K,  $\phi = 0.53$ ,  $O_2 = 10.9\%$ , Wet

Time(s)	<u>Stabilized Al/JP-10</u>		<u>Unstabilized Al/JP-10</u>	
	d(t)	d(t)/d <sub>0</sub>	d(t)	d(t)/d <sub>0</sub>
0.0	682	1.00	794	1.00
0.08	575	0.84	781	0.98
0.16	685	1.00	699	0.88
0.24	701	1.03	696	0.88
0.32	618	0.91	690	0.87
0.40	655	0.96	663	0.84
0.48	636	0.93	666	0.84
0.56	719	1.05	665	0.84
0.64	403	0.59	655	0.83
0.72	442	0.65	671	0.85
0.80	433	0.63	670	0.84
0.88	393	0.58	681	0.86
0.96	392	0.58	684	0.86
1.04	379	0.56	676	0.85
1.12	384	0.56	588	0.74
1.20	395	0.58	563	0.71
1.28	331	0.49	554	0.70
1.36	330	0.48	568	0.72
1.44	327	0.48	554	0.70
1.52			522	0.66
1.60			508	0.64
1.68			482	0.61
1.76			499	0.63
1.84			494	0.62
1.92			473	0.60
2.00			478	0.60
2.08			456	0.57
2.16			445	0.56
2.24			419	0.53
2.32			413	0.52
2.40			376	0.47
2.48			382	0.48
2.56			376	0.47
2.64			366	0.46
2.72			359	0.45
2.80			366	0.46
2.88			355	0.45
2.96			358	0.45

TABLE C.9 - Diameter Versus Time,  $T_{\infty} = 1677$  K,  $\phi = 0.58$ ,  $O_2 = 10.9\%$ , Wet

Time(s)	<u>Stabilized Al/JP-10</u>		<u>Al/C/JP-10</u>	
	d(t)	d(t)/d <sub>0</sub>	d(t)	d(t)/d <sub>0</sub>
0.0	807	1.00	800	1.00
0.04	807	1.00	794	0.99
0.08	775	0.96	801	1.00
0.12	817	1.01	895	1.12
0.16	772	0.96	931	1.16
0.20	743	0.92	926	1.16
0.24	775	0.96	902	1.13
0.28	659	0.82	898	1.12
0.32	666	0.82	905	1.13
0.36	679	0.84	918	1.15
0.40	655	0.81	922	1.15
0.44	784	0.97	923	1.15
0.48	744	0.92	918	1.15
0.52	726	0.90	928	1.16
0.56	766	0.95	925	1.16
0.60	677	0.84	917	1.15
0.64	524	0.65	911	1.14
0.68	518	0.64	897	1.12
0.72	394	0.49	908	1.13
0.76	526	0.65	910	1.14
0.80	423	0.52	907	1.13
0.84	471	0.58	892	1.11
0.88	488	0.60	896	1.12
0.92	549	0.68	901	1.13
0.96	467	0.58	900	1.12
1.00	501	0.62	904	1.13
1.04	448	0.55	911	1.14
1.08	475	0.59	887	1.11
1.12	460	0.57	909	1.14
1.16	457	0.57	906	1.13
1.20	481	0.60	905	1.13
1.24	486	0.60	908	1.14
1.28	461	0.57	893	1.12
1.32	417	0.52	898	1.12
1.36	486	0.60	899	1.12
1.40	367	0.45	893	1.12
1.44	460	0.57	920	1.15
1.48	465	0.58	903	1.13
1.52	378	0.47	901	1.13
1.56	419	0.52	905	1.13
1.60	414	0.51	896	1.12
1.64	400	0.50	900	1.12
1.68	419	0.52	904	1.13
1.72	472	0.59	901	1.13
1.76	410	0.51	898	1.12
1.80	403	0.50	902	1.13
1.84	418	0.52	902	1.13

TABLE C.10 - Diameter Versus Time,  $T_{\infty} = 1785 \text{ K}$ ,  $\phi = 0.62$ ,  $O_2 = 10.3\%$ , Wet

<u>Stabilized Al/JP-10</u>		
Time(s)	d(t)	d(t)/d <sub>0</sub>
0.00	876	1.00
0.04	863	0.99
0.08	882	1.01
0.12	773	0.88
0.16	861	0.98
0.20	845	0.97
0.24	852	0.97
0.28	835	0.95
0.32	861	0.98
0.36	864	0.99
0.40	879	1.00
0.44	881	1.01
0.48	829	0.95
0.52	550	0.63
0.56	550	0.63
0.60	573	0.65
0.64	537	0.61
0.68	540	0.62
0.72	548	0.63
0.76	571	0.65
0.80	545	0.62
0.84	538	0.61
0.88	537	0.61
0.92	560	0.64
0.96	510	0.58
1.00	552	0.63
1.04	558	0.64
1.08	541	0.62
1.12	541	0.62
1.16	517	0.59
1.20	474	0.54
1.24	467	0.53
1.28	482	0.55
1.32	471	0.54
1.36	499	0.57
1.40	549	0.52
1.44	494	0.56
1.48	481	0.55
1.52	471	0.54
1.56	460	0.53
1.60	449	0.51
1.64	446	0.51
1.68	451	0.51

APPENDIX D - JP-10 BURNING TIMES

TABLE D.1 - JP-10 Burning Times,  $T_{\infty} = 1510$  K,  $\phi = 0.54$ ,  $O_2 = 10.0\%$ , Dry

<u>Pure JP-10</u>		<u>JP-10 With Additives</u>	
$d_0$ ( $\mu\text{m}$ )	Burning Time(s)	$d_0$ ( $\mu\text{m}$ )	Burning Time(s)
771	0.60	1014	1.40
781	0.62	1095	1.28
1208	1.44	1180	1.70

TABLE D.2 - JP-10 Burning Times,  $T_{\infty} = 1548$  K,  $\phi = 0.59$ ,  $O_2 = 10.3\%$ , Dry

<u>Pure JP-10</u>		<u>JP-10 With Additives</u>	
$d_o$ ( $\mu\text{m}$ )	Burning Time(s)	$d_o$ ( $\mu\text{m}$ )	Burning Time(s)
1068	1.10	1203	1.28
1180	1.36	1239	1.44
1202	1.40	1259	1.40
		1366	1.68

TABLE D.3 - JP-10 Burning Times,  $T_{\infty} = 1659$  K,  $\phi = 0.66$ ,  $O_2 = 10.4\%$ , Dry

<u>Pure JP-10</u>		<u>JP-10 With Additives</u>	
$d_o$ ( $\mu\text{m}$ )	Burning Time(s)	$d_o$ ( $\mu\text{m}$ )	Burning Time(s)
1008	0.92	1072	1.16
1245	1.36	1202	1.24
1293	1.48	1313	1.56

TABLE D.4 - JP-10 Burning Times,  $T_{\infty} = 1809$  K,  $\phi = 0.58$ ,  $O_2 = 10.4\%$ , Dry

<u>Pure JP-10</u>		<u>JP-10 With Additives</u>	
$D_O$ ( $\mu\text{m}$ )	Burning Time(s)	$d_O$ ( $\mu\text{m}$ )	Burning Time(s)
938	0.68	905	0.60
1174	1.02	1087	0.80
1297	1.30	1276	0.98

TABLE D.5 - JP-10 Burning Times,  $T_{\infty} = 1827$  K,  $\phi = 0.37$ ,  $O_2 = 25.2\%$ , Dry

<u>Pure JP-10</u>		<u>JP-10 With Additives</u>	
$d_O$ ( $\mu\text{m}$ )	Burning Time(s)	$d_O$ ( $\mu\text{m}$ )	Burning Time(s)
610	0.22	978	0.72
710	0.28	1036	0.76
1108	0.72	1099	0.82
1205	0.90	1152	0.92

TABLE D.6 - JP-10 Burning Times,  $T_{\infty} = 1417$  K,  $\phi = 0.50$ ,  $O_2 = 10.9\%$ , Wet

<u>JP-10 With Additives</u>	
$d_o$ ( $\mu\text{m}$ )	Burning Time(s)
747	0.58
1002	0.85
1148	1.02
1191	1.08

TABLE D.7 - JP-10 Burning Times,  $T_{\infty} = 1519$  K,  $\phi = 0.50$ ,  $O_2 = 10.9\%$ , Wet

<u>Pure JP-10</u>		<u>JP-10 With Additives</u>	
$d_o$ ( $\mu\text{m}$ )	Burning Time(s)	$d_o$ ( $\mu\text{m}$ )	Burning Time(s)
938	0.76	814	0.82
1194	1.20	1105	1.22
		1226	1.38
		1324	1.60

TABLE D.8 - JP-10 Burning Times,  $T_{\infty} = 1547$  K,  $\phi = 0.53$ ,  $O_2 = 10.9\%$ , Wet

<u>JP-10 With Additives</u>	
$d_0$ ( $\mu\text{m}$ )	Burning Time(s)
1015	1.0
1134	1.0

TABLE D.9 - JP-10 Burning Times,  $T_{\infty} = 1677$  K,  $\phi = 0.58$ ,  $O_2 = 10.9\%$ , Wet

<u>Pure JP-10</u>		<u>JP-10 With Additives</u>	
$d_0$ ( $\mu\text{m}$ )	Burning Time(s)	$d_0$ ( $\mu\text{m}$ )	Burning Time(s)
640	0.33	1012	0.88
757	0.44	1097	0.96
897	0.60	1290	1.32
1153	1.00		

TABLE D.10 - JP-10 Burning Times,  $T_{\infty} = 1785$  K,  $\phi = 0.62$ ,  $O_2 = 10.3\%$ , Wet

<u>JP-10 With Additives</u>	
$d_0$ ( $\mu\text{m}$ )	Burning Time(s)
1040	0.86
1053	0.86
1227	1.03

E N D

10-86

D T / C